Institut de Physique
Université de Neuchâtel

Influence of anisotropy and disorder on the dynamic response of Josephson junction arrays

THESE

présentée à la Faculté des Sciences
de l'Université de Neuchâtel
pour l'obtention du grade de docteur ès Sciences

par

Jérôme Affolter
physicien diplômé
de l'Université de Neuchâtel

Neuchâtel, juillet 2001

A mes parents

IMPRIMATUR POUR LA THESE

Influence of anisotropy and disorder on the dynamic response of Josephson junction arrays

M. Jérôme AFFOLTER

UNIVERSITE DE NEUCHATEL

FACULTE DES SCIENCES

La Faculté des sciences de l'Université de Neuchâtel, sur le rapport des membres du jury

MM. P. Martinoli (directeur de thèse),
H. Beck, C. Schönenberger (Bâle)
et B. Pannetier (Grenoble F)

autorise l'impression de la présente thèse.

Neuchâtel, le 16 août 2004

La doyenne:

Prof. M. Rahier

Contents

List of Figures

Chapter 1

Introduction

1.1 Introduction and motivations

Josephson junction arrays (JJAs) have been abundantly studied, both theoretically and experimentally during these last decades, because their behavior allows to consider the interaction between several fundamental physical notions of two dimensional (2D) systems. Under certain circumstances they constitute indeed a direct realization of the XY model, and can so be used as model systems to broach a variety of basic physical concepts, from a static [1] as well as from a dynamical [2] point of view. By way of examples commonly studied, we can mention in particular phase transitions or frustration phenomena.

The work presented in this document constitutes an extension of previous studies, and has been realized by probing the response of arrays patterned with non-conventional geometries. More precisely, we measured the properties of disordered arrays on the one hand, and of anisotropic arrays on the other hand.

The notion of disorder takes place in the description of a large number of physical systems [3], but is generally a poorly controlled parameter. In this work, we chose on the contrary to create a system in which the nature and the amount of disorder can be accurately tuned, by using a site percolation process [4]: we randomly removed a known fraction of junctions from the array. An important characteristic of the percolation structures is the presence of a geometrical phase transition, leading at the percolation threshold to vacancies which extend to all length scales [4, 5]. This kind of structures shows in this case a remarkable property: if one selects one part and that enlarges it arbitrarily, this portion possesses the same statistical properties as the whole system. Such a system is self-similar, and is then described by a fractal geometry.

In the part of this document devoted to percolative arrays, we will study the effects related to the introduction of disorder in the structure of our samples. More particularly, we will first establish the influence of the self-similar structure at low temperature when the array is submitted to a weak external magnetic field. Then, in a second stage, we will focus on a domain of response close to the critical temperature. As a result of the intrinsically dynamical character of our measurement method, it will then be possible to probe the nature of the excitations at several scales and for different temperature regions.

This will also allow to set the kind of transition appearing in this disordered structure following from a change of temperature.

The critical behavior of the unfrustrated regular JJAs is relatively well understood and has been the subject of many works [6]: below the critical temperature the system is characterized by a quasi-long range order, which is broken at the transition temperature by the dissociation of pairs of point defects, in the form of vortex-antivortex pairs. These thermal excitations are associated with continuous symmetry properties of the order parameter, and lead to a transition described by Beresinskii, Kosterlitz and Thouless [7, 8] (BKT).

On the contrary, the critical behavior of frustrated arrays is only partially understood [9, 10, 11]. The frustration adds indeed discrete symmetries in the ground state, which are associated with a chiral order parameter [12]. The resulting critical behavior could then lead to an Ising-like transition in which linear defects, also called domain-walls, could play a role in addition to the point defects. The second part of this document is devoted to the study of these two kinds of thermal excitations. More specifically, we chose to perform measurements on arrays whose unit cell is pierced by half a flux quantum, and for which the coupling energy of the junctions was modulated in one direction. This configuration is specially interesting, because it allows to separate the critical regions associated with the two kinds of transitions. It is therefore possible to decouple the two critical regions.

1.2 Organization of this work

This thesis is organized as follows. In section two we will succinctly present the basic array physics. We will introduce the notions necessary to model the junctions when they are considered as independent entities. This will allow to present next the theoretical foundations useful to describe the collective phenomena following from their assembly in a network. It will then be possible to express the response of a regular array exposed to a weak electromagnetic field in the limit of low temperatures.

Chapter 3 is devoted to the description of the equipment used to perform the data acquisition. Moreover, we will discuss the electrodynamics of the two-coil measurement system, and the advantages and disadvantages related to this technique. At the end of the chapter we will present the numerical procedure used to convert the raw signal in quantities interpretable physically.

The fabrication process and the geometrical characteristics of the samples are described in chapter 4. In a first step we present separately the criteria leading to the design of the optical masks used to define the patterns of the percolative and modulated arrays. Afterwards we will discuss the deposition and photolithography processes, which are common to the two kinds of samples. This chapter will end by a discussion in which we will expose the physical features of the junctions constituting the arrays.

To avoid repetitions, we chose to present the notions common to the two kinds of arrays in the first four chapters of this document. Then chapters 5 and 6 are devoted to percolative and modulated arrays respectively. Chapter 5 starts with a reminder about

percolation theory. We next present the measurements and the theoretical notions useful to their explanation in four successive stages.

Chapter 6 is devoted to modulated arrays and is constituted of two main parts. In the first one, we will present the theory related to the phase transitions in junction arrays at zero and full frustration. These predictions will be compared to our measurements in the second part.

Chapter 2

General considerations

2.1 Introduction

In this section we introduce the basic physics necessary to the description of JJAs. To begin with, we briefly present the theoretical notions allowing to describe the kind of junctions used in this work. To this end, we recall some properties of the proximity effect junctions when they are considered as independent entities.

In a second stage, we describe the properties resulting from an assembly of junctions in a regular pattern. We set down the theoretical foundations allowing the description of the two-dimensional collective phenomena related to the JJAs. To simplify the discussion we restrict ourselves to consider an array with a regular structure. This discussion will nevertheless keep a general aspect and will give us the possibility to introduce some fundamental notions which will next be extended in chapters 5 and 6 to take into account the percolative and modulated structures peculiar to the arrays studied in this work.

2.2 Model of the junction

The junctions used in this work consist of two superconducting (S) islands separated by a normal (N) metal gap, as shown in Fig. 2.1. By lowering the temperature below the transition temperature T_{cs} of the lead islands, the density of Cooper pairs becomes non-zero in the superconducting areas. The Cooper pairs will then diffuse by proximity effect through the S-N interface out to a weakly temperature dependent distance $\xi_N(T)$, the coherence length in the normal metal. It describes the extension of the superconducting wavefunction in the normal metal. In the dirty limit where the mean free path ℓ of the electrons in the normal metal is smaller than $\xi_N(T)$, it is expressed by [13]:

$$\xi_N(T) = \sqrt{\frac{\hbar v_F \ell}{6\pi k_B T}} \tag{2.1}$$

where v_F is the Fermi velocity in the normal metal. $\xi_N(T)$ therefore increases with decreasing temperature, and at sufficiently low temperature there will be an overlap of

the Cooper pair densities extending from the two superconducting islands. In this way a superconducting bridge appears through the normal metal, and this system constitutes then an SNS junction.

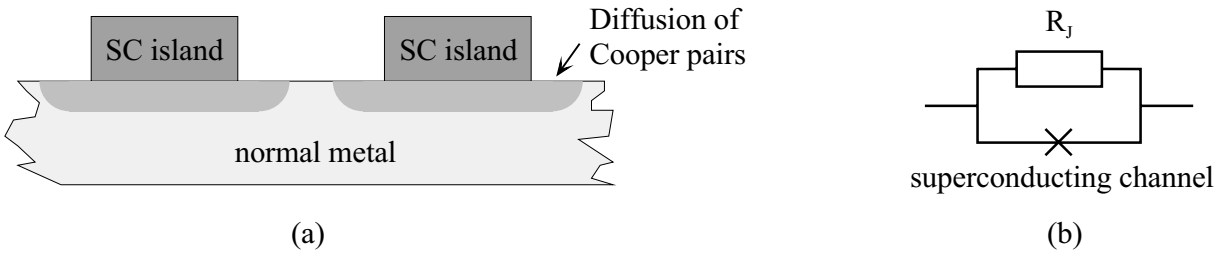

Figure 2.1: (a) Schematic view of a proximity effect junction. The two superconducting islands are separated by a normal metal bridge through which the Cooper pairs diffuse by proximity effect. (b) Equivalent circuit for an SNS junction. The superconducting channel is in parallel with a normal channel represented by a resistance R_J.

Let us express the superconducting wavefunction on the site j with $\psi_j = \psi_{0j} \exp(i\varphi_j)$. The gauge invariant phase difference between two sites i and j is then given by [14]:

$$\vartheta_{ij} = \varphi_j - \varphi_i + A_{ij} \quad \text{with} \quad A_{ij} = \frac{2\pi}{\phi_0} \int_i^j \vec{A}\, \overrightarrow{dl} \tag{2.2}$$

where $\vec{A}$ is the magnetic vector potential, which is zero in zero external magnetic field. The superconducting current I_{Sij} crossing the junction and the voltage across the junction V_{ij} are related through the phase difference by the relationships [15, 16]:

$$I_{Sij} = I_C \sin \vartheta_{ij} \quad \text{and} \quad \frac{d\vartheta_{ij}}{dt} = \frac{2e}{\hbar} V_{ij} \tag{2.3}$$

where I_C is the junction critical current. These two equations indicate in particular that a current smaller than the critical current can flow through the junction without the appearance of any voltage. It is the dc Josephson effect. One notices that application of a direct voltage to the terminals of the junction leads to the appearance of an alternating current. It is the ac Josephson effect.

The temperature dependence of the critical current near T_{cs} for a SNS junction without external magnetic field is described by the de Gennes formula[1] [17]:

$$I_C(T) = I_C(0) \left(1 - \frac{T}{T_{cs}}\right)^2 \exp\left[\frac{-l}{\xi_N(T_{cs})} \left(\frac{T}{T_{cs}}\right)^{1/2}\right]. \tag{2.4}$$

where l is the distance separating two superconducting islands. It is possible to calculate the energy E_{ij} stored in a junction by integrating of the power needed to create a phase

[1] See the discussion about the data analysis (Eq. (3.6)) for the validity of the de Gennes relation in the case of SNS junctions.

difference ϑ_{ij} (see Eqs. (2.3)) over a period. In this way one obtains $E_{ij} = E_J(T)(1 - cos\vartheta_{ij})$, with $E_J(T) = \hbar I_C(T)/(2e)$ the coupling energy. It is also useful to introduce the charging energy $E_C \equiv e^2/(2C)$ to determine the junction behavior. Because the value of the capacitor C depends of the geometry of the electrodes, the value of E_C will mainly depend on the size and the shape of the junctions. The SNS junctions used in this work are described by a large ratio E_J/E_C, therefore allowing to neglect charging effects and to describe the junction in a classical regime.

SNS junctions are usually well described in the framework of the RSJ (Resistively Shunted Junction) approach [14], a two fluid model, where the total current flowing through the junction is described by a superconducting channel in parallel with a normal channel, as shown in Fig. 2.1 (b). Because the normal currents generate dissipation, they are taken into account with a resistance R_{ij} between the neighboring sites i and j.

2.3 XY Model

The aim of this section is to recall some general notions related to the XY model. To simplify the discussion we consider only the case of arrays of identical junctions. The modifications necessary to study percolative or modulated arrays will be considered in chapters 5 and 6.

The geometrical parameters of the junctions were chosen to obtain a coupling between the superconducting sites which becomes important at temperatures well below the superconducting mean field transition of the islands. The relevant temperature region is therefore situated well below T_{cs}, allowing to neglect the fluctuations in the magnitude of the order parameter in the Pb islands. The Hamiltonian of the array is then given by the sum of the coupling energies of all the pairs of nearest-neighbor sites and leads, following section 2.2 to :

$$H = \sum_{<ij>} E_J[1 - cos\vartheta_{ij}] \quad \longrightarrow \quad H = -E_J \sum_{<ij>} cos\vartheta_{ij} \tag{2.5}$$

where the second expression is introduced without loss of generality, and is used to simplify the writing. The phase difference ϑ_{ij} is defined according to Eq. (2.2). By associating the phase of the superconducting order parameter of each island with a planar spin situated on the considered site, one thus obtains a physical realization of the XY model. In zero external magnetic field (i.e. $A_{ij} = 0$ following Eq. (2.2)), the ground state is therefore realized by a set of parallel spins pointing in some direction. Any change of this state will be ascribed to the appearance of collective two-dimensional phenomena.

By neglecting the screening currents flowing in the lead islands, the presence of a perpendicular external magnetic field can be described by introducing a frustration parameter $f = \sum A_{ij}/(2\pi)$, which is defined as the magnetic flux threading a unit cell of the array in units of the flux quantum ϕ_0. The fluxoid quantization leads then to $\sum \vartheta_{ij} = 2\pi(m + f)$, where the sum runs over the contour of an elementary plaquette, and where the integer m defines the vorticity of the cell [14]. It is not an easy task to

find the ground state of the φ_j at arbitrary frustration, and this problem is solved only in some particular cases. For example, the case of a regular square array at full frustration is discussed in section 6.1.2.

Notice that the Hamiltonian (2.5) is an even function in f and periodic in f with period 1. When investigating arrays in magnetic field, it is thus sufficient to consider the interval corresponding to $0 \leq f < 1/2$.

We saw in section 2.2 that the Josephson coupling energy is strongly temperature dependent for proximity effect junctions. To conserve the isomorphism with the XY-model, we have to get rid of this dependency; this may be achieved by introducing a reduced temperature τ, defined as the ratio between the thermal and the coupling energy:

$$\tau \equiv \frac{k_B T}{E_J(T)}. \tag{2.6}$$

By expressing our results as a function of this dimensionless parameter, it is thus possible to keep track only of the collective phenomena related to the global response of the arrays.

2.4 Conductance of a regular array without fluctuations

In this section we express the linear response of an array to a weak ac excitation current in the limit of low temperatures. We will deduce its sheet conductance G which is the quantity experimentally accessible. This result is valid only for an array with a regular square structure, but will be extended to percolative or modulated structures, as indicated in chapters 5 and 6.

Let us consider a square array at temperature low enough to neglect the fluctuations of the phase of the superconducting order parameter. If the excitation current is weak, it is possible to express [18], within the frame of the RSJ model, the conductance G_{ij} of the junction between the sites i and j as a function of the gauge invariant phase difference ϑ_{ij} in the ground state:

$$G_{ij} = \frac{1}{i\omega}\left[\frac{2e}{\hbar} I_{Cij} cos\vartheta_{ij}\right] + \frac{1}{R_{ij}}, \tag{2.7}$$

showing that a single junction can be described by a junction resistance R_{ij} in parallel with a junction inductance $L_{ij} = \hbar/(2eI_{Cij}\cos\vartheta_{ij})$. If we assume that the junctions are all identical, $I_{Cij} = I_C$ and $R_{ij} = R_J$. In the ground state of the unfrustrated system ($f = 0$), $cos\vartheta_{ij} = 1$, and the junction inductances are all equal and are related to the Josephson coupling energy by $L_J \equiv \hbar/(2eI_C) = (\hbar/(2e))^2 E_J^{-1}$. In these conditions, the measured sheet conductance G of a square array is simply given by

$$G = \frac{1}{i\omega L_J} + \frac{1}{R_J}. \tag{2.8}$$

For other kinds of geometry, the array structure may be taken into account by an appropriate multiplicative factor (for example $\sqrt{3}$ for a triangular array) for G.

Chapter 3

Experimental setup and measuring technique

3.1 Experimental setup

The equipment described in this section allows to measure the response of JJAs as a function of temperature, of an external magnetic field or of the measurement frequency. A detailed description of the parameters used for each kind of measurement are listed in Refs [19, 20].

The measurements presented in this work were realized in a ^{4}He cryostat (see appendix I) surrounded by an external N_2 dewar, allowing to reduce the supply of external heat and the losses of ^{4}He. Except for the computer, the whole electronic equipment was placed in a Faraday cage to reduce the effects due to undesirable electromagnetic perturbations. Moreover, low frequency magnetic fields, and in particular the earth's magnetic field, were shielded by a cylinder of high permeability material (μ – metal) surrounding the N_2 dewar and with a lead cylinder in the ^{4}He bath.

The sample is mounted in an evacuated pot on a sapphire plate, which is coupled to a coldplate by Delrin bars on which a heater is wound. The 1 K pot is filled with ^{4}He through a capillary and is connected to a manostat which allows to establish a controlled pressure inside it and therefore to stabilize the temperature. A germanium resistance thermometer embedded in the sapphire block is used to measure the temperature and serves as a sensor for the temperature feedback loop. With this system it is possible to measure temperatures in a range between 1.5 K and 10 K, and to achieve a temperature stability better than 1 mK for temperatures lower than 4 K and better than 3 mK for higher temperatures.

The pot is surrounded by a superconducting coil producing a magnetic field which allows to control the frustration applied to the arrays. This coil is provided with a mechanical superconducting switch which allows to use the coil in a persistent mode, to obtain high-stability magnetic fields. The coil gives a field of 0.285 G/mA, and the computed homogeneity of the field over the whole array is better than 1 part in 10^4 [22].

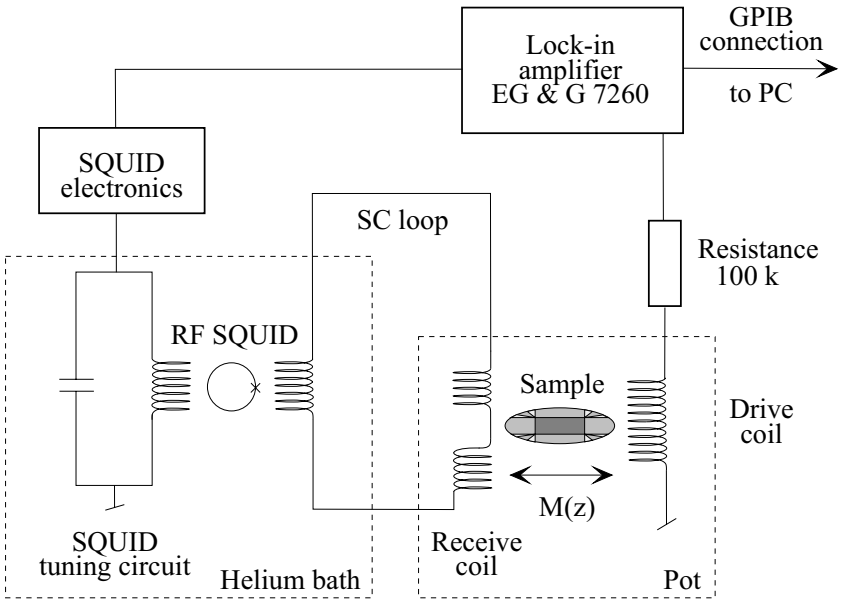

Figure 3.1: Schematic view of the inductive measurement setup.

The inductive measurement setup used in this work consists of exposing a sample to the electromagnetic field produced by a drive coil in which a small ac current flows. The excitation current is generated by the internal oscillator of a lock-in (7260 from *EG&G*), and has an amplitude of 0.5 μA. This current induces an ac magnetic field of the order of 10^{-4} G corresponding to a frustration of about 10^{-4}. A second coil, called detection or receive coil, is connected in series with the input coil of a SQUID (rf SQUID from Quantum Design with BTI electronics). These two elements constitute the superconducting loop: they are linked by a pair of twisted superconducting wires screened from external magnetic fields by superconducting PbSn tubes. In the presence of ac screening currents induced in the sample, a flux change is detected by the receive coils and is transmitted to the input coil of the SQUID via the superconducting detection loop. This is measured by the SQUID, and then treated to extract the physical quantities characterizing the sample. The measurement procedure is controlled by checking that the SQUID feedback signal is directly proportional to the mutual inductance between the drive and the receive coils. Moreover, the current flowing in the excitation coil has to be reduced until a linear response of the sample is observed.

The main advantage provided by the use of a SQUID is the possibility to detect extremely weak signals. Moreover it allows to measure almost directly the flux induced in the superconducting loop [20]. It is possible to perform measurements at frequencies ranging from 0.1 Hz to 20 kHz, the lower limit being fixed by the acquisition time, while the higher limit is determined by the SQUID electronics.

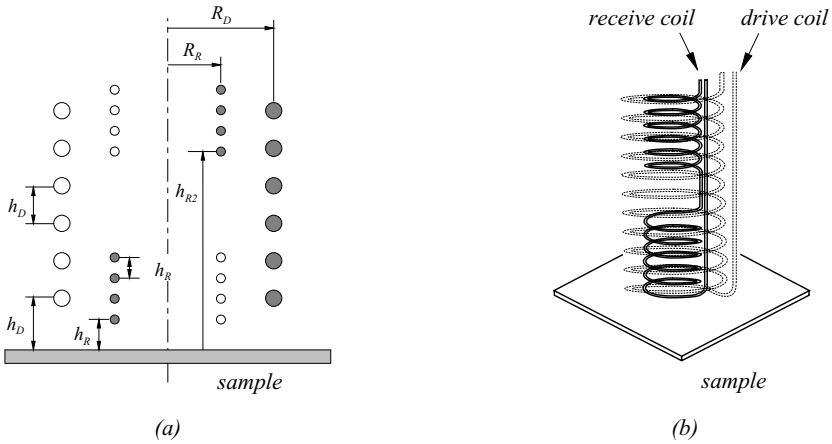

Figure 3.2: (a) Schematic view of the coil measurement system. The description of the geometrical parameters refers to table 3.1. (b) Schematic view of the coils and film arrangement. Notice the astatic configuration of the receive coils.

Coil	Drive	Receive
Radius	$R_D = 2.05\,\text{mm}$	$R_R = 1.47\,\text{mm}$
Number of turns	$N_D = 25$	$N_R = 2 \times 18$
Distance between turns	$\delta h_D = 0.2\,\text{mm}$	$\delta h_R = 0.055\,\text{mm}$
Distance 1st turn-sample	$h_D = 0.7\,\text{mm}$	$h_R = 0.2\,\text{mm}$, $h_{R2} = 4.7\,\text{mm}$
Inductance	$L_E \approx 1.5\,\mu\text{H}$	$L_R \approx 1.2\,\mu\text{H} \times 2$
Material	Cu ($\varnothing 100\,\mu$m)	NbTi ($\varnothing 50\,\mu$m)

Table 3.1: Parameters of the excitation and of the detection coils; see text for details.

The geometrical parameters of the coil system are summarized in table 3.1. The coils are cast in an epoxy resin shaped to bring them as close as possible to the sample, as shown in Fig. 3.2 (b). The distance between the sample and the coils fixes the amplitude of the measured signal, and will be determined by fitting the calculated signal to the measurements. The astatic winding of the receive coil allows to reduce the noise due to magnetic perturbations varying slowly in space over distances comparable to the size of the receive coils. Moreover, if the excitation-detection system is perfectly balanced, there is no signal at the terminals of the detection coils in the absence of a sample. For experimental reasons, it is nevertheless useful to put the excitation coils slightly shifted along the common axis with respect to the center of the driving coil. One produces in this way intentionally a diamagnetic offset, called pick-up, which is used to adjust the phase of the signal; moreover, this offset allows to increase the sensitivity of the measurement system.

The data acquisition as well as the magnetic field, the temperature and the measurement frequency are monitored by a computer. It is placed outside the Cu Faraday cage, and is connected to the measurement instruments by a GPIB bus.

3.2 Inductive measurement technique

This technique consists of exciting a sample with an ac electromagnetic field produced by the drive coil, and detecting the signal due to the screening currents induced in the sample with an astatically wound detection coil (see section 3.1). The measurement principle is therefore based on the flux imbalance created by the sample between the upper and the lower part of the receive coil. This produces a change in the mutual inductance between the drive and the receive coils, which is measured by the SQUID.

The two-coil technique

This measurement technique is particularly well suited to the characterization of superconducting arrays because the inductive response of the sample is a measurement of its conductance. So, contrary to the usual transport measurements which probe the " bad-conduction " properties of the sample, the inductive technique offers the possibility to measure low impedance samples. This allows to investigate the physical properties of the samples below their transition temperatures. Another advantage of this measurement technique is its intrinsically dynamic nature: it allows to study the response as a function of frequency in a very wide range. To each measurement frequency corresponds a time window through which we observe the physical phenomena. It is thereby possible, for example, to compare the physical parameters extracted from low frequency measurements with theoretical estimates in the thermodynamic limit. Moreover, notice that in an experiment at frequency ω the measurement probes the dynamics of the vortices at length scales $r_\omega \sim (D_v/\omega)^{1/2}$, where D_v is the vortex diffusion constant [21].

The inductive measurement technique combined with the use of a SQUID allows to use very weak excitations levels (see section 3.1). We have thus access to a linear regime where the response of the sample is proportional to the excitation level. In this way it is possible to probe a regime where the amplitude of the excitation current has no noticeable effects on the response of the studied physical phenomena. As a last advantage, the inductive technique is contactless, allowing to avoid problems arising from thermal voltages.

The use of the inductive measurement technique involves an inversion procedure to extract the sheet conductance from the measured mutual inductance, as discussed in the next section. Moreover, the inversion procedure imposes some restrictions on coils and sample geometry. In particular the array should appear homogeneous at the scale of the coils, and the lateral sample size should be larger than the coils diameter to avoid edge effects.

Electrodynamics of the system

The aim of this section is to examine the relationship between the sheet impedance of the sample $Z \equiv R + i\omega L$ and the complex mutual inductance $M \equiv M' + iM''$ measured between the drive and the receive coils. As the calculation was carefully performed in Refs [20, 18], we shall not go into details here, but only recall the major steps of the analysis by emphasizing the conditions necessary for the validity of the model.

The first step of the calculation is to find the relationship expressing the sheet current density $\vec{K}_s$ induced in the sample by the excitation coil. This is possible by assuming of a time dependence $e^{i\omega t}$ for the fields the currents, and that the sample is two-dimensional, homogeneous and infinite. The two-dimensional character implies that the sheet current density is constant through the thickness of the sample. In this experiment we consider samples large enough to be able to neglect the influence of finite size effects on the mutual inductance of the system [23].

The signal induced in the receive coil by the current distribution is calculated with the path integral of the electric field generated by $\vec{K}_s$ along each of the turns of the detection coil. It follows so that the mutual complex inductance $M(Z)$ is related to the sample impedance by the relationship [22, 24]:

$$M(Z) \equiv M' + iM'' = \int_0^\infty dx \frac{\widetilde{M}(x)}{1 + \frac{2}{\mu_0 h}\frac{Z}{i\omega}x} \quad , \tag{3.1}$$

where $h \equiv h_D + h_R$ and ω is the angular frequency. $\widetilde{M}(x)$ is a function depending only on the geometrical parameters of the coil system (see table 3.1) and which can be written [24]:

$$\widetilde{M}(x) = \pi\mu_0 \frac{R_D R_R}{h} J_1(\frac{R_D}{h}x) J_1(\frac{R_R}{h}x) \frac{1 - e^{-\frac{\delta h_D N_D}{h}x}}{1 - e^{-\frac{\delta h_D}{h}x}} \frac{1 - e^{-\frac{\delta h_R N_R}{h}x}}{1 - e^{-\frac{\delta h_R}{h}x}} e^{-x} \quad , \tag{3.2}$$

where $J_1(x)$ is the first-order Bessel function, and $x \equiv q_t h$ represents the transverse component (i.e. in the sample plane) of the wave vector. Eq. (3.1) establishes the relationship between the measured mutual inductance and the sheet impedance of the sample in a non-trivial way which depends on the geometry of the system. Because this integral relationship is not analytically solvable, we have to extract the sheet impedance by performing an iterative numerical inversion procedure which is described at the end of this section. It is nevertheless useful to notice that $\widetilde{M}(x)$ possesses a particular shape with a peak centered at $x_0 = 0.504$ [20]. It is thus possible to write in good approximation $\widetilde{M}(x) \simeq M_{ss}\delta(x - x_0)$ with $M_{ss} = \int_0^\infty \widetilde{M}(x)dx$. By using this approximation of $\widetilde{M}(x)$ we obtain a simplified solution of Eq. (3.1):

$$\frac{M(Z)}{M_{ss}} \equiv m' + im'' \approx \left[1 + \frac{Z}{i\omega M_c}\right]^{-1} \quad , \tag{3.3}$$

where $M_c \equiv \mu_0 h/(2x_0)$ represents the characteristic inductance of the coil system and is equal to $M_c \simeq 1.12 \cdot 10^{-9}$ H for our setup. In this way, we can directly extract two approximate solutions for the real and imaginary parts of Z:

$$R \approx M_c \frac{\omega m''}{m'^2 + m''^2} \quad \text{and} \quad L \approx M_c \frac{m'}{m'^2 + m''^2} - 1. \tag{3.4}$$

For temperatures well below the transition temperature of the sample, the sheet impedance is basically inductive and corresponds to the signal of a perfect diamagnetic sample. This

is the strong screening limit, which corresponds to a very small effective penetration of the magnetic field in the sample. In this limit, Eq. (3.1) reads $M(Z) \simeq \int_0^\infty \widetilde{M}(x)\,dx \equiv M_{ss}$. In this case the measured mutual inductance contains therefore only information about the geometry of the coil system. It can be numerically calculated by using the values shown in table 3.1; $M_{ss} = 1.314 \cdot 10^{-8}$ H [20] for the parameters of our coils.

At high temperature, i.e. in the normal state of the sample, the impedance is on the contrary purely resistive. By considering Eq. (3.1), one then deduces that the mutual inductance is purely imaginary for measurements performed at low enough frequencies and for samples possessing high resistances in the normal state.

The inductive measurement method suffers from intrinsic limitations which can be described by considering Eq. (3.3). Let us introduce a complex penetration depth $\Lambda = \Lambda' + i\Lambda''$ related to the sheet impedance by $Z = i\omega\mu_0\Lambda/2$ [14]. The equation (3.3) can then be written in the form:

$$\frac{M(Z)}{M_{ss}} \approx \left[1 + \frac{\Lambda}{r_c}\right]^{-1} , \tag{3.5}$$

where $r_c \equiv x_0/h \simeq 2$ mm represents a length of the order of the coil system. This relationship indicates that the measurement of a physically significant signal is possible when the term Λ/r_c is of the order of 1. So, in the limit of low temperatures, which corresponds to $\Lambda/r_c \ll 1$, the sensitivity limit is mainly fixed by the difference between the measured signal and its saturation value M_{ss}. By considering a purely inductive signal, we can then obtain an estimate of the sensitivity threshold, which is of the order of 1 pH with our measurement setup [22, 18]. The high temperature limit (normal state of the sample) corresponds to the case $\Lambda/r_c \gg 1$, which causes a decrease of the measured signal proportional to ω/Z following Eq. (3.5). In this case, the largest measurable impedance will be a function of the sensitivity and of the resolution of the equipment. To conclude this discussion about the experimental resolution of the inductive measurement technique, it is useful to go back to Eqs. (3.4). These relations indicate that the inductive part of the impedance has a resolution independent of frequency, contrary to the dissipative part for which the resolution is fixed by the ratio R/ω. One notices therefore that it is possible to probe low resistances by using low frequencies.

First stage of the data analysis

The first stage of the treatment of the measurements consists of a succession of semi-automatic simple operations whose aim is to transform the raw signal into data useful for the numerical inversion procedure.

- The first step is a correction of the reference phase peculiar to each measurement frequency. Before a measurement, the phase of the signal is adjusted by assuming that above the transition temperature the signal consists of an inductive component only, resulting from the incomplete compensation of the astatic wiring of the detection coils (pick-up). Actually, however, the ac field of the excitation coil will generate

eddy currents in the Cu layer of the sample, which adds a dissipative component to the measured signal. The phase has therefore to be corrected by a phase angle $\Delta\varphi_c$. It is possible to obtain an estimate of $\Delta\varphi_c$ with Eq. (3.3) and by taking into account eddy currents flowing in a thickness determined by the skin effect [18, 25]. In this way one obtains $\Delta\varphi_c = \arctan[\mu_0 h\omega/(2R_N x_0)]$, where R_N represents the normal state sheet resistance of the sample. The correction for the phase angle is $\Delta\varphi_c = 1.6\,^\circ$ for the geometry of our coils at $\omega/(2\pi) = 20$ kHz and for a normal state sheet resistance of 5 mΩ. Although this effect is only noticeable at frequencies higher than 1 kHz, we corrected for it in the whole frequency range.

- The second step consists in correcting the bad compensation of the coil system. This bad compensation leads to an offset in the inductive part of the signal (pick-up), which is constant as a function of temperature but depends on the measurement frequency. To correct this effect we simply subtract the pick-up from the imaginary part of the measured mutual inductance to move the high temperature plateau of the signal to zero. In this way we obtain the curve which would have been measured with a perfectly compensated system.

- The aim of the last operation is to normalize the data with respect to M_{ss}. Because this value is not completely reached even at low temperature, we had to define a criterion to determine the saturation value M_{ss}. Our criterion is based on the de Gennes prediction [17] for the behavior of the critical current of a junction as a function of temperature. This critical current can be related to the inverse sheet inductance $L^{-1}(T)$ of the array measured in the absence of fluctuations in zero magnetic field. This relationship follows from Eqs. (2.4), (2.7) and (2.8):

$$L^{-1}(T) = A\left(1 - \frac{T}{T_{cs}}\right)^2 e^{-|C|\sqrt{T}}, \tag{3.6}$$

  where $C = (6\pi k_B/(\hbar v_F \ell))^{1/2} l$ (see Eq. (2.1)) and A depends of the nature of the array (see section 4.4). The equation (3.6) was derived from the de Gennes expression for the critical current I_C (Eq. (2.4)), which, strictly speaking, is valid only close to T_{cs}. At lower temperatures ($T \ll T_{cs}$), I_C is given by a different expression [26]. Moreover, since the temperature dependence of I_C in both limits ($T \leq T_{cs}$ and $T \ll T_{cs}$) is dominated by the same exponential factor, the procedure to determine M_{ss} is insensitive to the details of $I_C(T)$. Therefore, in this work we will rely only on the de Gennes relation. The equation (3.6) predicts that a plot of $\ln[L^{-1}(T)/(1 - T/T_{cs})^2]$ as a function of $\sqrt{T}$ will be linear at temperatures where fluctuations can be neglected. It is this criterion which was adopted to normalize the data, by slowly varying the amplitude of the saturation signal to obtain a linear behavior at low temperature. The numerical values used for the fit and a more complete discussion of this procedure for percolative and modulated arrays are given in sections 4.4.1 and 4.4.2.

The data are then ready to be inverted by a numerical procedure which at last gives the real and imaginary parts of the sheet impedance.

Numerical inversion procedure

The purpose is to extract R and L from the integral (3.1) assuming $m' \equiv M'/M_{ss}$ and $m'' \equiv M''/M_{ss}$ are known. This procedure has been described in detail [20, 23], and we will therefore only describe here the main steps. The method applied in this work is based on the iterative algorithm of Newton-Raphson [23], which allows to find the zero of two functions $f_i(X)$ $(i = 1, 2)$ where X represents a two-component vector. By expanding these two functions in the neighborhood of X in Taylor series, and by neglecting terms of order higher than one, one obtains a set of two linear equations. Their solution allows to find the first order correction. Assuming convergence, the solution is improved at each iteration. The process is continued until the desired accuracy is achieved.

Applied to our problem, the Newton-Raphson method amounts to find the zero of two functions f_1 and f_2 directly derived from the real and imaginary parts of Eq. (3.1):

$$f_1 = -m' + \frac{1}{M_{ss}} \int_0^\infty dx \frac{1 + g_2 x}{(1 + g_2 x)^2 + (g_1 x)^2} \widetilde{M}(x) \quad \text{and} \tag{3.7}$$

$$f_2 = m'' - \frac{1}{M_{ss}} \int_0^\infty dx \frac{g_1 x}{(1 + g_2 x)^2 + (g_1 x)^2} \widetilde{M}(x)\,, \tag{3.8}$$

where g_1 and g_2 are the variables to be extracted, defined as follows:

$$g_1 = \frac{2}{\mu_0 h} \cdot \frac{R}{\omega} \quad \text{and} \quad g_2 = \frac{2}{\mu_0 h} \cdot L. \tag{3.9}$$

The initial guess for the Newton-Raphson algorithm is given by approximating the geometrical function $\widetilde{M}(x)$ by a delta function centered in its first maximum x_0. The first trial solution for the iterative process is therefore given by Eqs. (3.4).

Measurements as a function of frequency

A particular effort was made to carry out measurements of isotherms at constant frustration as a function of the driving frequency, which allow to probe directly the response of the sample at several length and/or time scales. This novel approach takes therefore full advantage of the dynamical aspect of the two-coils technique. Moreover, it allows to save time during the data acquisition, because the experimental setup is easier to stabilize following a change of the excitation frequency than following a change of temperature. It is necessary to determine first the reference phase and the amplitude at each excitation frequency . This is done during a preliminary reference measurement above the temperature T_{cs}, with the signal of the pickup. One then measures the isotherms in the appropriate frequency range, and corrects them with the reference phase angle determined with the previous measurement. It is then possible to perform the eddy currents correction, and to normalize the data with the amplitude of the reference measurements. The inversion procedure is finally applied in the way described above.

Chapter 4

Fabrication and characterization of the samples

4.1 Introduction

In this chapter we describe the fabrication process used to produce the samples as well as the geometrical parameters defining their patterns. In a second stage we present the method used to determine the physical characteristics of the junctions when they are considered as independent entities. This will in particular allow to establish the relationships between the measured temperature T and the reduced temperature τ.

Let us notice that some notions introduced in this chapter will be discussed in a more detailed way in chapters 5 and 6, in particular in section 5.2. This presentation enables us to completely discuss the geometrical properties of the arrays.

4.2 Design of the masks

The design of the masks used in the photolithographic process is the first stage in the study of SNS classical arrays. They consist of a quartz slide covered by a chrome pattern about 1 cm square defining the array geometry. Because the geometry of the mask determines the type of the array, we will present separately the geometries of the percolative array and of the modulated array. On the other hand, the fabrication process of the two kinds of samples are similar and are therefore presented in a common subsection.

4.2.1 Geometry of the percolative array

We chose to construct the percolative structure from a regular triangular array of 2000 columns times 2310 rows (about $5 \cdot 10^6$ sites), because in a triangular geometry the energy barrier opposing vortex motion is low [27]. The disorder is introduced through site percolation with the use of a program generating random numbers between zero and one [28]. The program covers the lattice structure site by site and, if the given random value happens to be below the chosen percolation fraction p, the site is occupied. Some of the

occupied sites are linked, forming clusters of various sizes; the sites without lead island form holes of different sizes.

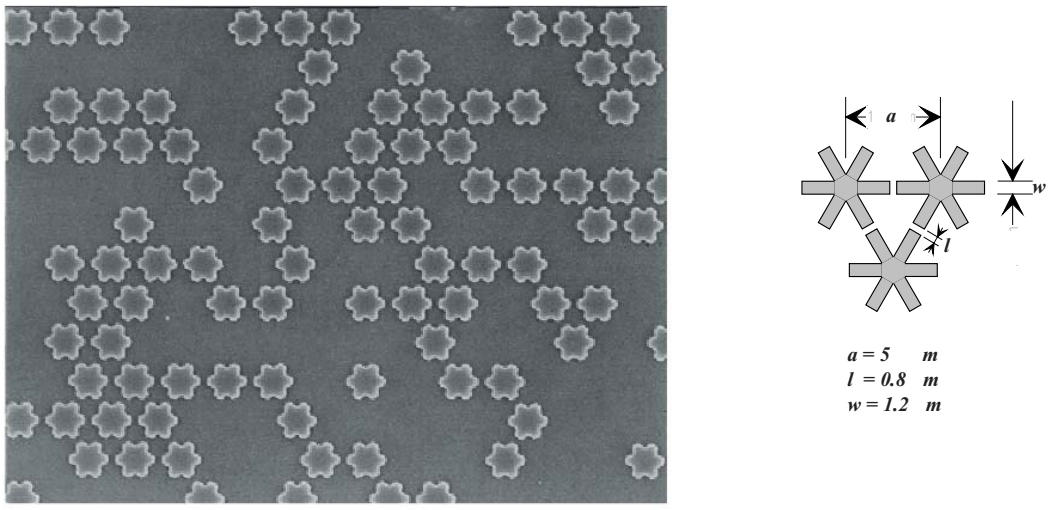

(a) (b)

Figure 4.1: (a) SEM image of a portion of the percolative array. (b) Geometrical characteristics of the superconducting islands. The lattice constant and the gap between the lead islands ($l = 0.8$ μm) are at the lowest possible limit of the definition of our photolithographic equipment.

A SEM image of a small area of the percolative array is shown in Fig. 4.1 (a). One observes that the superconducting islands possess rounded angles. This rounding follows both from the limits of our equipment and from the quality of the optical mask used for the photolithographic process. The gap between two adjacent Pb islands determines the length of the junction $l = 0.8$ μm; the width of the arms is $w = 1.2$ μm and the lattice constant $a = 5\,\mu$m. The thickness of the normal metal (Cu) is 2000 Å, and the Pb islands are 3000 Å thick.

The correlation percolation length ξ_p is one of the main characteristics of percolative disorder. It represents the average size of the largest holes in the percolating cluster (see section 5.2.3), and depends on the percolation fraction through the following relation [3, 4, 5]:

$$\xi_p = b \left(\frac{p - p_c}{1 - p_c} \right)^{-\nu} a, \tag{4.1}$$

where a is the lattice constant, $\nu = 4/3$ a critical exponent for percolation in two dimensions, and b a parameter of order unity determined by the geometry of the array (triangular, square, ...). With the basic triangular structure of our lattice, b is found experimentally to be equal to 0.22 (see later section 5.6.6).

The formula describing the response of the sample, Eq. (3.1), presupposes that the structure of the array is homogeneous at a scale given by the size of the coils. We therefore chose a percolation fraction p far enough from the critical threshold p_c to introduce holes small enough to ensure the homogeneity of the sample area probed by the detection coils. On the other hand p should be chosen sufficiently close to p_c in order to probe the response of the array in the fractal regime. In other words, the value of ξ_p must be big enough to allow measurements of the properties due to the fractal geometry of the sample within the frequency range experimentally accessible. The choice of ξ_p thus represents a compromise between two opposite requirements: observation of a fractal response and a sample homogeneity at a length scale of a few square millimeters. These requirements led us to chose a percolation fraction equal to $p = 0.515$, slightly above the percolation threshold $p_c = 0.5$ for triangular arrays with site percolation in 2D. This corresponds to $\xi_p \simeq 30\ a$. With a lattice constant $a = 5\ \mu$m, we reach an estimate of about 300 ξ_p^2 under the surface of the detection coils, which appears to be sufficient to guarantee sample homogeneity.

We used a program [18] based on the Hohsen-Kopelman algorithm [29] to determine statistical quantities peculiar to our array. In particular, we established the size distribution of the holes and of the clusters defining its structure; we also checked that there is a superconducting percolation path through the sample.

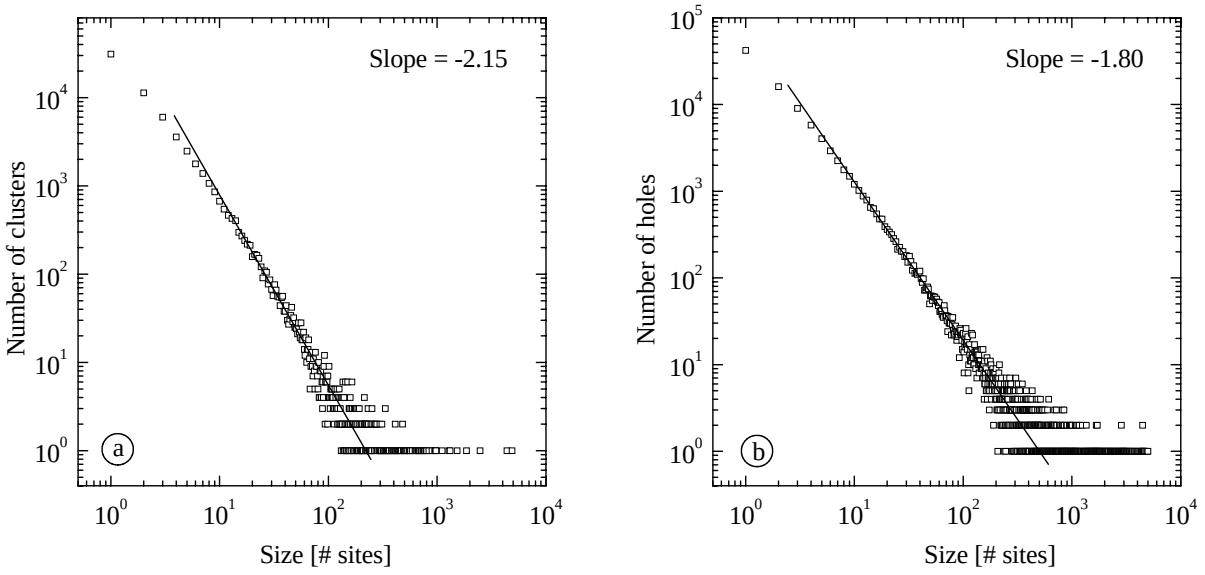

Figure 4.2: (a) Number of clusters in the array as a function of their sizes. (b) Number of holes in the array as a function of their sizes.

The size distributions of the clusters and of the holes in the studied array are shown in Fig. 4.2 (a) and (b) respectively. We will explain in section 5.2 that, for an infinite array at the percolation threshold, these distributions behave as power-laws, both with the

same exponent equal to 2.05 as a consequence of the fractal geometry of the percolative structures [3, 4, 5]. For our array, one notices in Fig. 4.2 that the size distributions obey power-laws for clusters or holes, but with exponents slightly different from the predicted value 2.05. These distributions deviate from power-law behavior for large sizes. This is probably due to the finite size of our array, which influences the statistics of the large structures.

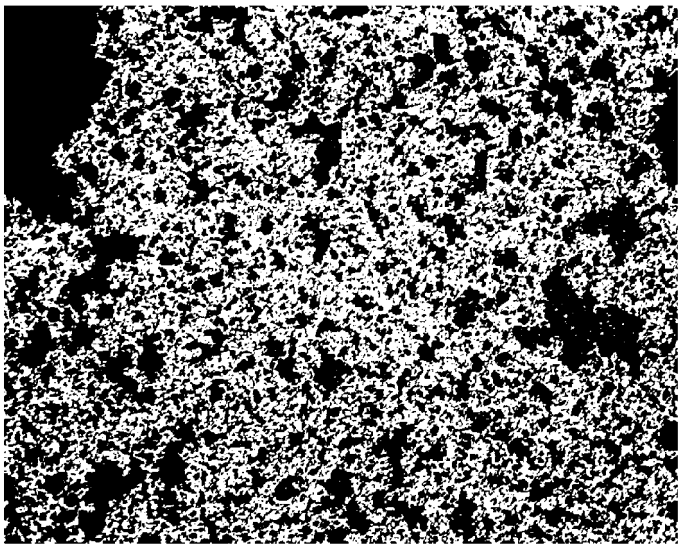

Figure 4.3: Schematic view of the percolating cluster, in white, for a portion of 640×480 sites. This represents about 1/15 of its total surface.

The structure of the percolation cluster for a section representing 1/15 of the total array is shown in Fig. 4.3. The percolating cluster is white, whereas the other sites are black. The array appears relatively dense, even for this percolation fraction close to p_c. This is due to the fact that the percolating cluster is formed in a major part by dangling ends, as discussed in section 5.2.3. This could visually lead to underestimate the size of the holes in the disordered structure.

4.2.2 Geometry of the modulated array

The geometry of the mask used for the study of the modulated array was defined to allow the creation of square arrays whose coupling energy is periodically modulated in one direction. This modulation was obtained by varying by about 10% the gap of one of the junctions of each plaquette, as shown in Fig. 4.4 (b). This leads to a gap $l = 0.81\,\mu$m for the unmodulated junctions, and $l + \Delta l = 0.92\,\mu$m for the modulated junctions; a lattice constant $a = 8\,\mu$m and a wide $w = 2\,\mu$m of the arms were chosen, as shown in Fig. 4.4 (b). The surface of the array covers $1\,\mathrm{cm}^2$, and is occupied by about $1.6 \cdot 10^6$ islands. The thickness of the normal metal (Cu) is 2000 Å, and it is 3000 Å for the lead islands.

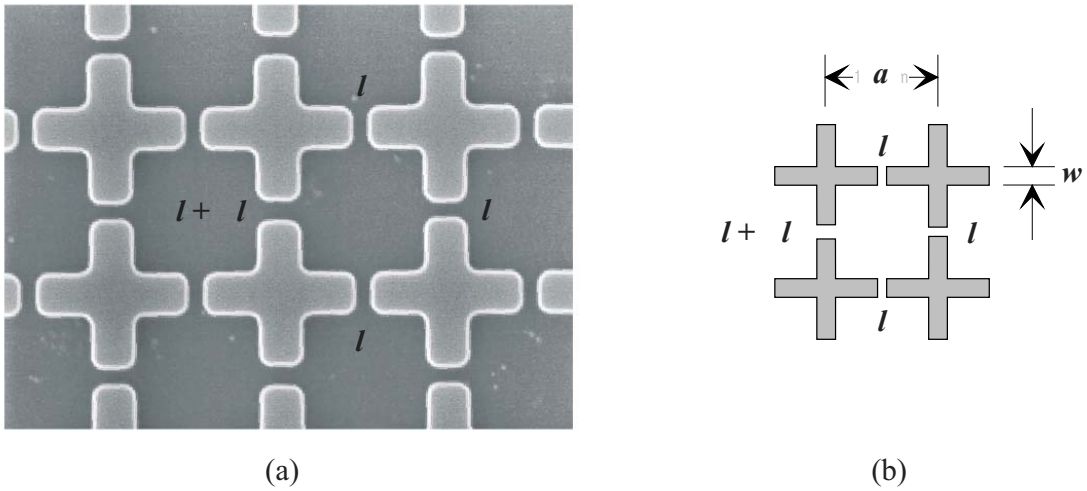

(a) (b)

Figure 4.4: (a) SEM image of a portion of the modulated array. (b) Geometrical characteristics of the lattice. This structure shows a modulation of the length of the junctions in one direction.

4.3 Fabrication of the samples

The first step in the fabrication process is the evaporation on a silicon substrate (diameter $1''$) of a thin film of Cu followed by a thin film of Pb (vacuum better than 10^{-6} Torr before the evaporation). During the evaporation, the transition from the Cu to the Pb must be performed with special care because the electrical contact at the interface of these two metals must be as good as possible. One has therefore to change from one evaporation source to the other very quickly to avoid the formation of an oxide layer between the two metallic films. One next brings the system to atmospheric pressure with Ar or N_2 gas, and covers the bimetallic strip with photoresist. The photoresist is then exposed to UV-light through the mask, and developed to remove the exposed photoresist. The areas of the Pb thin film which are not protected by the photoresist are then removed by argon ion-milling. This process is stopped as soon as the Cu film is visible; this leads to lead islands on a Cu layer according to the pattern of the mask. The last step consists in etching the Cu layer on the edges of the array to obtain contact pads allowing to perform four-probe resistive measurements.

Achieving uniformity of the junctions over the total area of the array is the most difficult aspect of the sample fabrication. The length l of the normal metal between two adjacent superconducting islands should be the same for all the junctions. It indeed determines the critical current of the junctions according to Eq. (2.4), and even a small variation of l leads to large variations of the junction coupling energy. Moreover, the proximity effect is very sensitive to the quality of the interface between the normal metal and the lead. It follows from these two considerations that even the best samples exhibit a certain amount of intrinsic disorder in the junction coupling energy.

4.4 Physical properties of the single junctions

In this section we present the measurements and the analysis allowing to determine the physical parameters of the individual junctions. We will in particular determine the transition temperature T_{cs} of the lead islands and the critical current of the junctions. Using these parameters, it will then be possible to establish the relationship between the real and the reduced temperature.

4.4.1 Percolative array

Resistive transition

The sample is first characterized by a preliminary four-probe resistive measurement, which allows to judge its quality, to determine the transition temperature of the lead islands and to study the general features of the superconducting transition. Fig. 4.5 shows a four-probe resistance vs temperature measurement of the percolative array, performed with an ac current of 0.1 mA at a frequency of 163 Hz. The value of the normal state resistance was calibrated with a dc resistive measurement.

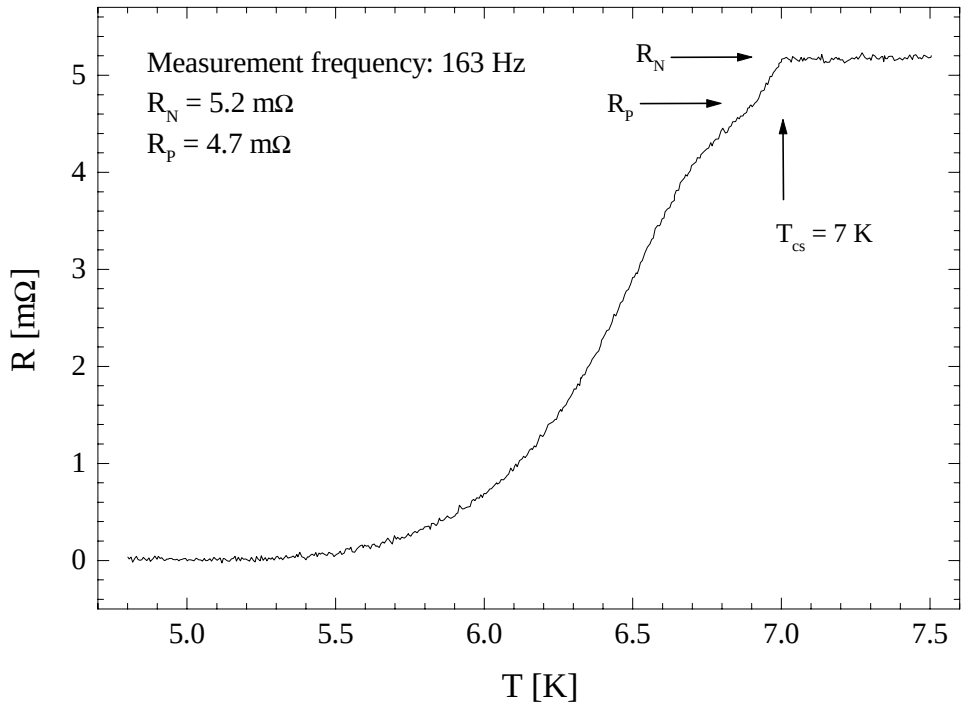

Figure 4.5: Resistance of the percolative sample as a function of temperature, measured with an ac current of 0.1 mA at the frequency of 163 Hz. Notice the relatively long resistive tail present at temperatures below 6.7 K. R_N is the normal state resistance and R_p corresponds to the beginning of the proximity shoulder.

For temperatures above 7 K, one notices the presence of a plateau from which one extracts the normal state sheet resistance of the sample $R_N = 5.2$ mΩ, which turns out to be essentially that of the underlying copper film. With decreasing temperature one observes a transition which occurs in two steps. The transition of the lead islands is clearly evident at a temperature $T_{cs} = 7$ K, and leads to a first decrease of the resistance to a value $R_p = 4.7$ mΩ. It corresponds to the onset of the proximity shoulder, which extends over a temperature interval 6.7 K $\leq T \leq$ 6.9 K where the resistance decreases slowly with temperature. In this region, the proximity effect becomes stronger and increases the superconducting properties of the Cu layer (see Eq. (2.1)).

For temperatures well above T_{cs} the random network can be modeled with the following elements:

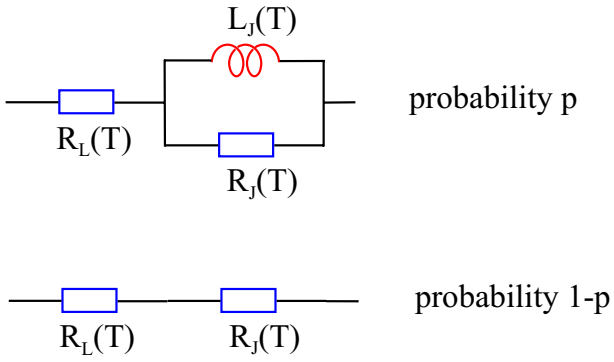

R_L represents the temperature dependent resistance of the normal metal bridge linking two superconducting islands of a junction. Noticing that the value of ωL_J is more than two orders of magnitude less than the sheet resistance of the array at the frequencies of interest, we can describe in good approximation the components of the network by R_L (with probability p) and $R_L + R_J$ (with probability $1-p$). Near the percolation threshold, this leads to a sheet resistance $R(T)$ of the array given by :

$$R(T) \simeq [R_L(T)(R_L(T) + R_J(T))]^{1/2}. \tag{4.2}$$

Just below T_{cs}, we obtain from Eq. (4.2): $R_L \simeq R^2(T_{cs})/R_N \simeq 4.25$ mΩ, which compares favorably with the resistance of the Cu-bridge $R_L \simeq 3.5$ mΩ obtained with the geometrical caracteristics of the junctions.

The coupling between the lead islands, via Josephson effect, becomes appreciable only during the second part of the transition, for temperatures lower than 6.7 K. The superconductivity expends more and more in the copper bridge between the islands, and finally phase coherence sets in across the whole array.

By comparing the measurement shown in Fig. 4.5 with those performed on regular arrays [2, 30], one sees that the resistive transition of percolative arrays shows a smaller proximity shoulder than a regular array. On the other hand the resistive tail extends over a larger interval toward low temperatures.

Determination of the coupling energy - reduced temperature

In this section, we briefly describe the analysis which allows to extract the physical properties of a single junction. In particular, we will find the formula for the junction inductance $L_J(T)$ as a function of temperature. We will deduce from it the relation between the real and the reduced temperature τ, which is needed as an appropriate dimensionless temperature parameter [27].

Consider first a regular JJA in zero magnetic field and at temperatures low enough so that phase fluctuations (spin-waves and vortices) may be neglected. By neglecting the dissipative channel of the junction[1], one obtains the sheet conductance by adapting Eq. (2.8) to the triangular structure of the array:

$$G(T) = \frac{\sqrt{3}}{i\omega L_J(T)}. \tag{4.3}$$

At length scales larger than ξ_p (i.e. at sufficiently low ω), the influence of disorder can be taken into account by treating our disordered array as a regular weakened array [18]. In this approach, the relationship between the measured inductance $L_\square$ and the inductance of a single junction L_J is given by a percolation dependent factor:

$$L_\square^{-1}(T) = \sqrt{3}\beta L_J^{-1}(T) \left(\frac{p-p_c}{1-p_c}\right)^{\mu} b^{-\zeta} \tag{4.4}$$

where μ and ζ are two critical exponents: $\mu \simeq 1.30$ and $\zeta \simeq 1$ in two dimensions [3]. The constant $b^{-\zeta} \simeq (0.22)^{-\zeta} \simeq 4.5$ was deduced experimentally by setting the energy barrier for vortex motion to its theoretical value (see later section 5.6.2), and β is some unknown coefficient of the order of one. Assuming $\beta = 1$ and using Eq. (2.4), it is then possible to relate the measured sheet conductance $L_\square(T)$ at low temperatures and for the low frequencies to the critical current of a single junction:

$$L_\square^{-1}(T) = \sqrt{3}\frac{2e}{\hbar} b^{-\zeta} \left(\frac{p-p_c}{1-p_c}\right)^{\mu} I_C(0) \left(1-\frac{T}{T_{cs}}\right)^2 e^{-|c|\sqrt{T}}. \tag{4.5}$$

[1] A posteriori it turns out that $\omega L_J \ll R_J$ at the frequencies of interest

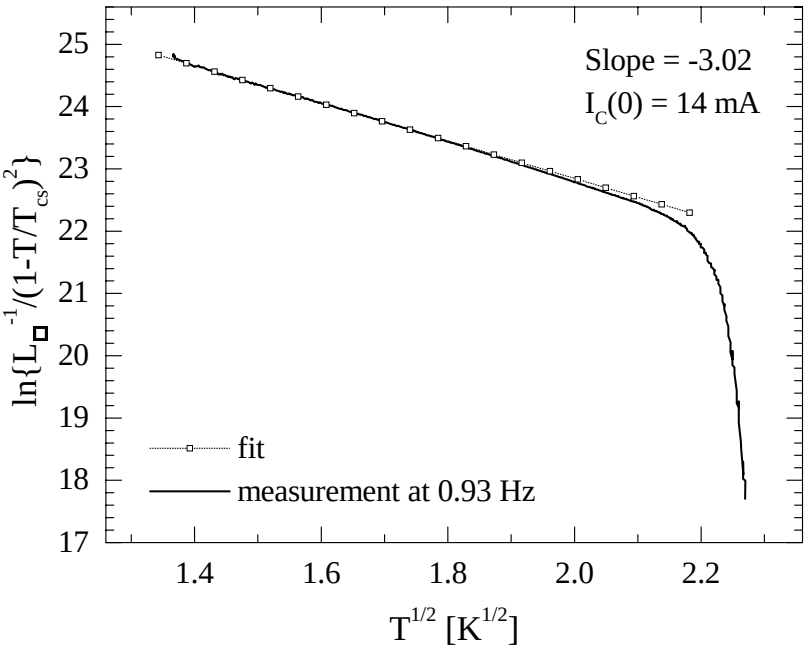

Figure 4.6: Typical example of the fit with the de Gennes expression, to extract the value of the critical current $I_C(0)$.

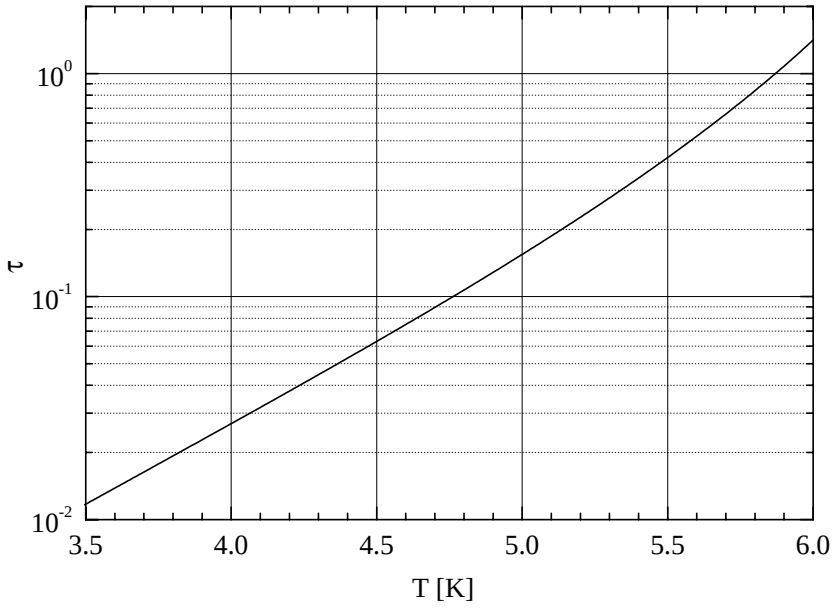

Figure 4.7: Linear-log plot of the reduced temperature τ as a function of the real temperature T in the typical temperature range of the measurements for the percolative array.

By fitting the data to Eq. (4.5) (a typical example is shown in Fig. 4.6), we deduce [20] the values of the critical current $I_C(0) = 14$ mA and $c = 3.02$ K$^{1/2}$. It's then possible to link the measured temperature T to the reduced temperature $\tau = k_B T/E_J(T) = (2\pi/\phi_0)^2 k_B T L_J(T) = 2ek_BT/(\hbar I_C(T))$. This leads to the curve shown in Fig. 4.7.

To conclude, we recall that the validity of the curve shown in Fig. 4.7 is somewhat limited since the theoretical expression for $E_J(T) = \hbar I_C(T)/(2e)$ (Eq. (2.4)) is, strictly speaking, only valid near T_c.

4.4.2 Modulated array

Resistive transition

The four-probe resistance vs temperature measurement of the modulated array is shown in Fig. 4.8. It was performed with an ac current of 0.1 mA at a frequency of 84 Hz. Its general trend is very similar to that of the percolative array, except for the proximity plateau which extends over a wider temperature interval; we can therefore explain the shape of the curve shown in Fig. 4.8 by using the considerations of section 4.4.1.

The resistance is 4.3 mΩ in the normal state, and decreases to about 3 mΩ when the proximity plateau is reached. The transition temperature of the lead islands T_{cs} is 7.02 K.

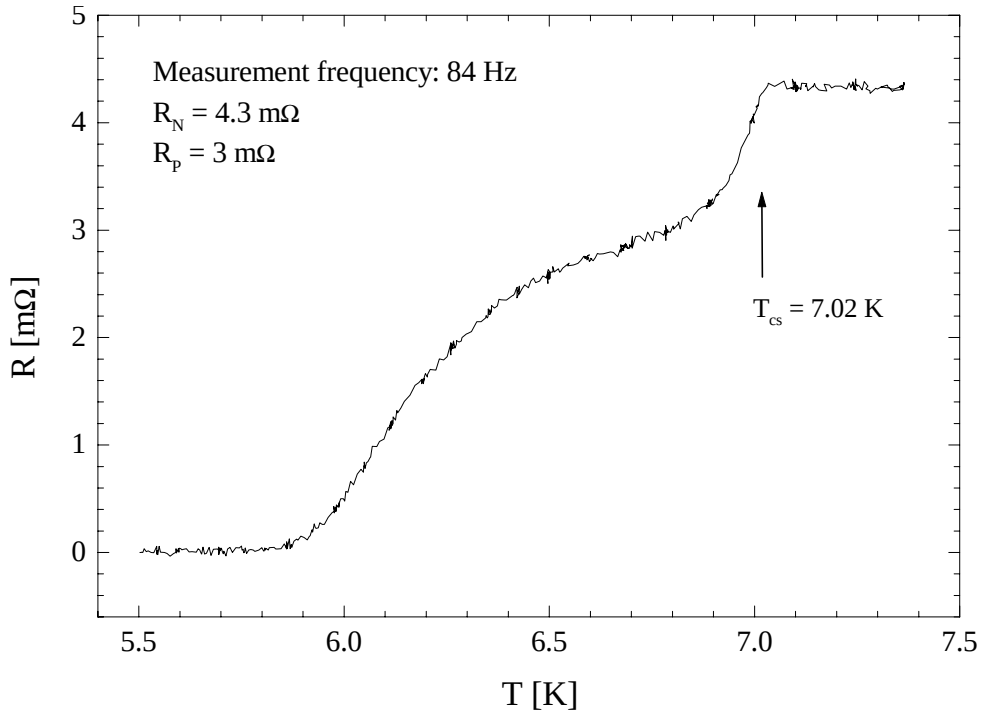

Figure 4.8: Resistance of the modulated sample as a function of temperature, measured with an ac current of 0.1 mA at the frequency of 84 Hz. R_N is the normal state resistance and R_p corresponds to the beginning of the proximity plateau.

Determination of the coupling energy - reduced temperature

Relating the measured conductance at low temperature to the single junction conductance is more complicated for modulated arrays than for percolative arrays. We have to take into account the anisotropy of the array by introducing a modulation parameter $\eta(T)$ and to consider the arithmetical mean of the conductances of the modulated and unmodulated junctions. This is discussed in detail in section 6.1.4, and leads to the following relationship between the array inductance $L_\square$ and the inductance L_J of an unmodulated junction:

$$L_\square^{-1}(T) = \frac{3+\eta}{4}\, L_J^{-1}(T) = \frac{2e}{\hbar}\,\frac{3+\eta}{4}\, I_C(0)\left(1-\frac{T}{T_{cs}}\right)^2 e^{-|c|\sqrt{T}}. \tag{4.6}$$

By fitting the data in a similar way than for the percolative array, we deduced from Eq. (4.6) a critical current $I_C(0) \simeq 100$ mA and $c = 3.8$ K$^{1/2}$. $\eta(T)$ was calculated by using Eq. (6.5) with $\Delta l \simeq -0.1$ μm and $\xi_N = 810$ Å. It is then possible to link the measured temperature T to the reduced temperature $\tau = k_B T/E_J(T)$. This leads to the curve shown in Fig. 4.9.

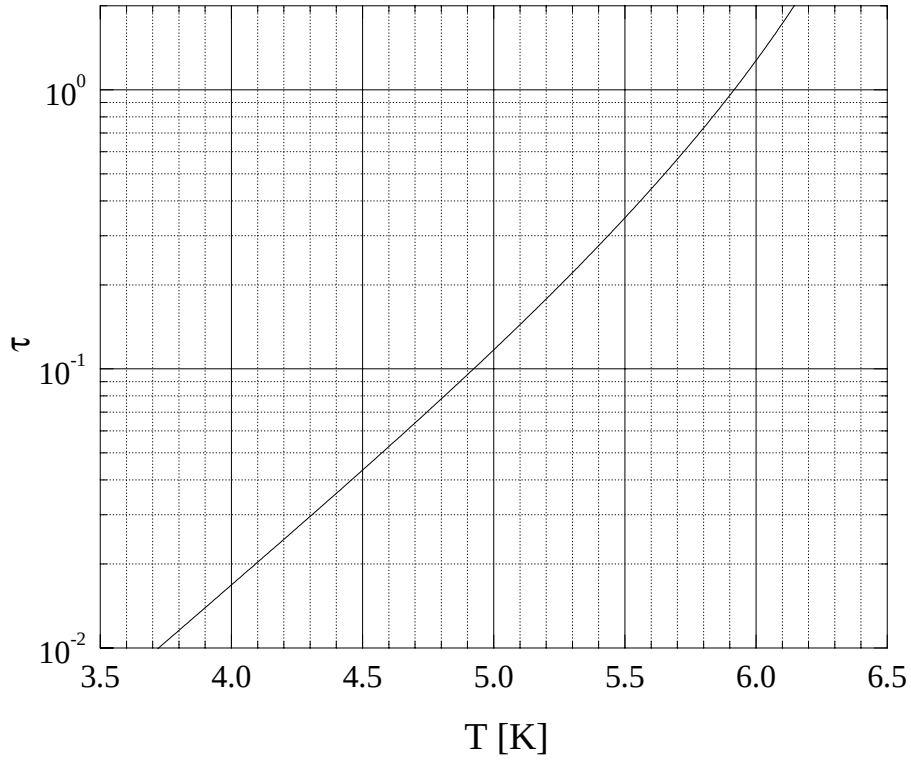

Figure 4.9: Lin-log plot of the reduced temperature τ as a function of temperature T in the temperature range of our measurements, for the modulated array.

Chapter 5

Percolative arrays

5.1 Introduction

The work presented in this chapter falls within the scope of research on JJAs having a fractal geometry. These investigations started with the study of Sierpinski gasket arrays [49, 50, 22], continued with the characterization of the response of percolative arrays at temperatures well below the critical temperature [53, 18, 54, 55], leading naturally to study the properties of percolative arrays in a higher temperature domain [56, 57, 58, 59]. The main purpose of this chapter is to present measurements performed on a percolative array near the percolative threshold in a temperature region close the transition. Moreover, we succinctly expose the theoretical approaches used to discuss our experimental results.

This chapter consists of five main parts. The first one is devoted to percolation theory. In the second part we show the frequency dependence of the sheet conductance well below the critical region in zero field. In the third part we show measurements performed at temperatures well below the transition temperature and at small frustration. We next discuss, in section 5.5, the array response in a domain close to the critical temperature. Measurements performed at higher temperatures are presented in section 5.6.

5.2 Notions of percolation

5.2.1 Purpose of this section

Percolation theory is one of the simplest models to describe disordered structures, and is applicable to many domains. The concept of percolation was first introduced about 50 years ago by Flory [31] and Stockmayer [32] when studying the gelation process. The first geometrical and statistical concepts were considered by Broadbend and Hammersley [33] in connection with the study of diffusion of fluids in random media. The introduction of fractal concepts [34], and the development of computers have significantly contributed to the present understanding of percolation.

We first mention general notions related to percolative systems, and concentrate afterwards on structural properties near the percolation threshold. We will finally consider transport properties peculiar to the fractal regime.

Although percolation theory is applicable to many three-dimensional systems, we will confine ourselves to study the two-dimensional case. A more complete description of the percolation theory and a rigorous derivation of the expressions presented below may be found in references [3, 4, 5].

5.2.2 Introduction to percolation theory

Consider an infinite triangular lattice, where each site is randomly occupied with probability p and empty with probability $1 - p$. The percolation fraction p is thus the ratio between the occupied sites and the total number of sites of the lattice. At low concentrations p, the occupied sites are either isolated or form small clusters of nearest-neighbors, and no path connecting opposite edges of the lattice exists (see Fig. 5.1). With increasing p, the mean cluster size increases up to the appearance of an infinite cluster which connects opposite edges of the lattice. This percolating cluster is sometimes called the infinite cluster, and appears at a critical concentration p_c. When p is further increased, more and more sites become part of the infinite cluster, and the average size of finite clusters decreases. Finally, at $p = 1$, all sites belong to the infinite cluster.

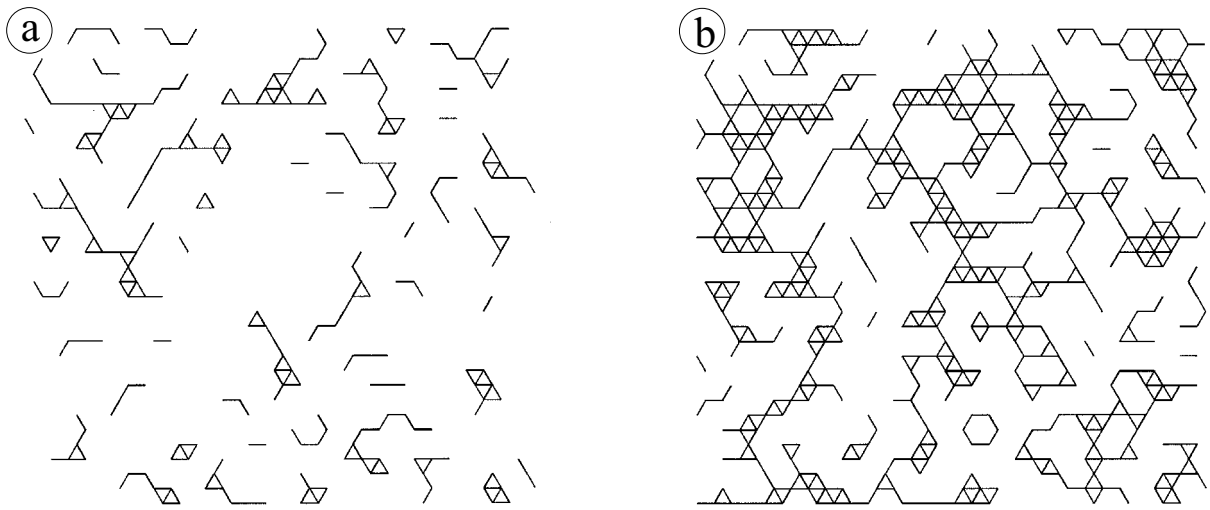

Figure 5.1: (a) Site percolation in a triangular array for the percolation fraction $p = 0.3$. Occupied sites are isolated or form small clusters. (b) Triangular array with site percolation for a concentration p slightly above the percolation threshold $p_c = 0.5$. Notice the appearance of a percolating cluster connecting the opposite edges of the lattice.

The threshold concentration p_c is called the percolation threshold, or, since it separates

two different phases, the critical concentration. The percolation transition can therefore be seen as a geometrical phase transition for which the critical concentration p_c separates a phase characterized by finite clusters ($p < p_c$) from a phase characterized by the presence of an infinite cluster ($p > p_c$). In percolation, the concentration p of occupied sites plays the role of the temperature in thermal phase transitions [35, 3]. By analogy, one expects that the typical quantities associated with the percolative transition are described by power-laws with critical exponents. The percolative threshold p_c depends on the structural details of the lattice (square, triangular,...), on its dimension, and on the type of percolation (site, bond,...). For site percolation in a triangular two-dimensional array, one can show analytically [3] that $p_c = 0.5$.

There are several kinds of percolative structures depending on the dimension of the system and on the way used to introduce disorder. In the previous example, we considered disorder due to a random occupation of the sites. In this case we speak of site percolation, in opposition to bond percolation which corresponds to random presence of bonds between the sites. One can also think to the case of continuum percolation, where the positions of the sites are not restricted to the discrete sites of a regular lattice (e.g.: Swiss cheese model).

5.2.3 Structural properties near p_c

Distribution of cluster sizes

Percolation is a random process and will therefore be characterized by statistical quantities. The first problem we consider is the distribution of cluster sizes at fixed percolation fraction. There is no method to rigorously determine this distribution in the general case, we can at best offer a generalization, guessed from results for special cases. Let us therefore assume (scaling Ansatz) that the mean number of clusters of size s normalized by the size of the lattice, $n_s(p)$, is given near p_c by [3]:

$$n_s(p) \sim s^{-\tau} f_{\pm}(|p - p_c|^{1/\sigma} s), \tag{5.1}$$

where s is the number of sites belonging to the cluster, τ and σ are critical exponents which depend only on the dimension. The scaling function $f_{\pm}(z)$ depends on the other hand on the lattice structure (triangular, square, ...) and on the type of percolation (bond, site, ...) and must therefore be determined numerically for each system. A satisfactory approximation for $f_{\pm}(z)$ is given by a decreasing exponential, leading to a distribution of clusters sites of the type:

$$n_s(p) \sim s^{-\tau} e^{-cs} \quad \text{with} \quad c \sim |p - p_c|^{1/\sigma}. \tag{5.2}$$

This approximation allows to separate the clusters into two groups: clusters of size $s \leq 1/c$ which are numerous enough to contribute significantly to the relevant quantities describing percolation, and clusters of size $s \gg 1/c$ which are exponentially rare. Eq. (5.2) thus defines a characteristic cluster size $s_\xi = 1/c$ which can be identified as representing a crossover from the behavior of " critical " clusters to that of " non-critical " ones. Notice that at the percolation threshold, $n_s(p) \sim s^{-\tau}$ with $\tau \simeq 2.05$ [5].

Cluster structure near p_c

Eqs. (5.1) and (5.2) allow a rigorous calculation of several quantities, such as the mean number of sites of finite clusters S, the probability that an occupied site belongs to the infinite cluster P_∞, or the correlation length ξ_p, sometimes also called connectivity length. These quantities behave as power-laws near the percolation threshold. They are respectively characterized by the exponents γ, β, and ν, which are universal in the sense that they depend neither on the structural details of the lattice, nor on the type of percolation but only on the dimension of the lattice. There are thus several exponents related to various quantities which diverge near p_c, but there exist relations between these exponents and the third may be obtained from the knowledge two.

The cluster structure near p_c can be partially characterized with the help of the correlation length. To calculate ξ_p, one introduces the radius of gyration R_g associated with a cluster of size s:

$$R_g^2(s) \equiv \sum_{i=1}^{s} \frac{|\vec{r}_i - \vec{r}_0|^2}{s}, \tag{5.3}$$

where $\vec{r}_0$ and $\vec{r}_i$ represent respectively the position of the center of mass and the position of the site i of the studied cluster. R_g is the radius of a ring formed by s sites having the same angular momentum as the cluster, it gives an idea of its size. By averaging R_g over all clusters of a given size s, one obtains an averaged gyration radius for a class of clusters of size s. It represents the average distance between two sites which belong to the same cluster. The correlation length is then defined as the average gyration radius weighted by the size distribution $n_s(p)$:

$$\xi_p^2 = \frac{2\sum_s R_g^2(s) s^2 n_s}{\sum_s s^2 n_s}. \tag{5.4}$$

It's possible to show that this quantity behaves like a power-law near the percolation threshold [4], with an exponent $\nu = 4/3$ in two dimensions defined by:

$$\xi_p \sim |p - p_c|^{-\nu}. \tag{5.5}$$

As we discussed about Eq. (5.2), the geometrical quantities diverging near p_c depend principally of clusters of sizes of order of s_ξ. We now see (Eq. (5.4)) that the correlation length, which is also one of these quantity, is the radius of those clusters which contribute mainly to the divergences. One can so associate ξ_p to the length dominating the critical behavior associated with the percolation transition.

In a more intuitive interpretation, that will be adopted in the following of this section, one associates ξ_p with the size of the largest hole of the lattice for $p > p_c$ and of the largest cluster for $p < p_c$. Using this interpretation, we establish in the next section that the properties of percolative arrays are different at length scales larger or smaller than ξ_p.

Infinite cluster near p_c

With our measurement technique, the response of the sample is mainly generated by the percolating cluster. It is therefore important to characterize its structure in a more detailed way.

We have seen in the previous section that ξ_p is the length dominating the system, and that it diverges near the percolation threshold. For percolation fractions close enough to p_c, the correlation length will therefore have a large value, and it will be possible to ignore the existence of a finite ξ_p at sufficiently small length scales. In the absence of any basic length scale to use as a " measuring stick ", the lattice will then appear the same at all scales of observation. If we select a part of it and arbitrarily enlarge this portion, it will possess the same statistical properties that the whole system. This property of self-similarity, at length scales larger than the unit size and smaller than ξ_p, is characteristic of fractal geometries. A particularity of fractal systems is their non-integer dimension, the fractal dimension d_f. It can be calculated with the help of the universal exponents introduced previously by the relation [3]:

$$d_f = d - \frac{\beta}{\nu} \quad , \tag{5.6}$$

where d represents the Euclidean dimension of the lattice. This formula gives a value $d_f = 91/48$ for $2d$ percolation systems. If $M(r)$ is the number of sites belonging to the percolating cluster within a sphere of radius r, the fractal dimension describes how, on average, $M(r)$ scales with r:

$$M(r) \sim r^{d_f}. \tag{5.7}$$

For percolation concentrations slightly above p_c, we have seen that ξ_p represents the linear size of the largest holes in the infinite cluster. Since ξ_p is finite above p_c, the infinite cluster can be self-similar only on length scales smaller than ξ_p [36]. We can therefore interpret ξ_p as a typical length up to which the infinite cluster is self-similar and can be regarded as a fractal. For length scales larger than ξ_p, its structure is that of an homogeneous two-dimensional system composed of several unit cells of size ξ_p.

As discussed above, the infinite cluster may be divided into boxes of size ξ_p. Inside each box the geometry of the cluster looks like that of the infinite cluster at p_c. But this cluster is very weak: removal of a few bonds can break it into finite clusters. This weakness leads to postulate that within each box of size ξ_p there is practically only one chain of bonds connecting opposite edges. This leads to a model of nodes at a distance ξ_p from each other connected by effectively one-dimensional links. But this model is incomplete: we must also take into account two kinds of structures which appear at scales smaller than ξ_p. First, there are loops of all sizes smaller than ξ_p between singly connected nodes. Secondly, there are dangling ends, which are the parts connected by one extremity only to the infinite cluster.

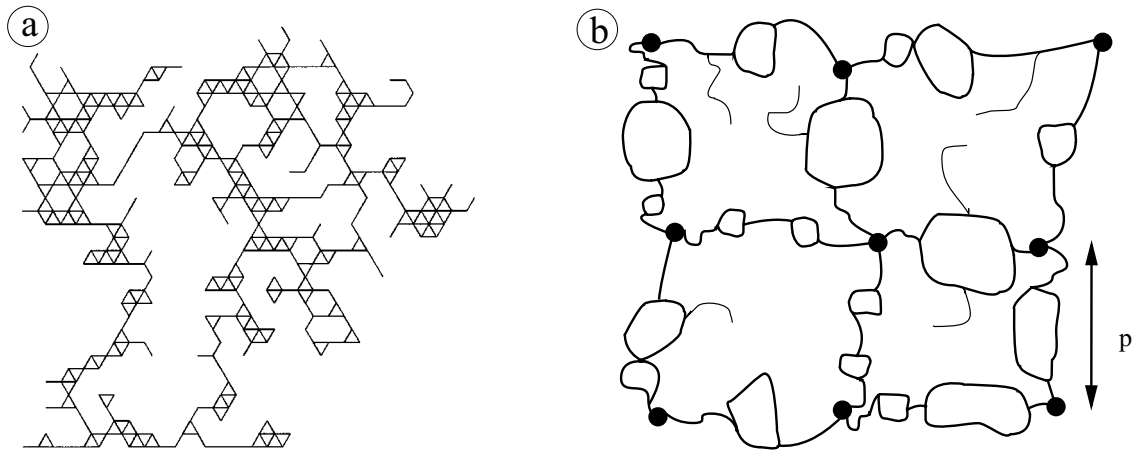

Figure 5.2: (a) Large percolating cluster in a triangular array with site percolation for a percolation fraction slightly above p_c. Notice the presence of many dangling ends, and of holes of various sizes. (b) Schematic picture for the links (one-dimensional chains), nodes (crossing points of the links) and blobs (self-similar dense regions with more than one connection between two points) of the infinite cluster slightly above p_c. The distance between the nodes as well as the maximum blob diameter are assumed to be of the order of ξ_p. The thin lines are the dead ends which form in fact most of the percolating cluster.

All the above arguments lead to the links-nodes-blobs model [37] shown schematically in Fig. 5.2. This picture consists therefore of nodes separated by ξ_p, connected by generalized links, which contain both singly connected bonds and blobs. Moreover, many dead ends are present in the structure.

There are several models of deterministic fractals which imitate the disordered structure of percolation systems and which can be used to describe analytically the geometrical properties of the percolation cluster. To capture the basic features of the percolation cluster at scales smaller than ξ_p, it is thus useful to introduce a simple geometrical model which possesses a hierarchical structure [45, 46]. Let's consider the hierarchical lattice model shown in Fig. 5.3. One starts at step $N = 0$ with a single bond of length $l(N = 0)$. At $N = 1$ this bond is replaced by four bonds of length $l(N = 1)$, two in parallel and two in series. This structure is the unit cell. At $N = 2$ each bond is replaced by the unit cell, and this process is next iterated at each step, with the Nth level being achieved by replacing each bond in the $(N-1)$th level by the unit cell. The iteration index N can be seen as a parameter which controls the effective linear dimension $l(N)$ of the hierarchical lattice.

The resulting structure is a self-similar fractal made of singly connected bonds, termed links below, and multiply connected blobs, but without dangling ends. A link is defined as one which, if cut, renders a part of the network disconnected. For this model we can calculate quantities such as the number of bonds $N_B = 4^N$ or the number of links $L_1 = 2^N$ between the extreme ends of the hierarchical lattice. By using the expression for L_1, it's

then possible to find a quantitative relationship between the iteration index N and the physical length scale $l(N)$ shown schematically in Fig. 5.3. A natural way to accomplish this goal is to use the fact that the number of links varies as $(L/l)^{1/\nu}$ for a finite-size system of total linear dimension L [43]. Since the number of links is also given by 2^N for a Nth-order hierarchical lattice, we can infer that the effective linear dimension l is given by $l(N) = 2^{-N\nu}L$ for the hierarchical model, or equivalently by:

$$l(N) = 2^{-\nu} l(N-1). \tag{5.8}$$

This last relationship expresses the scale invariance characterizing the fractal structures, which allows to consider a hierarchical structure of order N as formed by 4 identical substructures of order $N-1$. This aggregation process will allow to establish recursive relationships between the variables appearing in the hierarchical system.

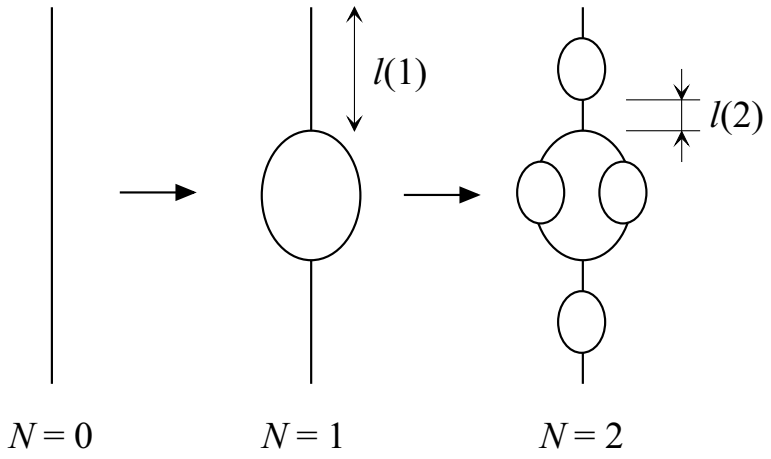

Figure 5.3: The first levels of iteration in the hierarchical lattice model. The first order structure ($N = 1$) represents the unit cell and is substituted for each bond at a given level to generate the next level. $l(N)$ represents a length scale which decreases as $l(N) = 2^{-\nu} l(N-1)$ at each iteration. The resulting model is self-similar up to the scale of the entire system and provides an accurate representation of the percolating cluster at scales smaller then ξ_p.

To conclude this section, notice that we could have used other non-random fractal structures, for example the Sierpinski gasket, to mimic the critical behavior of the infinite cluster. We have nevertheless used the model of Fig. 5.3 because the hierarchical embedding of links and blobs provides an accurate representation of the geometric features of the percolating cluster. In particular, the resulting critical behavior provides excellent approximations for the critical exponents of two-dimensional percolation [46].

5.2.4 Transport in fractal structures

In this section we present some dynamical properties of percolation systems. We show in particular that the laws describing the dynamics in a percolation structure near p_c are

modified and obey an anomalous behavior. We restrict ourselves to the description of two physical processes (the conductivity of a disordered network of resistances and the vibrational excitations of a disordered array) which will be useful for the discussion of our measurements.

Conductivity of random networks

Let us assume that the percolating cluster shown in Fig. 5.2 is formed by metallic bonds of equal resistances. If we apply a dc voltage difference between its opposite edges, an electric current will flow through the lattice structure. Naively, one could think that the conductivity $G(p)$ of such a system is proportional to the probability P_∞ that an occupied site belongs to the percolating cluster for any p. But the first transport experiments [38] showed that this is not the case. This is understood by realizing that the dangling ends of the percolating cluster do not take part in the transport phenomena, because they lead nowhere, and that a great part of the percolating cluster belongs to the dead ends. We must therefore introduce another critical exponent μ to describe the behavior of the conductivity G near the percolation threshold:

$$G \sim |p - p_c|^\mu. \tag{5.9}$$

To-date, there is no analytical expression linking the conductivity exponent μ to the exponents describing the previously defined static quantities. Its value for two-dimensional systems can nevertheless be estimated with the help of numerical simulations, which give a value $\mu \simeq 1.30$. The validity of Eq. (5.9) is limited to systems which appear homogeneous, i.e. when the probed length scale is much larger than ξ_p. For sizes L_p smaller than ξ_p or when $p = p_c$, the behavior becomes size-dependent [4] and the formula for the conductivity is given by $G \sim L_p^{-\mu/\nu}$.

Vibrational excitations

Consider first a regular array ($p = 1$) where nearest-neighbors are coupled by springs. If the sites of the lattice can perform local movements around their equilibrium positions, then the system possesses vibrational excitations. In regular networks these excitations are spread over the whole sample and can be called phonons [44], by analogy to the excitations appearing in a crystal lattice.

If we consider a percolating system slightly above p_c, then the excitations will move slowly. This is due to the fact that some parts of the percolating array remain dense, whereas others are strongly affected by disorder and are much weaker. Then, even if long wavelength excitation modes remain present in this percolation system, its behavior will be strongly affected by disorder.

For such lattices with percolation fractions slightly above p_c, we can therefore expect an Euclidean homogeneous regime dominated by phonon-like excitations if the probed length scales are larger than ξ_p. If the probed length scale is decreased below ξ_p, the dynamics will cross to a regime showing the influence of the fractal geometry [53].

5.3 Response well below T_c at zero frustration

In this section we discuss the response of disordered arrays in zero magnetic field and at temperatures well below the critical region. The results shown here have been obtained [53] by measuring the linear sheet conductance $G \equiv (i\omega L_\square)^{-1} + R_\square^{-1}$ of an array with $p = 0.51$, slightly different from the percolation fraction $p = 0.515$ of our array, but also very close to the threshold p_c. We expect thus that they exhibit similar behaviors.

Let us consider an unfrustrated percolative array at temperatures low enough so that thermally created vortices are irrelevant. In this case, the array can be modeled by a two-component random network [53] of conductance G_1 or G_2, with probability p and $(1-p)$ respectively. The conductance of a junction is $G_1 = (i\omega L_J)^{-1} + R_J^{-1}$ and results from the junction inductance L_J in parallel with the junction resistance R_J. Notice that L_J is the same for all the junctions because we consider the response at low temperatures, where the phase differences across the junctions are small. The conductance of the unoccupied sites is $G_2 = R_J^{-1}$ and is therefore simply given by the resistance of the normal metal layer. To calculate the conductance G, we have to consider two different limits taking into account the disordered structure of the array:

- at scales smaller than ξ_p, the geometry of the array is fractal and consequently G is expected to obey a power-law, reflecting the self-similar structure of the system. For bond percolation on a square two-dimensional lattice, the conductance at the percolation threshold can be calculated exactly [39, 40]: $G = (G_1 G_2)^{1/2}$. According to the " universality hypothesis ", this result should also be valid for the site percolation present in our sample and we then obtain, substituting G_1 and G_2:

$$L_\square^{-1} = c_L L_J^{-1} (\omega\tau_J)^{1/2} \quad \text{and} \quad R_\square = c_R R_J (\omega\tau_J)^{1/2} \tag{5.10}$$

  where $\tau_J = L_J/R_J$, and c_L and c_R are two numerical coefficients of order unity;

- at scales larger than ξ_p, the array shows a regular Euclidean structure, leading to a two-dimensional regime where both $L_\square^{-1}$ and $R_\square$ are expected to be length scale independent, and therefore independent of frequency. Using general scaling arguments and denoting by L_0 and R_0 the sheet inductance and the sheet resistance in the limit $\omega \to 0$, we find [18]:

$$\begin{aligned} L_\square^{-1}(\omega \to 0) = L_0^{-1} \simeq 4.5[(p-p_c)/(1-p_c)]^\mu L_J^{-1} \quad \text{and} \\ R_\square(\omega \to 0) = R_0 \simeq 4.5[(p-p_c)/(1-p_c)]^\mu R_J \ , \end{aligned} \tag{5.11}$$

  where $\mu \approx 1.3$ is the conductivity exponent for percolation in two dimensions, and the prefactor 4.5 is an estimate deduced by setting the energy barrier for vortex motion to its theoretical value (see later section 5.6.2).

With increasing frequency, or, equivalently, at decreasing length scale, we thus expect a crossover from a two-dimensional Euclidean regime, independent of ω, to a fractal regime

characterized by a power-law frequency dependence. The crossover occurs at a frequency ω_c corresponding to a length scale of ξ_p.

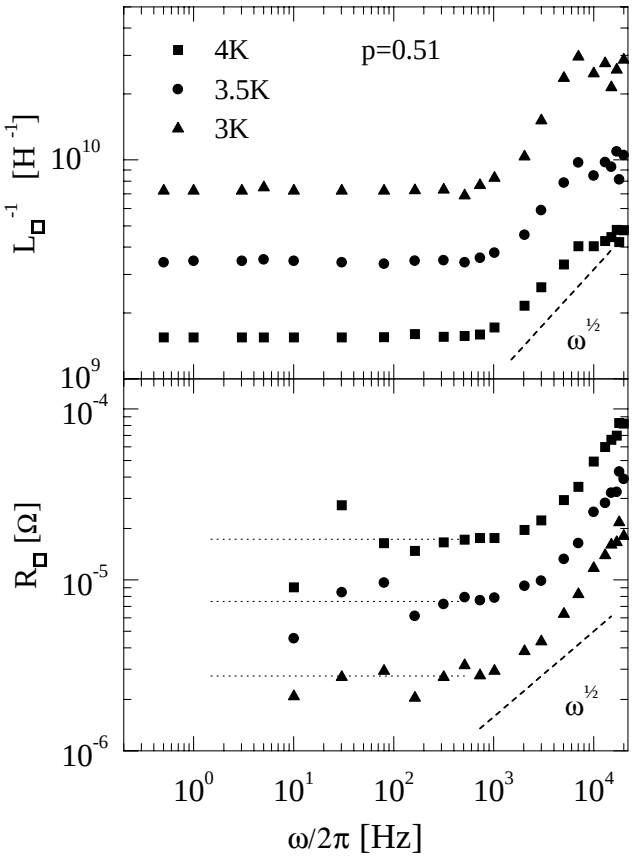

Figure 5.4: Frequency dependence of the inverse sheet inductance and of the sheet resistance in zero field at three different temperatures well below the critical region [53]. The dotted lines are guides to the eye to identify the low-frequency plateaus of $R_\square(\omega)$.

We show in Fig. 5.4, on a log-log plot, the frequency dependence of $L_\square^{-1}$ and $R_\square$ at temperatures well below the critical region, measured for a disordered array with $p = 0.51$ [53]. Both $L_\square^{-1}$ and $R_\square$ exhibit a similar behavior with increasing frequency. At frequencies smaller than $\omega_c \approx 1kHz$, the data are independent of ω in agreement with Eq. (5.11). In this frequency range, the response is dominated by extended "phononlike" modes of the phase system, occurring in the two-dimensional Euclidean regime. A profound change in phase dynamics occurs at ω_c, when the frequency-dependent length scale at which we are probing the system becomes of the order of ξ_p. Both $L_\square^{-1}$ and $R_\square$ become frequency dependent, and behave as power laws with exponents close to 1/2. This dynamical behavior, as predicted by Eq. (5.10), corresponds to the fractal regime, where localized "fractonlike" phase excitations lead to anomalous dynamics.

5.4 Corrections to the array inductance at small frustrations

5.4.1 Purpose of this section

In this section we perform a perturbation calculation of the phases of the superconducting wavefunctions associated with each island of the array, by assimilating the percolative structure of our lattice with the hierarchical links and blobs model [45, 46] introduced in section 5.2.3. The underlying idea will be to use the scale invariance peculiar to the fractal structures to consider a hierarchical structure of order N as being formed by the connection of 4 hierarchical structures of order $N-1$. In the limit of weak frustrations (i.e. when the smallest loops of junctions are free from vortices), this structural property will allow to take the influence of the smallest loops of junctions into account by the use of renormalized coupling constants. In this way, we will find recursive relationships between the renormalized coupling constants appearing at each decimation step. This will allow to establish the asymptotic corrections to the inductance of the array in the limit of small frustrations for temperatures well below the critical region. These predictions will then be compared with experimental results, as discussed in section 5.4.4.

The system must fulfill two preliminary conditions for the theoretical approach to be valid:

- the temperature of the array of junctions must be far below the critical temperature, so that there are no thermally nucleated vortices and so that the activation energy of field induced vortices is small compared to the pinning energy, allowing to assume that the vortices are pinned by the potential provided by the network. In this situation, the dissipative phenomena related to the dynamics of excitations can be neglected, and the array of junctions can be approximated by an array of inductances with different values. The changes in the response of the array as a function of an applied magnetic field are in this case only due to frustration phenomena, linked to the position of field induced vortices in the structure of the array;

- the probed length scales must correspond to the fractal domain. As discussed in section 5.2.3, this condition corresponds geometrically to length scales smaller than ξ_p. To fulfill this condition, we will therefore consider frustrations larger than that corresponding to 1 vortex per loop of area ξ_p^2. Moreover, we will only be interested in the changes of the inductance of the array in the limit of small frustrations. This will allow us to assume that the smallest loops are not filled by vortices.

5.4.2 Modeling of the array of junctions

In section 5.2.3 we established that several properties of the structure of the percolating cluster can be reproduced with the help of the hierarchical links and blobs model [45, 46] for lengths smaller than ξ_p. Let us assume that the left-hand side of Fig. 5.5 represents a

part of the percolating cluster. The crosses are at the positions of the junctions, and the phase of the superconducting order parameter at site i is φ_i.

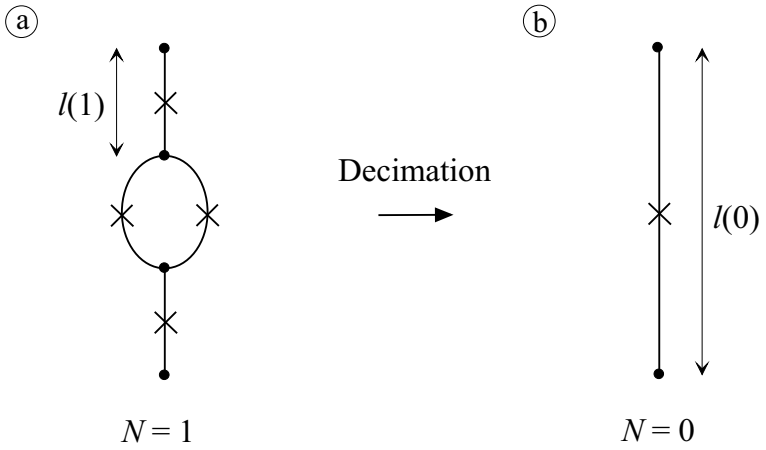

Figure 5.5: (a) Schematic representation of a part of the percolating cluster with the hierarchical model. The phases of each site are noted φ_i $(i = 1, .., 4)$, and the positions of the junctions are depicted by crosses. (b) Hierarchical structure of order $N = 0$ obtained after the decimation of the structure of order $N = 1$. $l(N)$ represents the characteristic length associated with the hierarchical structure of order N.

In the relevant temperature domain well below the critical temperature and at our relatively low measurement frequencies, the dissipative component of the impedance of the single junction is negligible if compared to the inductive component. The junction between the sites i and j is in this case modeled solely by an inductance L_{ij} [22]:

$$L_{ij} = \left(\frac{\hbar}{2e}\right)^2 \frac{1}{V''(\vartheta_{ij})}. \tag{5.12}$$

This relationship indicates that the inductance L_{ij} depends on frustration through the second derivative of the interaction potential $V(\vartheta_{ij})$ which describes the coupling between two neighboring sites $< ij >$ in terms of the frustration dependent gauge invariant phase difference. For SNS junctions, $V(\vartheta_{ij})$ is, to a very good approximation, a cosine function.

Eq. (5.12) shows that, if $V(\vartheta_{ij})$ is harmonic, L_{ij}, and therefore the array conductance G, are independent of frustration. Therefore, frustration effects will result from anharmonic corrections to $V(\vartheta_{ij})$. In order to simplify the treatment and to perform calculations analytically, we will restrict ourself to the first anharmonic term:

$$V_{AH}(\vartheta_{ij}) = \frac{E_J}{2}\vartheta_{ij}^2 - \frac{K}{24}\vartheta_{ij}^4, \tag{5.13}$$

where K is a positive constant. Moreover, we will replace the phase difference ϑ_{ij} by the variable $\phi_{ij} = (\varphi_i - \varphi_j - 2\pi n_{ij})$ where n_{ij} is an integer, ensuring the 2π-periodicity

of the potential. The validity of this substitution [47] was shown rigorously [48] for the Sierpinski gasket. Using Eq. (5.13), the inductance of a single junction becomes:

$$L_{ij} = \left(\frac{\hbar}{2e}\right)^2 \left[E_J - \frac{K}{2}\,\vartheta_{ij}^2\right]^{-1} \approx \left(\frac{\hbar}{2e}\right)^2 \frac{1}{E_J}\left[1 + \frac{K}{2E_J}\,\phi_{ij}^2\right]. \tag{5.14}$$

This relationship shows that the behavior of the inductance in a magnetic field is dictated by the anharmonic corrections through the factor $\gamma \equiv K/E_J$.

5.4.3 Calculation of the corrections to the inductance in the limit $f \to 0$

In the limit of weak frustrations, only the largest holes of the array will be occupied by vortices. This enables us to take into account the influence of the smaller loops, by considering the hierarchical structure of order N as a structure of order $N-1$ with renormalized coupling constants. It is possible to iteratively apply this process as long as the smallest loops of the successive decimated arrays are not occupied by vortices. In this section we calculate the renormalization factors and establish the corrections to the array inductance.

Since the phase differences are small for weak frustrations f, Eq. (5.14) indicates that the inductances of the various junctions are almost equal. This allows to calculate the corrections of the inductance of each junction δL_{ij} caused by frustration with a perturbation method. Let us write:

$$L_{ij} \approx L_J + \delta L_{ij} \quad \text{with} \quad \delta L_{ij} = \frac{K}{2E_J^2}\,\phi_{ij}^2, \tag{5.15}$$

where L_J represents the inductance of the junction at $f = 0$. The perturbation calculation is carried out in two steps. First, we consider the structure of Fig. 5.5(a) and take into account an harmonic interaction potential between the sites. The unperturbed Hamiltonian of this system H_{AR} is given by:

$$H_{AR} = \frac{E_J}{2}\left[(\varphi_1 - \varphi_3)^2 + 2(\varphi_3 - \varphi_4)^2 + (\varphi_4 - \varphi_2)^2\right]. \tag{5.16}$$

One can next use this Hamiltonian to determine the values of φ_3 and φ_4 for fixed values of φ_1 and φ_2, by minimizing the energy. This leads to:

$$\varphi_3 = \frac{3\varphi_1 + 2\varphi_2}{5} \quad \text{and} \quad \varphi_4 = \frac{2\varphi_1 + 3\varphi_2}{5}. \tag{5.17}$$

By substituting Eq. (5.17) into Eq. (5.16) and by introducing a renormalized coupling constant, the harmonic Hamiltonian of the hierarchical model of order 1 can be written:

$$H_{AR} = \frac{E_J}{2}\frac{2}{5}(\varphi_1 - \varphi_2)^2 \equiv \frac{E_{JR}^a}{2}(\varphi_1 - \varphi_2)^2 \quad \text{with} \quad E_{JR}^a = \frac{2}{5}E_J, \tag{5.18}$$

which is identical to the one of a hierarchical model of order 0 with a coupling energy renormalized by a factor 2/5. In a more general way, this decimation procedure applies to a hierarchical structure of order N and transforms it into the structure of order $N-1$ with a renormalized coupling energy.

One can then perform the second step of the perturbation calculation, where frustration phenomena are taken into account by adding the anharmonic corrections to the coupling potential. For a hierarchical structure of order 1 the previous Hamiltonian becomes:

$$H_{AH} = \frac{E_{JR}^a}{2}(\varphi_1 - \varphi_2)^2 - \frac{K}{24}\left[(\varphi_1 - \varphi_3)^4 + 2(\varphi_3 - \varphi_4)^4 + (\varphi_4 - \varphi_2)^4\right]. \tag{5.19}$$

The minimization of this Hamiltonian, keeping φ_1 and φ_2 fixed, leads to non-linear equations which can only be solved with a perturbation method, by expanding the phases φ_i $(i = 3, 4)$ about their harmonic solutions given by Eq. (5.17). The most important contributions are of first order in K and result from the substitution of the harmonic solutions of φ_i $(i = 3, 4)$ in the anharmonic contribution of Eq. (5.19). Proceeding in this way (substitution of Eq. (5.17) into Eq. (5.19)), one finds that the anharmonic Hamiltonian becomes:

$$H_{AH} = \frac{E_{JR}^a}{2}(\varphi_1 - \varphi_2)^2 - \frac{K}{24}\frac{34}{625}(\varphi_1 - \varphi_2)^4. \tag{5.20}$$

Similar to the harmonic case, this Hamiltonian is thus the Hamiltonian of a hierarchical structure of order 0 with renormalized coupling constants:

$$E_J \to E_{JR}^a = \frac{2}{5}E_J \quad \text{and} \quad K \to K_R = \frac{34}{625}K. \tag{5.21}$$

A comparison of the two expressions appearing in Eq. (5.21) reveals that for each decimation step the amplitude of the anharmonic corrections K decreases faster than the one of the harmonic terms E_J, therefore justifying *a posteriori* the perturbation approach. It is now possible to end this perturbation calculation by combining the results of Eq. (5.21) with the interpretation of Eq. (5.14) indicating that at each decimation step the corrections to the single inductances L_{ij} are given by a renormalization factor $\gamma \equiv K/E_J$. Finally, this allows to find the renormalization factor for the inductances appearing at each decimation step:

$$\gamma(N-1) = \frac{17}{125}\gamma(N). \tag{5.22}$$

In the experimental part we will be interested in the asymptotic behavior of the relative variation of the sheet impedance of the whole array $\Delta L_\square / L_\square(0)$, defined by:

$$\frac{\Delta L_\square(f)}{L_\square(0)} \equiv \frac{L_\square(f) - L_\square(0)}{L_\square(0)}. \tag{5.23}$$

The behavior of this quantity is completely determined by the renormalization of the single links L_{ij}, which will all be renormalized by the same common factor 17/125 at each

decimation step. When changing from a hierarchical structure of order N to a structure of order $N-1$, the relative variation of the total inductance of the array will therefore be reduced by the same factor 17/125, leading directly to:

$$\frac{\Delta L_{\square}(f/4^{\nu})}{L_{\square}(0)} \propto \frac{17}{125}\frac{\Delta L_{\square}(f)}{L_{\square}(0)}. \tag{5.24}$$

The effective change in frustration f from f to $f/4^{\nu}$ in Eq. (5.24) can be understood with Eq. (5.8). This equation indicates that the variation of the effective linear length $l(N)$ (see Fig. 5.5) of the hierarchical structure behaves according to $l(N) = 2^{-\nu}l(N-1)$ at each iteration step, with $\nu = 4/3$ for two-dimensional percolation. Since the frustration is defined in terms of a surface, i.e. $f(N) \propto l(N)^{-2}$, one obtains that the frustration increases at each decimation by a factor 4^{ν}, as indicated in Eq. (5.24). Notice at last that the asymptotic behavior $f \to 0$ of $\Delta L_{\square}/L_{\square}(0)$ described in Eq. (5.24) can be expressed equivalently as a power-law, to allow a more direct comparison with the experimental results:

$$\frac{\Delta L_{\square}(f)}{L_{\square}(0)} \propto f^{\alpha} \quad \text{where} \quad \alpha = \frac{\ln(125/17)}{\nu \ln 4} \simeq 1.08. \tag{5.25}$$

The power-law behavior of $\Delta L_{\square}/L_{\square}(0)$ described by Eq. (5.25) or, equivalently, by Eq. (5.24) follows therefore from the scale invariance peculiar to the geometry of the disordered array. A comparison of this predicted behavior with experimental results will be performed in section 5.4.4, and will allow to confirm the self-similar properties of the studied array.

It's interesting to estimate the number of iteration steps N necessary to obtain a regular array with renormalized coupling constants from a percolative structure. This can be achieved by comparing the correlation length ξ_p with the characteristic length $l(N)$ of the hierarchical structure given by $l(N) = 2^{-\nu}l(N-1)$. For the percolation fraction $p = 0.515$, they have comparable sizes after $N = 4-5$ steps, indicating that we need $4-5$ decimation steps to reduce our percolative array to a regular one with renormalized coupling constants.

5.4.4 Self-similar signature of the array

In this section we will show the measurements performed as a function of weak magnetic fields in a temperature region where the vortices are pinned in the potential provided by the array. We will be more particularly interested in the behavior of the relative change of the inverse sheet inductance $\Delta L_{\square}^{-1}(f)/L_{\square}^{-1}(0)$ defined by:

$$\frac{\Delta L_{\square}^{-1}(f)}{L_{\square}^{-1}(0)} \equiv \frac{L_{\square}^{-1}(0) - L_{\square}^{-1}(f)}{L_{\square}^{-1}(0)} \propto f^{\alpha} \quad \text{with} \quad \alpha \approx 1.08 \quad \text{for} \quad f \to 0. \tag{5.26}$$

In the limit of weak frustrations, the behavior of this quantity is equivalent to that of the relative change of the sheet inductance $\Delta L_{\square}(f)/L_{\square}(0)$ defined through Eq. (5.23). The behavior of $\Delta L_{\square}^{-1}(f)/L_{\square}^{-1}(0)$ obeys therefore Eq. (5.25) and corresponds to a power-law with an exponent $\alpha \approx 1.08$ in the limit $f \to 0$.

To check the power law behavior predicted by theory, the relative change of the inverse sheet inductance is reported on logarithmic scales in Fig. 5.6. These measurements were performed with a driving frequency of 163 Hz at two different reduced temperatures τ over a frustration range of approximately two decades.

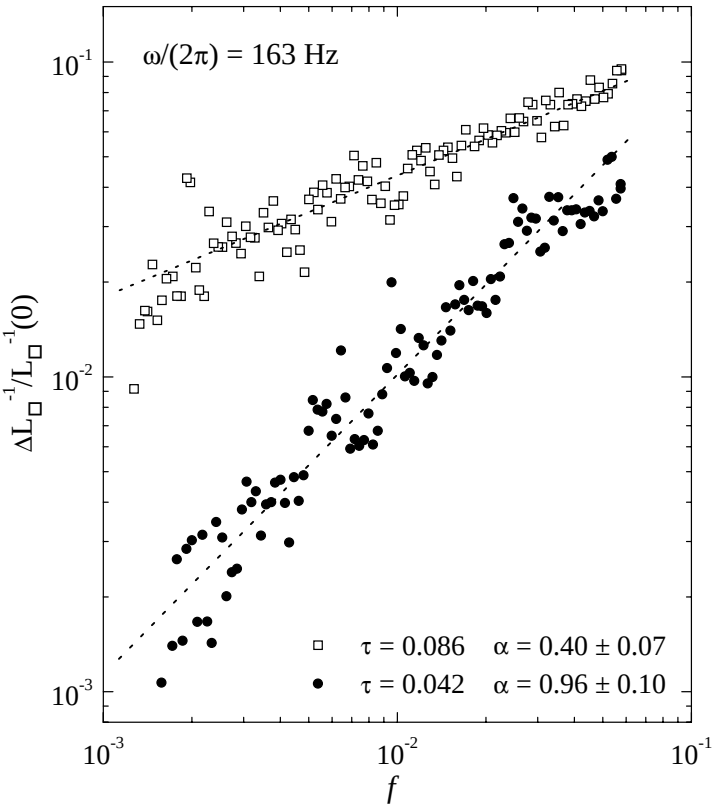

Figure 5.6: Logarithmic representation of the relative change of the inverse sheet inductance at a frequency of 163 Hz as a function of frustration. The measurements were performed at different reduced temperatures and both behave as power-laws. A decrease of the reduced temperature corresponds to an increase of the measured exponent which approaches the value $\alpha = 1.08$ predicted by theory. The dashed lines are the fits used to extract the exponents. The uncertainties related to the exponents take only into account the data scattering.

The sensitivity threshold of our measurement setup restricts the reduced temperature to a lower value $\tau \simeq 0.04$ for this kind of measurement performed in a magnetic field at a frequency of 163 Hz. One curve of Fig. 5.6 was recorded at the lower temperature $\tau = 0.042$, slightly below the critical temperature $\tau_c = 0.055$, while the other was taken at a higher temperature. As discussed in section 5.4.1, the theoretical approach leading to a power-law behavior of $\Delta L_\square^{-1}(f)/L_\square^{-1}(0)$ presupposes in particular that the field induced vortices behave as static quantities completely pinned by the potential of the array of junctions. To check that this condition is fulfilled for both measurements of Fig. 5.6, we

can refer to the measurements and to the discussion of section 5.6.6. These indicate that the thermal activation of vortices appears at reduced temperatures higher than $\tau \approx 0.2$ at a frequency of 163 Hz and weak frustrations. Since the data shown in Fig. 5.6 were recorded at lower temperatures, they correspond to a regime where vortices can be treated as static objects, and they can be compared to the theoretical approach of section 5.4.3. The theoretical description also assumes that only field induced vortices are present in the system. This condition is not completely fulfilled for both curves of Fig. 5.6, because they were measured near the critical temperature, where thermally nucleated vortices are present in the array.

The domain of frustration shown in Fig. 5.6 is limited by the domain of validity of the theoretical approach of section 5.4.2 which presupposes that the sample is in the fractal domain, at frustrations larger than 1 vortex per loop of area ξ_p^2. Numerically, this condition corresponds to frustrations larger than $f \simeq 1$ ‰. The upper limit of frustration $f \simeq 0.1$ is fixed on the one hand by the perturbation approach used to calculate Eq. (5.25), which is only correct at small frustration, and on the other hand by the decimation process which is only valid if the smallest loops of junctions are free from vortices.

The measurements shown in Fig. 5.6 present both a power-law behavior, but with a strongly temperature dependent exponent α. A decrease of the temperature therefore corresponds to an increase of the measured exponent, which reaches at $\tau = 0.042$ the value $\alpha = 0.96$, near 1.08 predicted by theory. For the measurement performed at the lower temperature, the asymptotic corrections $\Delta L_\square^{-1}(f)/L_\square^{-1}(0)$ are therefore in good agreement with the theoretical predictions. This power-law behavior thus confirms experimentally that the disordered structure of the array possesses effectively a scale invariant fractal structure at scales smaller than ξ_p.

The temperature dependence of the exponent α is probably due to thermal fluctuations, which have not been taken into account in the theoretical approach, but which seem to have a considerable effect on the measured curves. This strong dependence may be qualitatively explained by remembering that the vortices interact very weakly at the lowest frustrations. The states appearing at low frustrations require therefore a long range phase coherence, which is easily modified by thermal fluctuations. Since the latter are important in the critical region, it seems reasonable that they are still present in the measurements shown in Fig. 5.6.

A deterministic fractal system is built by applying an iterative rule to a unit cell, as shown, for example, in Fig. 5.3 for the case of the hierarchical links and blobs model. They possess consequently a regular sublattice with loops of determined positions and sizes. On the other hand, the percolative structure of our array is completely disordered because it was built using a random process, and possesses loops of all sizes, randomly distributed. These differences of construction can be related to the data shown in Fig. 5.6 by comparing similar measurements performed on deterministic fractals [22], which showed that the power-law describing the corrections to the inductance is modulated by a fine regular structure. These fine structures can be attributed to the regular sublattice of the deterministic fractal. The measurements shown in Fig. 5.6 show no regular fine structures; this therefore indicates that our percolating array is really completely disordered.

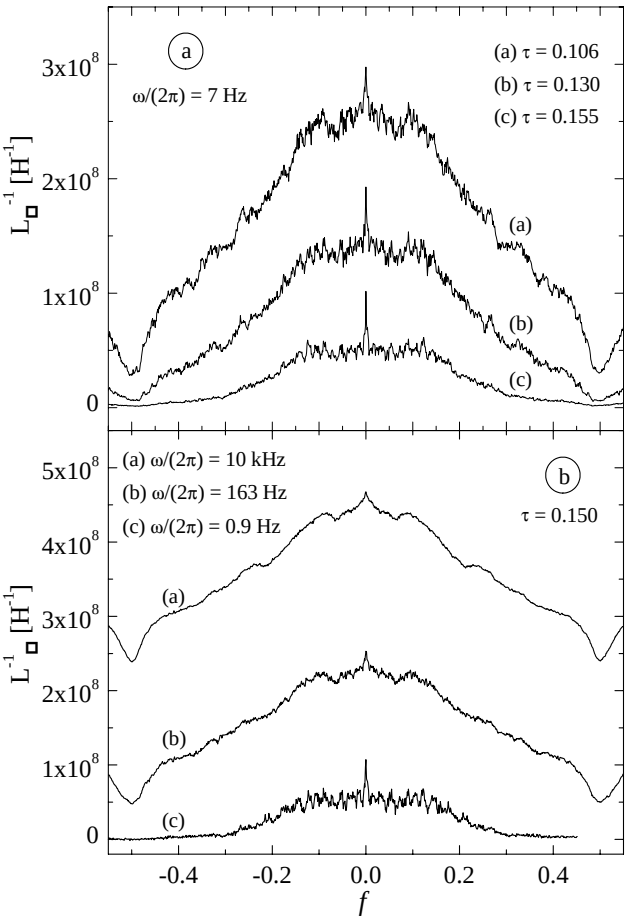

Figure 5.7: (a) Inverse sheet inductance measured at 7 Hz as a function of frustration for several reduced temperatures. (b) Inverse sheet inductance measured as a function of frustration for several frequencies at $\tau = 0.150$. Notice that the curves show qualitatively the same behavior in (a) and (b) with varying of temperature and frequency.

It is possible to grasp the influence of thermal fluctuations on the measurements in the critical region from the data shown in Fig. 5.7. The inverse sheet inductance measured at 7 Hz for several temperatures as a function of frustration is plotted in Fig. 5.7 (a). Similar curves measured at $\tau = 0.150$ for several frequencies are shown in Fig. 5.7 (b). The effects of thermal fluctuations are clearly visible in Fig. 5.7 (a): an increase of the temperature leads to a decreasing $L_{\square}^{-1}$. Moreover, for $|f| \leq 0.2$, one notices that the curves exhibit sharp peaks, which are probably due to commensurability effects. Despite the disordered structure of the array, the vortices seem therefore to adopt privileged configurations, resulting in the small peaks of $L_{\square}^{-1}$ observed for $|f| \leq 0.2$. A comparison of the curves shown in Figs. 5.7 (a) and 5.7 (b) shows that they behave similarly as a function of temperature or frequency. For a fixed temperature, the effects of thermal fluctuations are therefore more pronounced at low frequencies.

5.5 Response near the critical temperature

The basic issue addressed in this section is the following: does a Beresinskii-Kosterlitz-Thouless (BKT) transition [7, 8] occur in disordered arrays? And if yes, under which conditions? The low-temperature conductance measurements discussed in section 5.3 show that, at sufficiently low frequencies such that the frequency-dependent length scale at which one is probing the system is larger than ξ_p, percolative arrays behave as two-dimensional homogeneous systems. One can therefore speculate that, at sufficiently low frequencies, an array with percolative disorder undergoes the BKT transition characteristic of two-dimensional superfluids.

In this section we first introduce the notions relative to the BKT transition in a very general way, then we focus more specifically on the response of the bound vortex pairs. These theoretical predictions will be compared to our measurements of the sheet conductance.

5.5.1 Scenario of the BKT transition

Our discussion of the BKT transition will not be an attempt to provide a complete rigorous derivation, but rather to develop a coherent picture of the underlying physics. Consider first an array in zero magnetic field within the context of the XY model. At zero temperature all the spins are aligned and the system exhibits a long-range order. At non-zero temperature, fluctuations in the form of spin-waves appear and destroy the conventional long-range order in 2D. There remains nevertheless a certain order, called topological order, characterized by a spin-spin correlation function which decreases algebraically with the distance x, i.e. proportional to $x^{-\eta}$, where $\eta = \tau/(2\pi)$ [51]. At high temperatures, the system is found to be in a liquid like phase described by an exponentially decaying correlation function. One thus expects some kind of phase transition between these two states. This was explained by Beresinskii, Kosterlitz and Thouless [7, 8, 52] by introducing a new type of excitations of the spins: the vortex-antivortex bound pairs and the single vortices.

In a regular structure the energy $E_v = \pi E_J \ln(L/a)$ of a single vortex [14] involves all the spins of the system and increases logarithmically with the sample size L. On the other hand, the cost in energy of bound pairs also increases logarithmically, but only with the distance r between the two constituents: $E_p = 2\pi E_J \ln(r/a)$. At low temperature the nucleation of vortices is therefore prohibitively expensive, therefore the bound pairs appear first as the transition temperature is approached from below. Some small pairs will first be created. As the temperature is raised, more and more pairs of increasing sizes will be present in the system. The BKT transition temperature T_c is defined as the temperature at which the largest pair (ideally of infinite size) unbinds, i.e. when the first free vortex appears. This phenomenon leads to a destruction of the topological order, which is replaced by a short range order, as in a liquid. The system is then characterized by an exponentially decaying spin correlation function with a correlation length ξ_+ specific

to the BKT transition, which is given in a narrow interval above T_c by [52]:

$$\xi_+/a \sim \exp(\frac{b}{\sqrt{T-T_c}}), \tag{5.27}$$

where b is a constant of order unity. Physically ξ_+ represents the scale at which vortices begin to unbind, or, in other words, the mean distance between two free vortices. At smaller scales vortices are still bound in pairs, even if the temperature is above the critical temperature T_c.

Another important aspect of the BKT theory involves the screening of the vortex-antivortex interaction due to the background of polarizable small vortex pairs located between pairs of larger sizes. Because vortex pairs are thermal excitations of the system, there will be only a few pairs present well below T_c. For $T \ll T_c$, we therefore expect that the space between a given pair will not contain other pairs, and that a simple unrenormalized interaction is correct. On the other hand, near the transition temperature, there are many more vortex pairs present in the system, including some which are located between and around the constituent vortices of other, larger, pairs. Since vortices of opposite polarity attract, these smaller pairs will tend to align in the field produced by the larger pairs. This polarization will then reduce the strength of the vortex interaction. This effect is generally described by incorporating the effects of the smallest bound pairs into a scale dependent dielectric function $\epsilon_r(r,T)$, which reduces the interaction energy of the pairs of larger sizes. The calculation of $\epsilon_r(r,T)$ involves the application of renormalization group technique to the BKT model, and leads to the BKT renormalizations equations [52].

At the critical temperature T_c these equations predict, for infinite systems, a drop to zero in the superfluid density according to a universal relation between the superfluid density, which in our case is inversely proportional to the inductance of the array, and the critical temperature itself. For a regular triangular array it is given by:

$$L_\square(T_c)T_c = \frac{\sqrt{3}}{2}\frac{\phi_0^2}{8\pi k_B} \approx 1.07 \cdot 10^{-8} \text{ HK}. \tag{5.28}$$

5.5.2 Vortex contribution to the array response

Quite generally, the response of the array to an external electromagnetic excitation can be characterized by taking into account the contributions of the superfluid, of the normal electrons and of the vortices. This can be achieved by using a two-fluid model, where the medium is described by an inductive superfluid channel in parallel with a dissipative channel.

The effects due to the vortices can be incorporated in the conductance of the array as follows [60, 61]: in the presence of a current, the vortices experience a Lorentz force which will set them in motion perpendicularly to the current flow. Associated with the vortex motion, there is an electric field which adds to the electric field of the accelerated superfluid background. This phenomenon therefore leads [62] to an increase in the sheet impedance by an amount $Z_v(\omega,\tau)$, which comes in series [47] with the impedance of the superfluid background $Z_0(\omega,\tau) \equiv i\omega L_0(\tau)$, as shown schematically in Fig. 5.8.

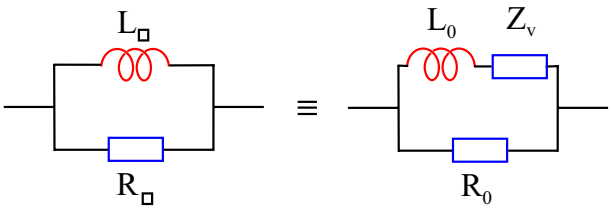

Figure 5.8: Equivalent circuit for a 2D superconductor in the presence of vortices. The vortex response renormalizes the superfluid channel by adding an impedance Z_v. $R_0(\tau)$ represents the dissipative processes resulting from the normal currents flowing in the junctions.

The measured quantity is the sheet conductance $G(\omega,\tau) \equiv (R_\square)^{-1} + (i\omega L_\square)^{-1}$. It is related to the vortex impedance $Z_v(\omega,\tau) = R_v + i\omega L_v$ as indicated in Fig. 5.8, and the components R_v and L_v are therefore:

$$R_v(\omega,\tau) = \frac{R_\square^{-1} - R_0^{-1}}{\left(R_\square^{-1} - R_0^{-1}\right)^2 + (\omega L_\square)^{-2}} \quad \text{and} \tag{5.29}$$

$$L_v(\omega,\tau) = \frac{L_\square}{1 + \left(R_\square^{-1} - R_0^{-1}\right)^2 (\omega L_\square)^2} - L_0 \equiv L_* - L_0 \ . \tag{5.30}$$

When analyzing the data, we will therefore extract R_v and L_v from the sheet conductance G to determine the vortex dynamics. The usual way to calculate R_v and L_v is to introduce the dielectric function of the vortex medium $\epsilon(\omega,\tau)$, or equivalently the susceptibility of the vortex medium $\chi(\omega,\tau) \equiv \chi' - i\chi''$, with $\epsilon(\omega,\tau) = 1 + 4\pi\chi(\omega,\tau)$, by setting $i\omega L_0 + Z_v = i\omega L_0 \epsilon(\omega,\tau)$, leading to:

$$R_v(\omega,\tau) = 4\pi L_0(\tau)\omega\chi''(\omega,\tau) \quad \text{and} \tag{5.31}$$

$$L_v(\omega,\tau) = L_0(\tau) 4\pi\chi'(\omega,\tau). \tag{5.32}$$

5.5.3 Calculation of the bound pair dielectric function

To calculate $\chi(\omega,\tau)$, in this subsection, we restrict ourself to the response of vortex-antivortex bound pairs [63, 64, 47, 67]. In discussing the experimental results, the theoretical predictions derived here will be valid below τ_c, where the response is dominated exclusively by bound vortices, and also above τ_c provided the length scales probed in our conductance measurements are small enough to neglect the influence of single vortices. By using the 2D Coulomb gas analogy, Ambegaokar et al. [63] and Kadin et al. [64] write the scale dependent susceptibility as:

$$\chi(\omega,T) = 2\pi \int_{a_c}^{\infty} n_p(r)\alpha(r,\omega) r dr \tag{5.33}$$

$$\text{where} \quad n_p(r) = \frac{1}{a_c^4} e^{-\frac{U_p(r)}{k_B T}} \quad \text{and} \quad \alpha(r,\omega) = \frac{q_0^2 r^2}{4 k_B T} \frac{1}{1 + i\frac{\omega r^2}{\gamma D_v}}. \tag{5.34}$$

$n_p(r)$ is the density of thermally excited vortex-antivortex pairs, $\alpha(r,\omega)$ is the pair polarizability, γ a numerical factor approximately equal to 14 for a regular system [65], and a_c is a cut-off length to be specified later. The vortex charge q_0 can be written in terms of the renormalized coupling energy and the vortex diffusion constant is related to the vortex mobility μ_v by Einstein's relation $D_v = \mu_v k_B T$. The pair energy (vortex-antivortex energy) is given by:

$$U_p(r) = 2E_N + \int_{a_c}^{r} q^2(r') d[\ln r'] \approx 2E_N + 2\pi E_{JR} \ln \frac{r}{a_c} \tag{5.35}$$

where E_N is the nucleation energy for a vortex (or antivortex) and $q^2(r)$ is the screened vortex charge. The second part of Eq. (5.35) was established by neglecting screening, i.e. by setting $q(r) = q_0$, and using $q_0^2 = 2\pi E_{JR}$, with $E_{JR} \sim E_J(p - p_c)^\mu$. Recalling the Kosterlitz-Thouless prediction $k_B T_c \approx \pi/2 E_{JR}(T_c)$ and using Eq. (5.35), $n_p(r)$ becomes:

$$n_p(r) = \frac{1}{a_c^4} e^{-\frac{2E_N}{k_B T}} \left(\frac{r}{a_c}\right)^{-4\frac{\tau_c}{\tau}}. \tag{5.36}$$

Noticing that the term $q_0^2 r^2/(4k_B T) = \tau_c r^2/\tau$ in Eq. (5.34), we find that $\chi(\omega,\tau)$ is given by (with $x \equiv r/a_c$):

$$\chi(\omega,\tau) = 2\pi \frac{\tau_c}{\tau} \int_1^\infty e^{-\frac{2E_N}{k_B T}} x^{3-4\frac{\tau_c}{\tau}} g(x,\omega) dx \quad \text{where} \quad g(x,\omega) = \left(1 + i\frac{\omega a_c^2}{\gamma D_v} x^2\right)^{-1}. \tag{5.37}$$

Before proceeding further, let us make three important comments:

- the above approach is correct only when used to describe the behavior of a two-dimensional system in an Euclidean geometry. This clearly emerges from the logarithmic interaction between charges in two dimensions (see Eq. (5.35)). With regards to percolative arrays, it's therefore evident that our approach is valid only at length scales r such that $r \geq \xi_p$, leading to $a_c = \xi_p$;

- for fractal structures, the nucleation energy E_N depends on the size R_t of the loop in which the vortex is created, approximately as $E_N \approx E_J(a/R_t)^\zeta$ [50, 22], with $\zeta = \mu/\nu$ in two dimensions. It follows that the vortex-antivortex pairs which are mostly contributing to $\chi(\omega,\tau)$ are those located in the largest loops, i.e. those of size $R_t \approx \xi_p$;

- this derivation implicitly assumes a rather low density of vortices, in particular that there is no pair-pair interaction. This is evident, for example in Eqs. (5.34) and (5.35), where the unrenormalized effective charge is used to determine the polarizability and the pair energy.

Relying on these remarks and using once again the BKT prediction, it's now possible to write:

$$\chi(\omega,\tau) = 2\pi\frac{\tau_c}{\tau}e^{-s\frac{\tau_c}{\tau}}\int_1^\infty x^{3-4\frac{\tau_c}{\tau}}g(x,\omega)dx \tag{5.38}$$

where s is a numerical factor of order unity. The last step to estimate $\chi(\omega,\tau)$ is to find an approximation for $g(x,\omega)$ to calculate the integral in Eq. (5.38). This can be achieved in the following way [63]: first, setting $x_\omega \equiv r_\omega/\xi_p = (\gamma D_v/\omega\xi_p^2)^{1/2}$, we can approximate $g(x,\omega)$ by:

$$g(x,\omega) = \Theta[1-\frac{x}{x_\omega}] - i\frac{\pi}{4}x\delta(x-x_\omega) \tag{5.39}$$

where $\Theta[1-\frac{x}{x_\omega}] = 1$ for $x < x_\omega$ and $= 0$ for $x > x_\omega$. By substituting Eq. (5.39) into Eq. (5.38) one obtains the final expressions for the susceptibility of the vortex medium:

$$\chi'(\omega,\tau) = \frac{\pi(\tau_c/\tau)e^{-s\tau_c/\tau}}{2[(\tau_c/\tau)-1]}\left\{1-(\omega\tau_{Dp})^{2[(\tau_c/\tau)-1]}\right\} \quad \text{for } \tau \neq \tau_c \tag{5.40}$$

$$\chi'(\omega,\tau) = \pi e^{-s}\ln\left(\frac{1}{\omega\tau_{Dp}}\right) \quad \text{for } \tau = \tau_c \tag{5.41}$$

$$\chi''(\omega,\tau) = \frac{\pi^2}{2}\frac{\tau_c}{\tau}e^{-s(\tau_c/\tau)}(\omega\tau_{Dp})^{2[(\tau_c/\tau)-1]} \tag{5.42}$$

where $\tau_{Dp} = \xi_p^2/(\gamma D_v)$. By setting $u(\tau) = 2\tau_c/\tau - 1$, one obtains the relations for the components of the vortex impedance in the relevant limit for the 2D case ($\omega\tau_{Dp} < 1$):

$$R_v(\omega,\tau) = 2\pi^3\frac{\tau_c}{\tau}e^{-s(\tau_c/\tau)}\frac{L_0(\tau)}{\tau_{Dp}}(\omega\tau_{Dp})^{u(\tau)} \tag{5.43}$$

$$\lim_{\omega\tau_{Dp}\mapsto 0}(L_0+L_v) = L_0(\tau)\left[1+\frac{4\pi^2(\tau_c/\tau)e^{-s\tau_c/\tau}}{u(\tau)-1}\right] \quad \text{for } \tau < \tau_c \tag{5.44}$$

$$\lim_{\omega\tau_{Dp}\mapsto 0}(L_0+L_v) = L_0(\tau)\frac{4\pi^2(\tau_c/\tau)e^{-s\tau_c/\tau}}{1-u(\tau)}\frac{1}{(\omega\tau_{Dp})^{1-u(\tau)}} \quad \text{for } \tau > \tau_c \tag{5.45}$$

$$\lim_{\omega\tau_{Dp}\mapsto 0}(L_0+L_v) = L_0(\tau_c)4\pi^2e^{-s}\ln\left(\frac{1}{\omega\tau_{Dp}}\right) \quad \text{for } \tau = \tau_c. \tag{5.46}$$

It's useful to briefly discuss the behavior of these formulas in three temperatures limits ($\tau \ll \tau_c, \tau \gg \tau_c, \text{and}\, \tau = \tau_c$). Notice first that Eq. (5.43) predicts an exponential decrease

of R_v with decreasing temperature, as expected. Moreover, one observes that R_v decreases faster ($u(\tau) > 1$) for $\tau < \tau_c$ with decreasing frequency than for $\tau > \tau_c$ ($u(\tau) < 1$).

In the relevant low frequency limit ($\omega\tau_{Dp} < 1$), the inductive part approaches a constant for temperatures below τ_c as shown by Eq. (5.44), thereby indicating a non-vanishing superfluid density. In particular, for $\tau \ll \tau_c$, the vortex induced component becomes negligible, as expected, since there are no thermally excited vortex-antivortex pairs. For temperatures above τ_c, $(L_0 + L_v) \mapsto \infty$ for $\omega \mapsto 0$, pointing to a vanishing superfluid density at high temperature, as shown by Eq. (5.45). Finally, Eq. (5.46) indicates that the inductive part diverges logarithmically at the transition temperature.

5.5.4 Sheet conductance measurements in the vicinity of T_c

The set of curves presented in this section was measured for different temperatures, by sweeping the frequency from 0.1 Hz to 20 kHz. In this way, it's possible to study, at a given temperature, different dynamical regimes. This acquisition method proved to be very fruitful, because it allows to identify the nature of excitations which dominate the response at given frequency and temperature.

Although the behavior of the sheet conductance is not directly interpretable in terms of vortex dynamics, as explained in section 5.5.2, it's beneficial to take a global look at $G(T, \omega)$ to infer a qualitative understanding of the dynamical phenomena occurring in the array. The resistive part $R_\square(\omega, \tau)$ and the inductive part $L_\square^{-1}(\omega, \tau)$ of $G(\omega, \tau)$ as a function of ω are shown in Figs. 5.9 and 5.10 at several reduced temperatures.

For frequencies larger than $\omega_c \simeq 1$ kHz, the resistive and the inductive part of $G(\omega, \tau)$ tend towards a power-law frequency dependence with an exponent close to 1/2 at all temperatures. A similar behavior was found in percolative arrays at temperatures well below τ_c (see section 5.3). Thus we attribute the power-law frequency dependence to the same physical mechanism: at high frequencies, in the fractal regime, the response is dominated by localized "spin-wave" excitations. As the frequency decreases below ω_c, the data of Fig. 5.9 (a) exhibit, at intermediate frequencies and at sufficiently low temperatures ($\tau < 0.122$), a ω-independent behavior. In this regime, the relevant excitations are extended "spin-waves" characteristic of the two dimensional Euclidean regime.

As evidenced in Fig. 5.9 (a), the sheet resistance behaves like a power-law with an exponent close to 1 at low frequencies and for $\tau < 0.122$. As it will be shown in details below, this behavior can be ascribed to the response of vortex-antivortex bound pairs. At τ_c, the largest bound pairs (ideally of infinite size) break up into single vortices and then, as the temperature is increased, smaller and smaller pairs dissociate. This phenomenon is visible in Fig. 5.9 (b) where, with decreasing frequency, $R_\square(\omega, \tau)$ crosses from the bound pair power-law dominated regime to a frequency independent value pointing to single vortex dynamics (see later section 5.6). The frequency at which the crossover appears increases with increasing temperature, thereby showing the dissociation of bound pairs of smaller and smaller size.

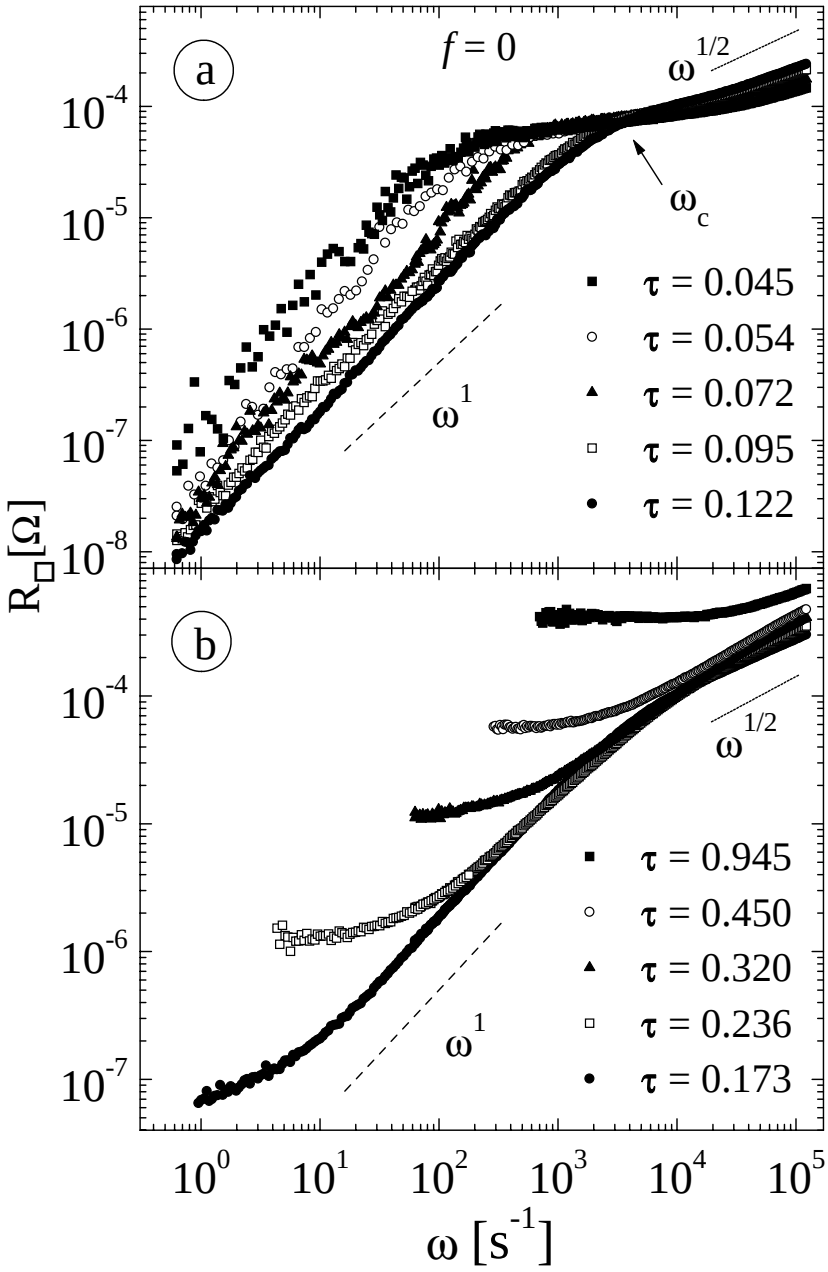

Figure 5.9: Sheet resistance of the array vs frequency at reduced temperatures larger than or approximately equal to the transition temperature $\tau_c = 0.055$. In (a), notice the power-law behavior occurring at low frequencies, denoting a regime due to bound pairs. In (b), the appearance of plateaus reveals a regime dominated by single vortices at the lowest frequencies.

The change in behaviour due to the dissociation of bound pairs into single vortices is also visible in the $L_{\square}^{-1}(\omega, \tau)$ isotherms of Fig. 5.10. The curves measured at reduced temperatures $\tau > 0.122$ show at low frequencies a power-law dependence close to ω^2. As

a matter of fact, this is in agreement with predictions of barrier limited diffusion (see section 5.6.4). With increasing frequency and decreasing temperature, $L_\square^{-1}(\omega,\tau)$ exhibits a crossover to a weaker and weaker ω-dependent regime, which can be associated with the dynamics of bound pairs, as described by Eqs. (5.44) and (5.45).

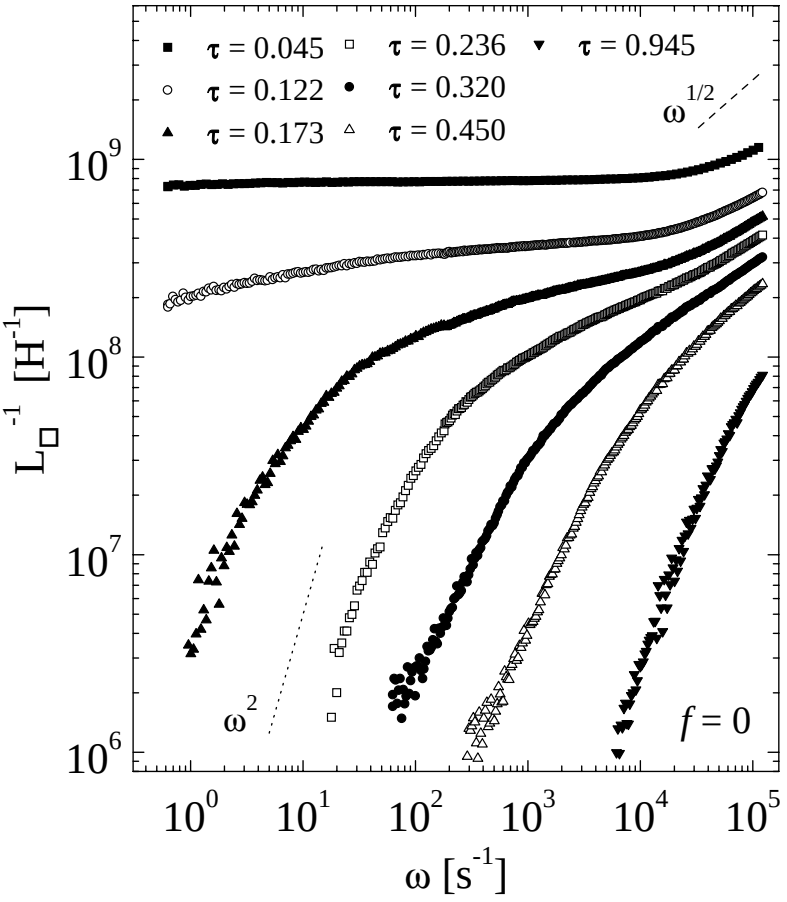

Figure 5.10: Inverse sheet inductance of the array as a function of frequency at several reduced temperatures higher or equal to the transition temperature. The dramatic fall of $L_\square^{-1}$ with decreasing frequency demonstrates the disappearance of the superfluid density at large scales at the higher temperatures.

Notice that the vortex dynamics takes place in a narrow frequency range for each isotherm, as observed in Figs. 5.9 and 5.10. The experimental window to probe the single vortex dynamics in zero magnetic field is therefore rather limited.

The interpretation of the data shown in Figs. 5.9 and 5.10 is confirmed experimentally by probing the response of the array at weak frustrations. In this way, it is possible to fix the field-induced vortex density independently of the measured temperature, and thus to vary the single vortex density while keeping the number of bound pairs constant. We show in Fig. 5.11 (a) the sheet resistance $R_\square(\omega,\tau,f)$ at several weak frustrations at a

reduced temperature $\tau = 0.173$. Similar measurements taken at several temperatures are plotted in Fig. 5.11 (b).

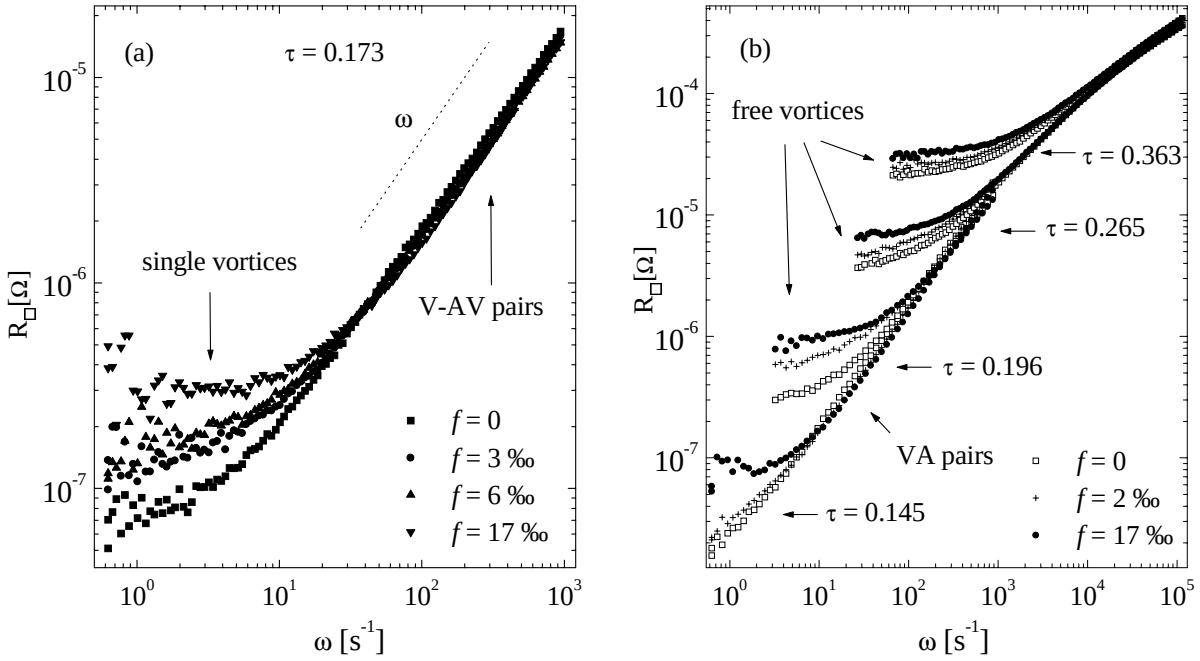

Figure 5.11: (a) Sheet resistance of the array at small frustrations for $\tau = 0.173$. Two kinds of behaviors as a function of length scale are clearly visible. The large scale response, at low frequencies, is dominated by single vortices while the bound pair regime is valid at small scales. (b) Sheet resistance of the array at small frustrations for several reduced temperatures. The general trend is similar for each set of data and strongly supports the scenario proposed for $f = 0$.

The general trend of the data shown in Fig. 5.11 (a) and (b) is the same: the curves meet with increasing frequency, independently of the applied magnetic field. This clearly reveals the appearance of two kinds of behavior as a function of length scale: at high frequencies the response is not influenced by the external field, and behaves as a power-law with frequency. By remembering that the observed scale increases with decreasing frequency (see section 3.2), this frustration independence demonstrates that single vortices play a negligible part at small scales. Bound vortex pairs dominate this regime. On the other hand, for the lowest frequencies, the sheet resistance saturates at various levels and is found to be strongly field dependent, pointing out the presence of unbound vortices at large scales. Moreover, notice that the cross-over frequency increases with increasing temperature, indicating that pairs of smaller sizes are broken with increasing temperature. The scenario proposed for $f = 0$ is therefore corroborated by the measurements shown in Fig. 5.11.

5.5.5 Extraction of the vortex impedance

In this section, we proceed in two stages to extract and discuss in detail the vortex impedance $Z_v(\omega,\tau) \equiv R_v + i\omega L_v$: we first explain how we extracted R_v and L_v from the sheet conductance $G(\omega,\tau)$, and then we discuss the data using the theoretical expressions derived in section 5.5.3.

At frequency and temperature values where bound pairs do not contribute to the response, according to Eq. (5.11), $R_\Box = R_0 \propto R_J(\tau)(p-p_c)^\mu$ and $L_\Box^{-1} = L_0^{-1} \propto L_J^{-1}(\tau)(p-p_c)^\mu$ in the Euclidean two-dimensional regime of interest here. Thus, $R_0(\tau)$ can be extracted from low-frequency " plateaus " as those shown in Fig. 5.4. The result of this analysis is displayed in Fig. 5.12. The data show that R_0 increases with temperature as one qualitatively expects from a progressive suppression of the proximity effect in the Cu-bridges linking the superconducting Pb-islands. At high temperatures $R_0(\tau)$ saturates to a value of $10^{-4}\,\Omega$ consistent with the prediction $R_0 = 4.5R_J[(p-p_c)/(1-p_c)]^\mu$ if R_J is set equal to its maximum value, i.e. $R_J = R_N = 5.2$ mΩ.

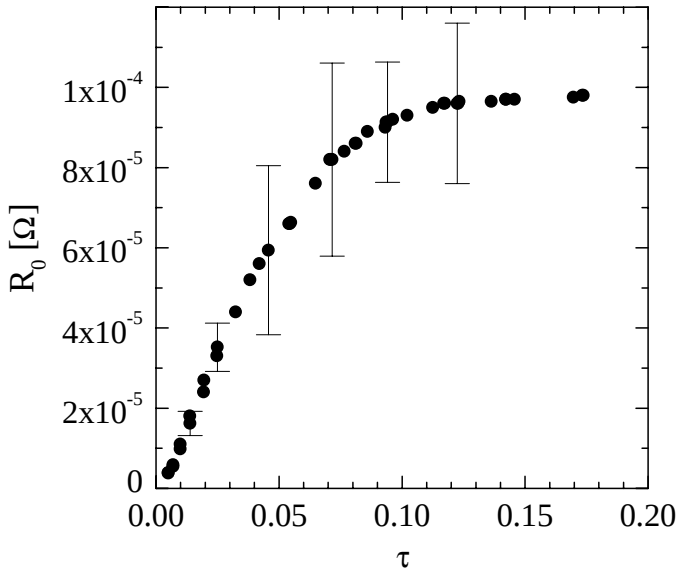

Figure 5.12: Sheet resistance of the array in the 2D spin-wave dominated regime as a function of the reduced temperature. The saturation of R_0 for $\tau \geq 0.13$ can be ascribed to the renormalization of the normal state resistance by disorder. Notice that the data corresponding to $\tau \geq 0.05$ show large uncertainties, as indicated by the error bars.

$R_v(\omega,\tau)$ was determined with Eq. (5.29), identifying $R_0(\tau)$ with the plateau of $R_\Box(\tau)$ shown in Fig. 5.12. The result is shown in Fig. 5.13 and gives the resistance due to the vortex excitations as a function of frequency at several reduced temperatures near τ_c. The lowest measurement frequency of 0.1 Hz was imposed by the sensitivity of our acquisition system and by the time available for each measurement, whereas the highest frequency, about 160 Hz, is the upper limit of the regime dominated by bound pairs as noticed in the

discussion of Fig. 5.9. The noise observed in the data taken at the lowest temperatures is intrinsic to our measurement system.

It is now possible to compare the behavior of $R_v(\omega, \tau)$ predicted by Eq. (5.43) with the experimental data shown in Fig. 5.13. At reduced temperatures $\tau \leq 0.122$, the general trend of the experimental data is well described by Eq. (5.43): the frequency dependence behaves like a power-law, $R_v \propto \omega^{u(\tau)}$, with a temperature dependent exponent close to 1. For the measurements performed at the higher reduced temperatures $\tau \geq 0.144$, a change appears in the vortex response with decreasing frequency: $R_v(\omega, \tau)$ changes from power-law behavior to a frequency independent regime. This cross-over occurs at higher and higher frequencies with increasing temperature, indicating a transition from the bound pair dominated response to the single vortex regime.

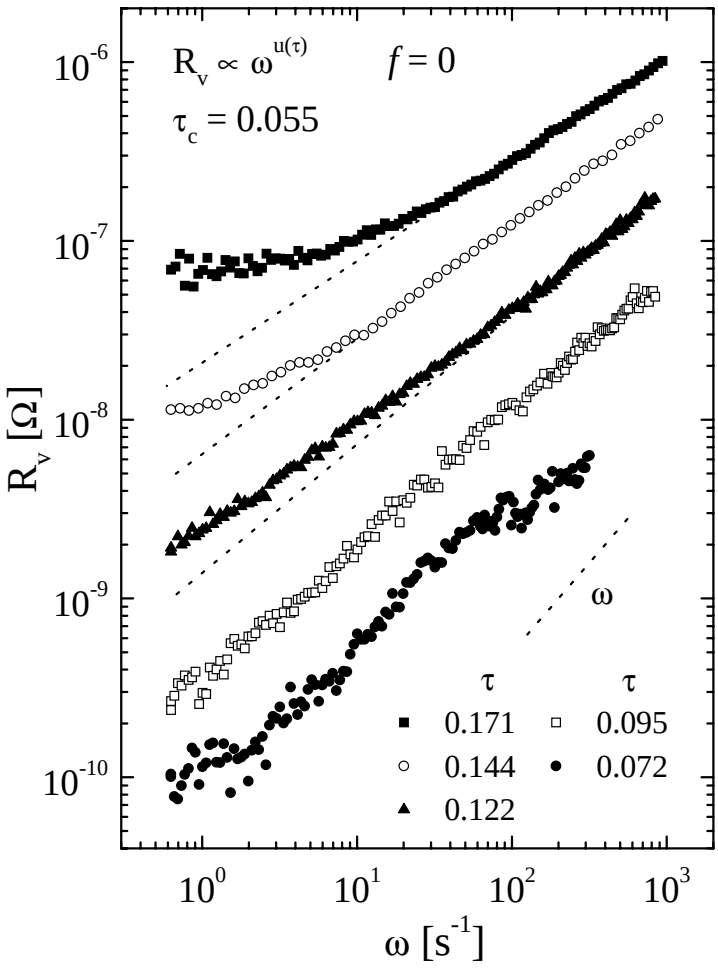

Figure 5.13: Resistance due to the vortex excitations as a function of frequency for temperatures above the transition. Notice the qualitative agreement with Eq. (5.43), which predicts a power-law behaviour of $R_v(\omega, \tau)$ in the vicinity of τ_c. The dashed lines correspond to the fits performed to extract the exponent $u(\tau)$.

The extraction of $L_v(\omega,\tau)$ is more complex, because it involves not only $R_0(\tau)$ but also $L_0(\tau)$, which adds in series to the vortex contribution, as expressed by Eq. (5.30). We used two different methods to determine L_v:

- the value of $L_0(\tau)$ may be calculated with Eq. (4.5) and then inserted into Eq. (5.30); the weak point of this method is that it relies on a fit performed using a theoretical expression (de Gennes formula) to determine the inductance of a single junction $L_J(\tau)$;

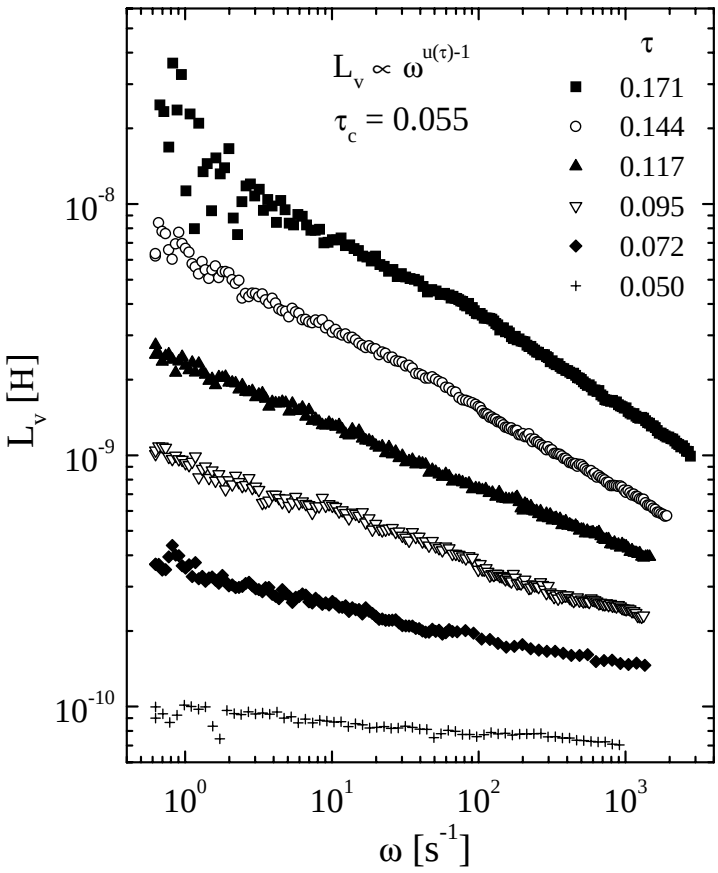

Figure 5.14: Inductive part $L_v(\omega,\tau)$ of the vortex medium as a function of the measurement frequency for temperatures above the transition. The measurements are in good agreement with the frequency power-law behavior predicted by theory, Eq. (5.45). Notice the temperature dependence of the exponent.

- we calculated $L_*(\omega,\tau)$ with Eq. (5.30) using the measured $R_\square$ and $L_\square$ and the values of R_0 given by Fig. 5.12. Since $L_* = L_0 + L_v$, where L_0 is independent of frequency, the logarithmic derivative of L_*, using Eq. (5.45), is predicted to be:

$$\frac{\delta L_*(\omega,\tau)}{\delta \ln \omega} = \omega \frac{\delta L_v(\omega,\tau)}{\delta \omega} \propto \omega^{u(\tau)-1} \quad \text{for } \tau > \tau_c \ . \tag{5.47}$$

This allows to verify the power-law behavior of $L_v(\omega, \tau)$ as a function of frequency and to find the temperature dependence of $u(\tau)$ predicted by Eq. (5.45) without needing a specific $L_0(\tau)$.

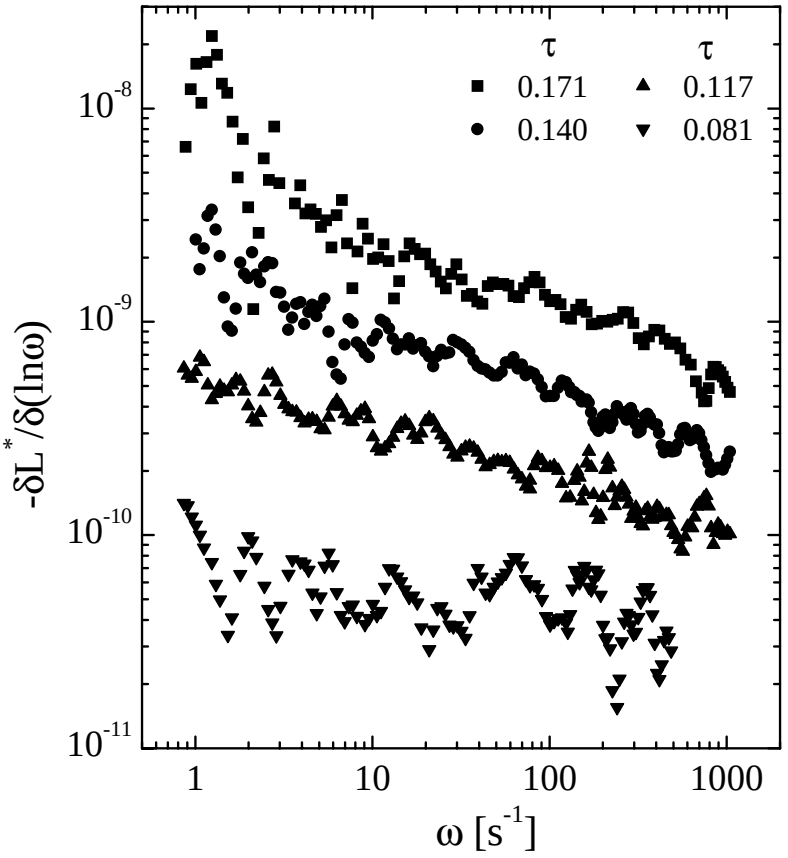

Figure 5.15: Derivative of $-L_*(\omega, \tau)$ for several reduced temperatures as a function of frequency. In spite of the large amount of noise due to the numerical calculation of the first derivative, the power-law behaviour with a temperature dependent exponent is visible.

In spite of their difference, the two methods lead to similar results. The values obtained with the first method are reported in Fig. 5.14, while the derivative of $L_*(\omega, \tau)$ as obtained with the second method is shown in Fig. 5.15. The noise in the data of Fig. 5.15 is mainly due to the numerical calculation of the first derivative.

According to Eq. (5.45), the inductive part of the bound pair response should follow a power-law with a temperature dependent exponent: $L_v \propto \omega^{u(\tau)-1}$ as shown qualitatively by Figs. 5.14 and 5.15. Notice, in particular, that the exponent $u(\tau) - 1$ tends to 0 as τ approaches τ_c. The deviation from the power-law behaviour due to the appearance of single vortices is also observed for $L_v(\omega, \tau)$ at reduced temperatures > 0.120 at the lower frequencies.

The isotherms of Figs. 5.13 and 5.14 allow to determine the temperature dependence of $u(\tau)$. To exclude the contribution of single vortex excitations, the exponent extracted from the resistive data was determined from the slopes shown by the dashed lines in Fig. 5.13. The result of this analysis is shown in Fig. 5.16. We notice, first of all, that the exponents extracted from R_v and L_v are consistent with each other. By extrapolating the data at $u(\tau_c) = 1$, we infer a critical reduced temperature $\tau_c \approx 0.055$, which compares reasonably well with the approximate theoretical prediction $\tau_c(p) \approx \tau_c(1)\, 4.5\, [(p - p_c)/(1 - p_c)]^{\mu} \approx 0.071$ obtained using $\tau_c(1) \approx 1.5$ [68]. However, the experimental $u(\tau)$ exhibits a much slower temperature dependence than the theoretical prediction $u(\tau) = 2\,\tau_c/\tau - 1$ (dashed line in Fig. 5.16), thus making the BKT interpretation of the response questionable. In this connection, we notice that the prediction $u(\tau) = 2\tau_c/\tau - 1$ is, strictly speaking, valid only very close to τ_c, where the bound-pair density is assumed to be small. One could therefore attribute this discrepancy to an enhanced pair density well above τ_c. However, such a scenario would require the presence of an appreciable population of vortices also in the small holes (of sizes $\ll \xi_p$) of the fractal structure of the array. This is difficult to understand, since the nucleation energy to create vortices in such small holes is too high.

An alternative dynamical theoretical approach, not based on bound pair dynamics in the quasi-homogeneous Euclidean regime, could rely on vortex excitations moving in the hierarchical pinning potential of the lattice. This would result in a glass-like dynamics. But, again, it's difficult to conceive of the presence of vortices in the small holes, due to their large nucleation energy when created in small holes.

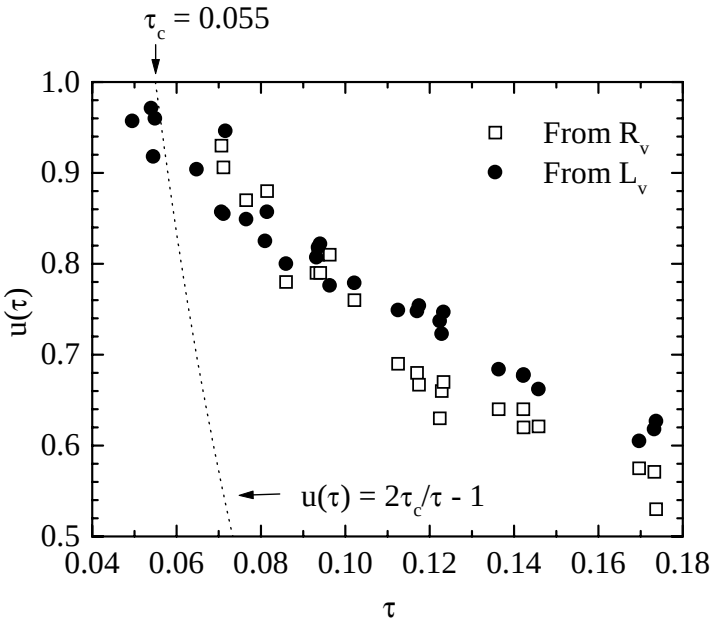

Figure 5.16: Temperature-dependent exponent $u(\tau)$ deduced from the measurements of $R_v(\omega, \tau)$ and $L_v(\omega, \tau)$. The dashed line is the theoretical prediction calculated with $\tau_c = 0.055$.

To complete this analysis, notice, for $\tau > \tau_c$, the possibility to compare directly the frequency dependence and the temperature dependence of $R_v(\omega, \tau)$ and of $L_v(\omega, \tau)$ by taking into account the ratio (see Eqs. (5.43) and (5.45)):

$$\frac{R_v(\omega, \tau)}{\omega L_v(\omega, \tau)(1 - u(\tau))} = \frac{\pi}{2} , \tag{5.48}$$

in the regime dominated by bound pairs of vortices. We reported the ratio of these measured quantities in Fig. 5.17 at several reduced temperatures. Moreover, the average of the data is shown by a dashed line for each temperature.

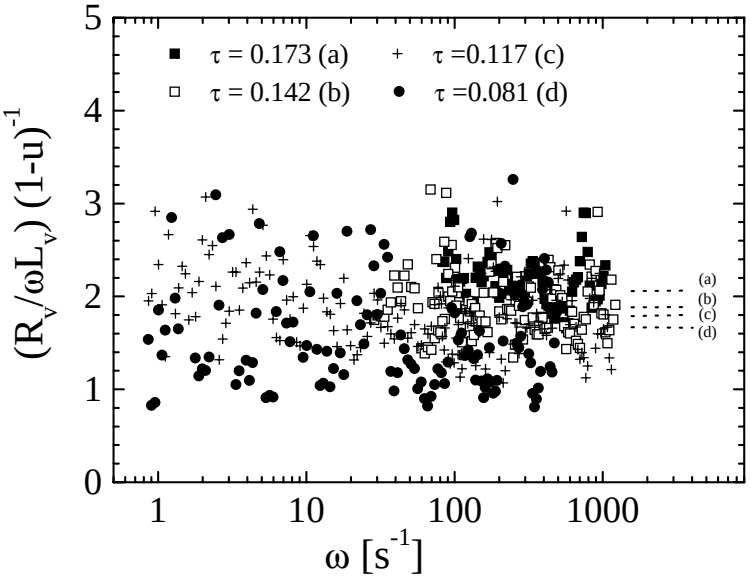

Figure 5.17: Ratio between the inductive and the resistive part of Z_v at several reduced temperatures in the region dominated by vortex-antivortex bound pairs. Notice the frequency independent behavior of this quantity. The dashed lines show the averages performed for each temperature.

In spite of a large scattering, one observes that the data shown in Fig. 5.17 are independent of frequency, as predicted by Eq. (5.48). Moreover, one notices that the discussed ratios are slightly temperature dependent, and converge to the predicted value $\pi/2$ when approaching the critical temperature. This is maybe due to the fact that, strictly speaking, Eq. (5.48) is only valid very close to τ_c.

To conclude this section, we notice that the frequency range reflecting the dynamics of bound pairs in the quasi-homogeneous (Euclidean) two-dimensional regime should be limited, on the high-frequency side, by the condition $\omega\tau_{Dp} \approx 1$ (see section 5.5.3), where $\tau_{Dp} \approx \xi_p^2/14D_v$ and the vortex diffusion constant D_v is related to the vortex mobility μ_v by $D_v = \mu_v k_B T$. Since vortex diffusion in arrays with percolative disorder close to the

threshold is limited by an energy barrier $\Delta \simeq 2E_J$ (see section 5.6.2), the vortex mobility is thermally activated and given by $\mu_v = \mu_{0v} \exp(-\Delta/k_B T)$, where $\mu_{0v} \approx R_N \xi_p^2/\phi_0^2$ is the free vortex mobility. Taking $T = 5\,\mathrm{K}$ ($\tau = 0.1$) as a representative value for the temperatures of interest, we find that $1/\tau_{Dp}$ is orders of magnitude lower than the upper frequency limit (in the $10^2 - 10^3\,\mathrm{sec}^{-1}$ range) of the power-law regime corresponding to bound pair dynamics in Fig. 5.9. In other words, the vortex mobility in percolative arrays appears to be much higher than the one resulting from our simple estimate. A possible explanation could rely on the partner transfer mechanism between members of small and large pairs proposed in reference [69], a process implying an activation energy much less than that for single vortex diffusion. However, this scenario would require the presence of an appreciable vortex population in small holes, which, in view of the large nucleation energy for vortices in small holes, is quite unlikely at the temperatures of interest.

5.6 Single vortex dynamics

5.6.1 Introductory remarks

The disordered structure of our array is a result of its percolative character which has been created by removing superconducting islands from a regular triangular lattice. On the other hand, the normal metal layer is homogeneous over the whole area of the sample. Effects related to percolation will therefore be felt when the physical properties of the lead islands determine the behavior of the array, at temperatures of the order or less than τ_c. By considering the scheme shown in Fig. 5.8, we can postulate that the normal channel resistance is given by $R_0(\tau \lesssim \tau_c) \propto R_J(\tau)(p - p_c)^\mu$ at temperatures smaller than or equal to τ_c, whereas it loses its percolative character at temperatures well above τ_c and becomes $R_0(\tau \gg \tau_c) \approx R_N \approx R_J(T_{cs})$. In this section, we are concerned with the dynamics of independent vortices which becomes relevant in the temperature range above τ_c. These considerations allow to neglect the normal channel ($R_J(T_{cs}) \gg Z_v$ and $R_J(T_{cs}) \gg \omega L_0$) at the temperatures and frequencies of interest, and one obtains:

$$R = R_v, \quad L = L_0 + L_v \quad \text{and} \quad L_\square^{-1} = L^{-1}\left[1 + \left(\frac{R_v}{\omega L}\right)^2\right]^{-1}. \tag{5.49}$$

Quite generally, the vortex impedance can be written:

$$Z_v = \phi_0^2 (n_v + n_f)\mu_v, \tag{5.50}$$

where $n_v \approx 1/\xi_+^2$ is the density of thermally nucleated vortices, n_f the density of field induced vortices, and μ_v their mobility. Above τ_c, the mean distance ξ_+ between 2 free vortices exhibits, according to Eq. (5.27), an exponential inverse square root temperature dependence [52]. With increasing temperature, it decreases extremely fast near τ_c, then tends toward ξ_p. Since the physical phenomena described in this chapter occur well above τ_c, we consider hereafter the limit $\xi_+(\tau) \mapsto \xi_p$, leading to the estimate $n_v \simeq 1/\xi_p^2$.

5.6.2 Energy barrier in percolative arrays near p_c

Due to its fractal geometry, the array contains loops of all sizes smaller or equal to ξ_p. By analogy with the Sierpinski gasket [50], the vortex nucleation energy in a loop of size R_t is given by $E_N \propto E_J\,(a/R_t)^{\zeta}$ with $\zeta = \mu/\nu$ in two dimensions, and thermally nucleated vortices are most likely in the largest loops, of size of order of ξ_p. Within the framework of a simplified model, in the following, we thus consider the motion of single (non-interacting) vortices in an array consisting of loops of size ξ_p, each of them containing M junctions (see Fig. 5.18). We calculate [67, 47] the energy barrier Δ for one vortex to jump from one hole of size ξ_p to another. The energy Δ is found by taking the energy difference between two vortex positions in the array: we first consider a vortex located at the equilibrium position in the middle of a hole of size ξ_p, then at the saddle point in the middle of the edge of a hole (see Fig. 5.19).

Consider first a single vortex located in the middle of a hole of size ξ_p containing M junctions along its edge, as depicted in Fig. 5.18. The vortex position is indicated by a cross, and the phase difference between two adjacent islands i and j by $\Delta\varphi_{ij}$.

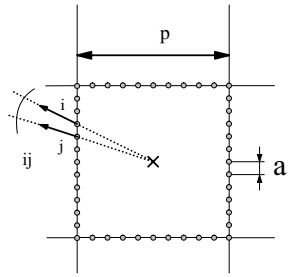

Figure 5.18: Single vortex located in the middle of a hole of size ξ_p. The vortex position is indicated by a cross, and the phases of the superconducting islands i and j are represented by arrows. For our qualitative estimate, the geometrical factor determined by the shape of the hole is not important.

Approximating the square loop by a circular one having the same perimeter to simplify the calculations, we find that the contribution of the loop to the vortex energy is given by:

$$\widetilde{E}_{\xi_p} = E_J \sum_{<ij>} (1 - \cos \Delta\varphi_{ij}) \simeq E_J \left[1 - \cos \frac{2\pi}{M}\right] M \approx \frac{\pi^2}{2} E_J \frac{a}{\xi_p}\,, \tag{5.51}$$

where the last equality is obtained by assuming M large enough to expand the cosine to the lowest order. Since the hole is part of a structure with fractal geometry, this " isolated-hole " result is modified as follows:

$$E_{\xi_p} \approx \frac{\pi^2}{2} E_J \left(\frac{a}{\xi_p}\right)^{\zeta} \approx \frac{\pi^2}{2} E_J \left(\frac{p - p_c}{1 - p_c}\right)^{\mu}. \tag{5.52}$$

This relation provides an estimate only of the core energy of the vortex. Its total energy is easily found by noticing that, at length scales larger than ξ_p, the system is two dimensional and therefore:

$$E_m \approx E_{\xi_p} \ln \frac{Na}{(2/\pi)\xi_p} \approx \frac{\pi^2}{2} E_J \left(\frac{a}{\xi_p}\right)^{\zeta} \ln \frac{Na}{(2/\pi)\xi_p} \tag{5.53}$$

where N is the total number of junctions on one side of the array. We now estimate the vortex energy for the vortex position at the saddle point:

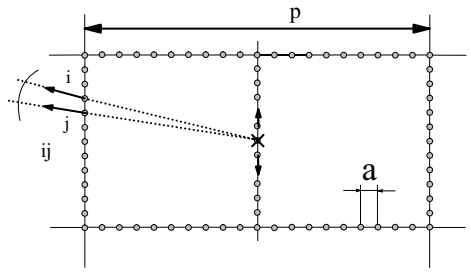

Figure 5.19: Single vortex located on the edge of a hole of size ξ_p. Symbols are those of the previous figure.

The contribution emerging from the junction on the edge where the vortex is located is given by $E_s = E_J(1 - \cos\pi) = 2E_J$. By performing a development analog to the one carried out above, with a loop of length $6\,\xi_p$ enclosing the vortex, as shown in Fig. 5.19, we find the contribution to the vortex energy due to the loop:

$$\widetilde{E}'_{\xi_p} \approx \frac{\pi^2}{3} E_J \frac{a}{\xi_p}. \tag{5.54}$$

By taking into account the fractal structure of the array and the contributions from length scales larger than ξ_p, we can now deduce the total energy E_b for a vortex situated at the saddle point:

$$E_b = E_s + E'_{\xi_p} \ln \frac{\pi Na}{3\xi_p} \approx 2E_J + \frac{\pi^2}{3} E_J \left(\frac{a}{\xi_p}\right)^{\zeta} \ln \frac{\pi Na}{3\xi_p}. \tag{5.55}$$

Finally, the energy barrier Δ is given by taking the difference between Eq. (5.55) and Eq. (5.53), leading to:

$$\Delta \approx 2E_J - \pi^2 E_J \left(\frac{p - p_c}{1 - p_c}\right)^{\mu} \left[\frac{1}{6} \ln \frac{Na}{a} \left(\frac{p - p_c}{1 - p_c}\right)^{\nu} + 0.21\right]. \tag{5.56}$$

For $p \mapsto p_c$ the second term in Eq. (5.56) vanishes, reducing considerably the corrections for arrays near the percolation threshold, so that $\Delta \approx 2E_J$ which is, remarkably, the

barrier for an isolated junction. For our sample, the second term in Eq. (5.56) is smaller then $0.1 \cdot E_J$, and thus negligible with respect to the first one. The result $\Delta \approx 2E_J$ has been used to determine the constant $b^{-\zeta} \approx 4.5$, and therefore to refine the reduced temperature scale through Eq. (4.5).

5.6.3 Independent Brownian particle model

Let us begin by writing the equation of motion for a single vortex (i.e. non-interacting with other vortices) considered as a Brownian particle in a pinning potential $U(\vec{r})$ [70, 71, 61]:

$$m\ddot{\vec{r}} + \eta\dot{\vec{r}} + \vec{\nabla}U(\vec{r}) = \vec{F}(t') + \vec{F}_D, \tag{5.57}$$

where m is the vortex mass, $\vec{r}$ its coordinate, η the viscosity, $\vec{F}(t')$ the Langevin fluctuating force, and $\vec{F}_D$ the externally applied driving force.
Some comments on Eq. (5.57) are in order:

- $m\ddot{\vec{r}}$: vortex inertia. This term becomes important only at high frequencies or when the junction capacitance is not negligible [72]. For SNS junctions and for our measurement frequencies this term can be neglected;
- $\vec{\nabla}U(\vec{r})$: pinning force arising from the pinning potential $U(\vec{r})$. In spite of the random nature of $U(\vec{r})$ in percolative arrays, to describe vortex motion in the two-dimensional quasi-homogeneous regime, it seems reasonable, to a first approximation, to replace $U(\vec{r})$ by a sinusoidal potential of amplitude $\Delta/2$ and periodicity $q = 2\pi/\lambda$ [73]. With regard to the considerations of the previous subsection, we expect $\lambda \simeq \xi_p$ and $\Delta = 2E_J$;
- $\vec{F}(t')$: Langevin fluctuating force, related (white noise) to the uncorrelated thermal fluctuations $< F(t')F(0) >_{t'} = 2\eta k_B T\delta(t')$. The dissipation described by η is therefore due to the coupling with fluctuations.

In the overdamped Smoluchowski limit, where viscous friction dominates, Eq. (5.57) leads to the following complex vortex mobility [74]:

$$Re\,\mu_v = \mu_{0v}\frac{I_0^{-2}(z) + (\omega t)^2}{1 + (\omega t)^2} \quad \text{and} \quad Im\,\mu_v = \mu_{0v}\frac{\omega t[1 - I_0^{-2}(z)]}{1 + (\omega t)^2} \tag{5.58}$$

$$\text{with} \quad t = t_p\frac{I_0^2(z) - 1}{I_0(z)I_1(z)} \quad \text{and} \quad t_p = \frac{2}{\mu_{0v}\Delta q^2}, \tag{5.59}$$

where $I_0(z)$ and $I_1(z)$ are modified Bessel functions of order 0 and 1 respectively, and μ_{0v} the free vortex mobility. The variable $z \equiv \Delta/(2k_BT)$ becomes $z = 1/\tau$ if one takes an amplitude $\Delta = 2E_J$ for the energy barrier of the sinusoidal pinning potential. Moreover, notice that for our measurement frequencies: $(\omega t)^2 \ll 1$.

5.6.4 Response at $f = 0$

In the experiment reported below, the regime of interest is such that $z = 1/\tau > 1$, and corresponds to the strong pinning limit (or barrier limited vortex diffusion). In this regime, the Bessel functions $I_0(z)$ and $I_1(z)$ can be approximated by exponential functions, leading to $t \simeq t_p$, where t_p is the characteristic time for viscous relaxation for a vortex in the periodic pinning potential. With $n_f = 0$ in Eq. (5.50), one obtains:

$$R(\tau) = R_v(\tau) = \frac{\phi_0^2}{\xi_p^2}\mu_{0v}\frac{2\pi}{\tau}\, e^{-2/\tau} \approx R_N e^{-2/\tau}\ , \quad \text{and} \tag{5.60}$$

$$L(\tau) = L_0 + L_v = L_0(\tau) + \frac{\lambda^2}{2\pi\xi_p^2}L_J(\tau). \tag{5.61}$$

Since the prefactor of the exponential in the first part of Eq. (5.60) varies very slowly ($\sim 1/\tau$) compared to the exponential factor, the temperature dependence of R_v is dominated by the exponential term. In first approximation, we will therefore neglect the temperature dependence of this prefactor; this leads to the last part of Eq. (5.60), where the prefactor of the exponential is equal to the sheet resistance R_N, relevant for temperatures well above τ_c.

Eq. (5.61) can be simplified in the 2D regime, where we expect the periodicity λ of the pinning potential to be of the order of ξ_p, leading to $L_v \simeq L_J(\tau)$ much smaller than L_0, and accordingly to $L(\tau) = L_0 + L_J \propto L_J(\tau)(p - p_c)^{-\mu}$. This last equality means that the vortex contribution to the total inductance is negligible. The quantity measuring the degree of superconducting phase coherence is $L_\square^{-1}$ as given by Eq. (5.49). In the high-temperature single vortex regime, $R_v \gg \omega L \approx \omega L_0$ at our measuring frequencies, so that:

$$L_\square^{-1}(\omega, \tau) \simeq \frac{L_0(\tau)}{R_N^2}\omega^2 e^{4/\tau}. \tag{5.62}$$

We have therefore an ω^2 dependence prediction in this high temperature regime, coupled with an exponential temperature law.

5.6.5 Response at $f \neq 0$

In the previous section, we described the response of an unfrustrated array well above the critical temperature assuming a constant number of thermally nucleated vortices $n_v \sim 1/\xi_p^2$. Experimentally, a better control of the vortex density can be achieved by exposing the array to a weak external magnetic field B.

For our triangular structure, the frustration is $f = \sqrt{3}\, Ba^2/(4\phi_0^2)$, leading to a field induced vortex density n_f given by $n_f = 4f/(\sqrt{3}\, a^2)$. The regime we are interested in is characterized by single vortex dynamics, implying a linear Z_v vs f dependence as expressed by Eq. (5.50). Deviations from linearity indicate the presence of vortex-vortex interactions.

Moreover, since our 2D approach is only valid to describe the response of vortices separated by distances larger than ξ_p, the field induced vortex density n_f must be smaller than $1/\xi_p^2$, leading to a maximum frustration value $f_c = \sqrt{3}\,a^2/(4\xi_p^2)$, above which our two-dimensional description is no longer valid. With Eqs. (5.60) and (5.50), we obtain a prediction for the resistance due to independent vortex dynamics:

$$R_v(\tau, f) \simeq \phi_0^2 n_v Re\{\mu_v\}[1 + \frac{n_f}{n_v}] \simeq R_N e^{-2/\tau}[1 + \frac{f}{f_c}]. \tag{5.63}$$

The first derivative of R_v with respect to frustration is proportional to the real part of the mobility:

$$\frac{\partial R}{\partial f} = \frac{R_N}{f_c} e^{-2/\tau}. \tag{5.64}$$

We find again a thermally activated behavior independent of the measurement frequency. For the inductive part of the response, at temperatures $z > 1$, where $L_v \simeq L_J$:

$$\frac{\partial L}{\partial f} \simeq \frac{L_J(\tau)}{f_c}\,. \tag{5.65}$$

The inductive part of the response is therefore not-activated and independent of ω.

5.6.6 Measurements in the high temperature limit

At temperatures well above the critical temperature τ_c and at sufficiently low frequencies, the vortex pair contribution becomes negligible, as shown in section 5.5.5. The response enters a regime dominated by free vortices. If the vortex density is small enough to neglect the vortex-vortex interactions and if the mean distance between them is larger than ξ_p, one can consider the vortices as independent entities moving in a 2D Euclidean geometry. The equations of sections 5.6.4 and 5.6.5 will then be valid. In this section, we compare experiment and theory for temperatures well above τ_c. First, we discuss the data taken without frustration and then we will discuss measurements in a small magnetic field.

In accordance with Eq. (5.60), the temperature dependence of $R(\omega, \tau)$ is dominated by an exponential, and is frequency independent. This prediction is clearly verified in Fig. 5.20 where the resistance is shown on a logarithmic scale as a function of the inverse reduced temperature for several measurement frequencies. The data meet on the same straight dashed line, independently of the measurement frequency in the temperature range $1 \leq 1/\tau \leq 6$. This is the signature of a thermally activated behavior, and a characteristic of single vortex dynamics.

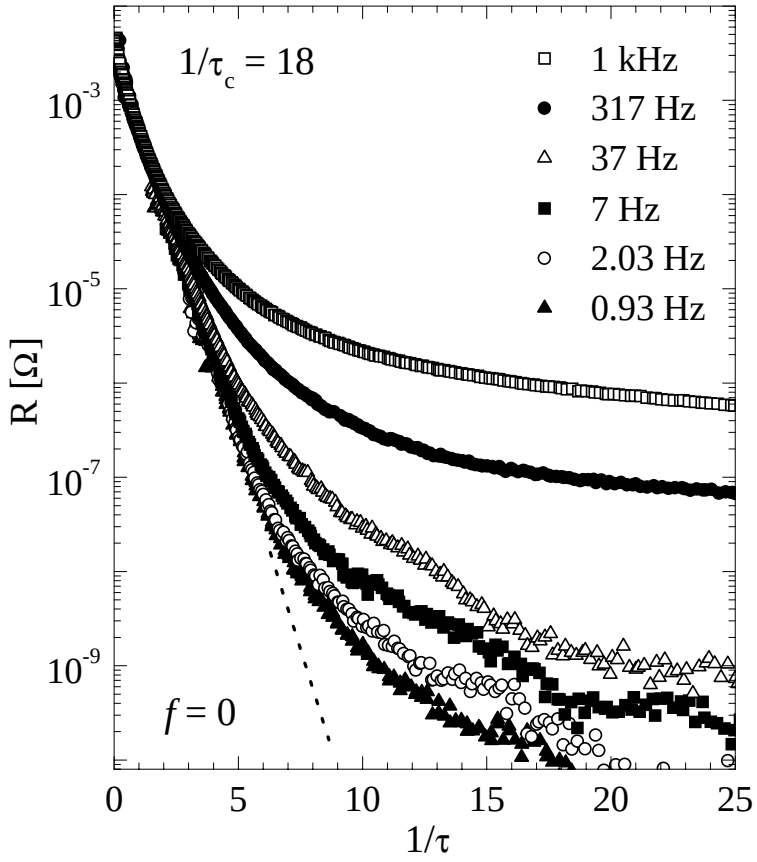

Figure 5.20: Resistance of the array in the high temperature regime at several frequencies. The data fall on the same straight line, independent of the measurement frequency in the temperature range $1 \leq 1/\tau \leq 6$. This is the signature of a thermally activated behavior.

When we defined the reduced temperature scale in section 4.4.1, we used the relation $\Delta = 2E_J$ defining the typical energy barrier for vortices moving in an array with a percolation fraction near p_c. It would then be illusory to extract Δ from the slope of the dashed straight line of Fig. 5.20, because it is equal to 2 due to the definition of τ. On the other hand, from the fit in the thermally activated regime, it is possible to find the sheet resistance of the proximity effect plateau, equal to the prefactor of Eq. (5.60). A value of 3.2 mΩ is deduced from the fit, in good agreement with the value 4.7 mΩ inferred from standard 4-probe resistive measurements.

The superfluid part of the response is shown in Fig. 5.21 and exhibits a thermally activated behaviour at temperatures well above τ_c. To demonstrate the quadratic frequency dependence predicted by Eq. (5.62), we report $[\omega^2 L_\square L_0]^{-1}$ as a function of $1/\tau$ for several measurement frequencies. The thermally activated regime for the single vortex excitations leads to a slope of value $2\Delta = 4.5$ in the temperature range $1 \leq 1/\tau \leq 5$. With Eq. (5.62), we estimate the sheet resistance of the proximity effect plateau by fitting

the data in the thermally activated regime, represented by a dashed line in Fig. 5.21. The resistance deduced from the fit is 12 mΩ, a satisfactory result, even if this value is three times larger then the value inferred from usual 4-probe resistive measurements.

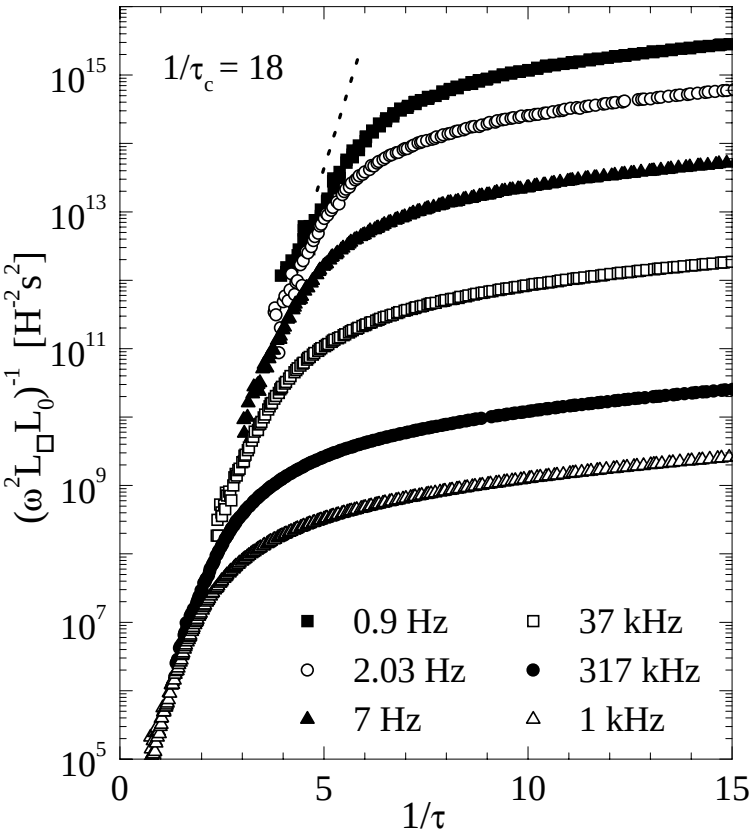

Figure 5.21: Superfluid part of the response in the high temperature regime at several measurement frequencies. The data meet on the same straight line independently of the measurement frequency in the temperature range $1 \leq 1/\tau \leq 5$. This is the signature of a thermally activated behavior.

A measurement obtained by sweeping the external magnetic field around $f = 0$ at constant temperature and frequency is shown in Fig. 5.22. These data were acquired at the low measurement frequency of 7 Hz and at a reduced temperature $\tau = 0.2$, well above τ_c.

As predicted by Eq. (5.64), one observes a linear behavior of the resistance as a function of frustration in the vicinity of $f = 0$. In this domain, the resistance is therefore proportional to the density of field induced vortices, which may thus be considered independent particles. Deviations from the linear behavior appear at frustrations $|f| > |f_s|$, maybe indicating the transition to a fractal dynamics or the appearance of vortex-vortex interactions. Notice in particular that the commensurability effects between the vortex lattice and the structure of the array occur below $|f_c| \simeq 0.35\%$ which is defined as the

first minimum. In comparison with a regular triangular array [61], the values of f_s and f_c are small. This can be understood by taking into account the renormalization of the frustration scale by an amount $(a/\xi_p)^2$ due to the introduction of a superlattice of lattice constant ξ_p.

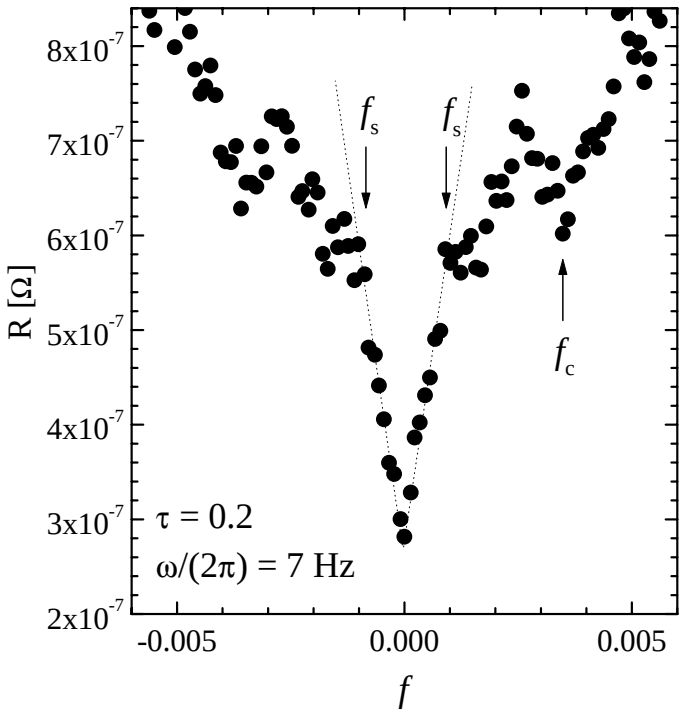

Figure 5.22: Measurement obtained by sweeping the external magnetic field around $f = 0$ at the constant temperature $\tau = 0.2$ and at the frequency $\omega/(2\pi) = 7\,\mathrm{Hz}$. In the vicinity of $f = 0$, the resistance is proportional to the number of field induced vortices, which may therefore be considered as independent entities.

By analogy with the behavior of a regular array, the minimum of the resistive curve at the frustration f_c can be associated with the filling of each hole of size ξ_p of the superlattice with a vortex. This situation corresponds to the case $f = 1$ for a regular lattice and is expressed by the relationship $f_c = \sqrt{3}/4(a/\xi_p)^2$. This leads, by using $f_c = 0.35\%$, to a value $\xi_p \approx 11\,a$, in reasonable agreement with the value $\xi_p \approx 30\,a$ estimated with Eq. (4.1). Because the location of the holes of size ξ_p is not ordered in the structure of the array, the commensurability effects are not observable for frustrations smaller than f_c for our percolative array.

In the domain $|f| < |f_s|$ of small frustrations and in the temperature region of the thermally activated regime, the resistance will depend linearly on frustration, as predicted by Eq. (5.64). In particular, this relationship predicts an exponential variation of $\delta R/\delta f$ with characteristic energy barrier $\Delta = 2E_J$.

To check the validity of these predictions, we carried out several frustration sweeps around $f = 0$ at reduced temperatures in the thermally activated domain at a frequency of 160 Hz. We plot the slopes $\delta R/\delta f$ on a logarithmic scale as a function of $1/\tau$ in Fig. 5.23.

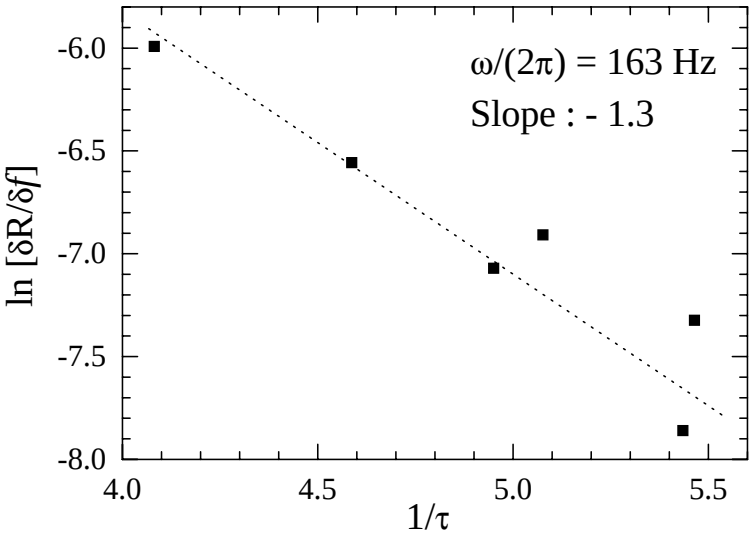

Figure 5.23: Slopes $\delta R/\delta f$ of measurements performed at 160 Hz at several reduced temperatures in the thermally activated domain. The fit, represented by a dashed line, gives an estimate of the energy barrier for vortex motion in the array of junctions.

In spite of the scatter of the data at the lowest temperatures, the measurements shown in Fig. 5.23 fall on a straight line, therefore confirming the presence of a thermally activated behavior. The slope of the dashed line gives an independent estimate of the energy barrier. Even if smaller than predicted, the experimental value $\Delta \simeq 1.3E_J$ is consistent with the estimate deduced from Figs. 5.20 and 5.21. This too small experimental value of Δ is maybe the consequence of a weak random variation of the coupling energy of the junctions (see section 4.3). The barrier energy of some junctions would then be reduced, leading to a too weak experimental determination of Δ.

Chapter 6

Modulated arrays

6.1 Theoretical background

6.1.1 Introduction

The critical behavior of the unfrustrated regular JJAs has been the subject of much work [1, 2], and is relatively well understood. This behavior is described by a quasi-long-range order at low temperature, which is broken at the Beresinskii-Kosterlitz-Thouless transition temperature by the dissociation of vortex-antivortex bound pairs. The critical behavior of frustrated arrays, on the contrary, is more complex and still not well understood, because of the appearance of two kinds of excitations in the critical region. In addition to vortices, which may be considered point-like defects, linear defects called domain walls could appear in frustrated arrays. The interplay between these two kinds of excitations in the critical region is still not completely understood, and even the nature of the transition is controversial. The aim of this work is to gain some insight in the phenomena appearing in the critical region of such arrays, by studying a fully frustrated array with modulated coupling energies in one direction. We explain in section 6.1.3 and in section 6.1.4 that this geometry allows to split the effects related to the appearance of point-like and linear defects. In this way, it is in particular possible to study more precisely the properties of domain walls.

6.1.2 Regular array at full frustration

The aim of this section is to present some results about the fully frustrated square arrays of junctions, and to introduce notions which will be useful for the description of modulated arrays. Let us first remember that the Hamiltonian of a square array at full frustration, i.e. one where each unit cell carries one half flux quantum of external magnetic field, can be written in the framework of the 2D XY model [10]:

$$H = -E_J \sum_{<ij>} \cos(\varphi_j - \varphi_i - A_{ij}), \tag{6.1}$$

where φ_i represents the phase of the superconducting node at site i, and E_J is the coupling energy of an isolated junction; the sum is performed over nearest-neighbor sites only. A_{ij} is the integral from node i to j of the vector potential due to the external magnetic field and allows to introduce the frustration f of the system. In the Landau gauge (i.e. $\overrightarrow{A} = (0, Bx, 0)$), the quantities A_{ij} are 0 for all horizontal bonds and will alternate between 0 and π on the vertical bonds [12]. By substituting these values in Eq. (6.1), one sees that each plaquette of the array possesses three " ferromagnetic " coupling constants of value $+E_J$ and one " antiferromagnetic " link of value $-E_J$. The phase configuration [12] corresponding to the ground state is shown in Fig. 6.1 (a); it leads to gauge invariant phase differences equal to $\pm\pi/4$. Equivalently, the ground state can be depicted with the help of the supercurrents between each island of the array. One can then notice, as shown in Fig. 6.1 (b), that supercurrents of equal magnitude circulate in a clockwise or counterclockwise sense on the plaquettes of the array. The ground state is thus a checkerboard, and it's possible to identify vortex-bearing plaquettes as those about which current circulates in a chosen sense, implying a double degeneracy of the ground state.

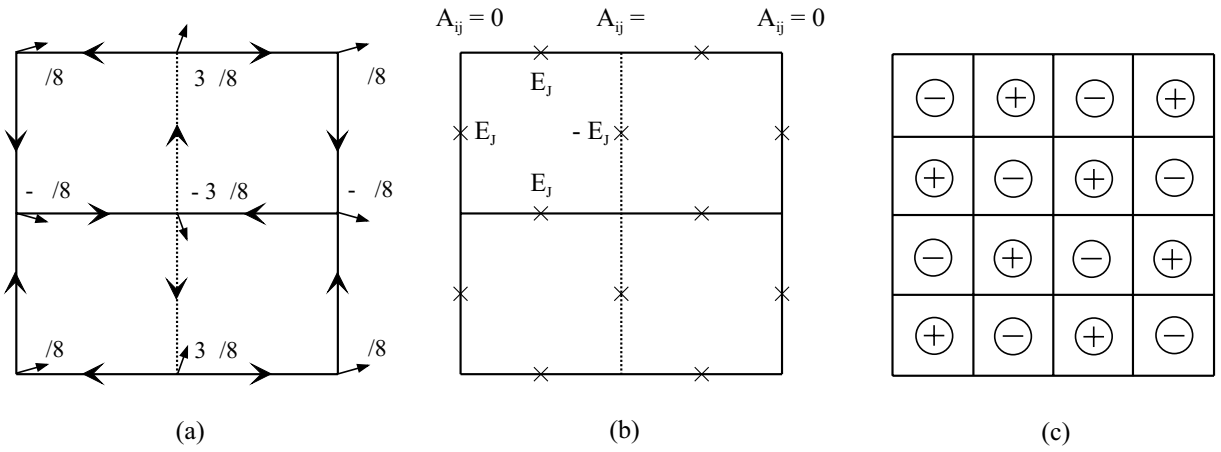

Figure 6.1: (a) Phase and current configurations in the ground state [12]. The arrows located at the nodes of the array represent the phases associated with each superconducting island. Notice that the ground state has a checkerboard form, alternate plaquettes having currents circulating in opposite sense. (b) An equivalent picture is obtained by considering an array with three " ferromagnetic " bonds (full lines) and one " antiferromagnetic " bond (broken line) for each plaquette. The crosses represent the positions of the junctions. (c) Equivalently, the checkerboard ground state in the Coulomb gas picture is obtained by using effective charges with alternating signs. They have half-integer values and are situated on the sites of the square lattice.

To understand the phenomena occurring as one moves away from the ground state, it's useful to introduce a representation of the system in the Coulomb gas picture [77]. The model in terms of phases is then substituted by a system of half-integer charges which

in the ground state are equal to $\pm 1/2$ and alternate, as shown in Fig. 6.1 (c). The ground state is therefore doubly degenerated.

The low temperature ordered phase becomes unstable with respect to two different types of excitations, which must conserve charge neutrality and correspond to rearrangements of the ground state charges. The first, of the BKT-type, consists of the interchange of a given pair of $+1/2, -1/2$ charges [7, 8, 11], as shown in Fig. 6.2 (a), where positive and negative signs represent half-integer charges of different signs. The unbinding and recombination of pairs give rise to the BKT-transition. The second instability results from excitations which we call Ising type excitations [11]. These consist of a domain of opposite chirality, within the ordered phase, formed by flipping nearest-neighbor pairs of charges. The nucleation of these Ising domains causes the system to switch between the two ground states, destroying the Ising order present in equilibrium. These regions of opposite chirality are separated by linear defects called domain walls, as shown in Fig. 6.2 (b).

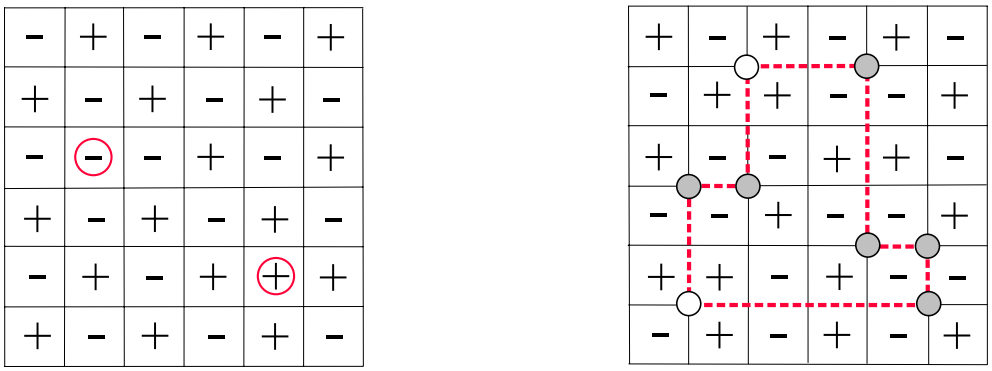

Figure 6.2: Thermal excitations in the 2D Coulomb gas analogy [11]. The positive and negative signs represent half-integer charges of opposite signs. (a) Point defects due to the exchange of two charges of opposite sign. The unbinding of these dipoles suppresses the phase order and produces the BKT transition. (b) Domain of opposite chirality in the ordered phase. Domain walls represented by a dashed line separate the two phases and carry $+1/4$ (empty circles) and $-1/4$ (full circles) charges at the corners. Their proliferation leads to a suppression of chiral order.

To understand the influence of domain walls on the behavior of the system, we have to understand how they affect charge transport. This can be partially achieved by considering the domain wall shown in Fig. 6.2 (b), which reveals that domain walls have a peculiar property: all the charges effectively average out except for the corner of the domain walls where fractional $\pm 1/4$ charges appear.

When the system is in the Ising ordered phase the domain walls are short and form small loops with a net integer charge due to the $1/4$ charges at each corner. These integer charges can exhibit a BKT-transition. However, as soon as the Ising-transition takes place, the domain walls increase and large domains can occur. This means that there are

now free fractional charges present. Since these charges screen the Coulomb potential, they will play an important role in the critical behavior of the system.

Until now, the interplay between these different excitations in the critical region is not completely understood. Recent Monte Carlo simulations [11] suggest a critical behavior associated with the chiral order parameter, but are not sufficiently accurate in the critical region to distinguish between a single transition with a mixed character or two distinct transitions appearing very close to each other.

Only few measurements [78, 79, 80, 81] have been performed to investigate the behavior of square arrays at full frustration. Experimental data [78, 79] obtained by probing the response (IV curves and resistive measurements) of tunnel junction arrays seem to indicate that the array exhibits at $f = 1/2$ a BKT-like transition with a non-universal jump. But on the other hand, inductive measurements performed on arrays of proximity effect junctions [80, 81] are consistent with a description of a phase transition at $f = 1/2$ within the framework of the BKT ideas. Because these experiments were performed with different kinds of arrays and with different experimental techniques, it's nevertheless difficult to directly compare their results and to extract some general conclusions. Moreover, the exact role and the interplay between domain walls and vortices at full frustration are not clearly determined from an experimental point of view; in particular, these measurements do not provide a complete information about the appearance of an Ising-like transition.

6.1.3 Arrays with modulated couplings in one direction

The purpose of this section is to understand how the behavior of the fully frustrated regular array discussed in section 6.1.2 is modified when the coupling constants are modulated in one direction. The first step consists in describing the ground state of the modulated arrays [82]. Next we study qualitatively the nature of the phase transition in the 2D modulated lattice at full frustration [82, 83, 84, 85]. A more quantitative description is given in section 6.1.4 which will allow a comparison with the experimental results.

Let us remember that the modulation of the coupling energy has been obtained by varying the length of one of the junctions of each plaquette (see Fig. 4.4), as explained in section 4.2.2.

Ground state of the modulated array

The ground-state configuration of the modulated array shown in Fig. 6.3 can be derived analytically [82] by considering its Hamiltonian:

$$H_{mod} = -\sum_{<ij>} E_J^{ij} \cos(\varphi_i - \varphi_j - A_{ij}), \tag{6.2}$$

with nearest-neighbor interactions E_J^{ij} equal to E_J for positive bonds represented by full lines in Fig. 6.3 (a) and to ηE_J for bonds which are represented by broken lines. The modulation parameter η varies from -1 to infinity: $\eta = 1$ corresponds to the unmodulated fully frustrated case of section 6.1.2 while $\eta = -1$ corresponds to the isotropic "

ferromagnetic " case. In the following we will use the terms strong bonds (SB) and weak bonds (WB) to indicate the bonds with the largest and smallest value of E_J^{ij}, respectively.

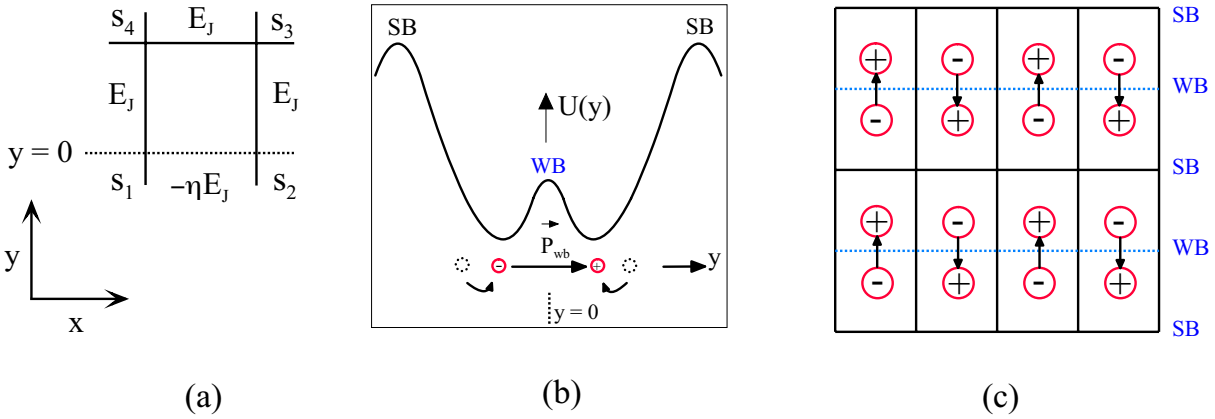

Figure 6.3: Schematic description of the ground state of a modulated array. (a) Modulated lattice with alternating rows of bonds of variable strength. (b) Schematic illustration of the shift of the charges due to the modulation. This shift can be seen as a consequence of the introduction of a potential modulated by η. (c) Ground state of the modulated array with alternating columns of upward and downward dipoles. See text for a detailed description of the pictures.

To perform the analysis of the ground state configuration it suffices to consider a single plaquette, as shown in Fig. 6.3 (a), and to minimize its Hamiltonian with respect to the spins. In this way one obtains [82] that the cosine of the phase difference across the junctions with the same coupling constant are all equal and given by:

$$\cos\vartheta_{ij} = \frac{1}{2}\left(\frac{\eta+1}{\eta}\right)^{1/2} \quad \text{whereas} \quad \cos\widetilde{\vartheta}_{ij} = \frac{1}{2}\left(\frac{\eta+1}{\eta}\right)^{1/2}\left(\frac{2\eta-1}{\eta}\right) \tag{6.3}$$

gives the phase difference for the modulated " antiferromagnetic " bond. Since $|\cos\vartheta|$ never exceeds unity, Eq. (6.3) implies a lower critical value of $\eta = 1/3$. Below this value there is only one ground state configuration, the " ferromagnetic " one. At $\eta = 1/3$ there is a bifurcation of the " ferromagnetic " solution toward two solutions [84]. The origin of this degeneracy in this case is easily seen (see Fig. 6.3 (a) for the site s_i numbering): for any orientation of the spin representing the phase on the site s_2, there are two possible orientations for the spin on the site s_3 according to Eq. (6.3). Once the orientations of s_2 and s_3 are chosen, the orientation of the two remaining spins of sites 4 and 1 is determined. Thus, the ground-state is doubly degenerate for all $\eta > 1/3$. This model can thus be considered a generalization of the fully frustrated case. As long as the double degeneracy of the ground state exists one expects a transition of Ising type.

Similarly to the unmodulated case, it's useful to introduce the 2D Coulomb gas analogy to develop an intuitive picture. First, as rigorously derived in reference [83], the introduction of a modulated coupling constant results in a small displacement of the charges, as

schematically indicated in Fig. 6.3 (b). This can be seen as the result of the introduction of a potential $U(x, y)$ provided by the other junctions. This potential is modulated in the y direction because of the modulation of the E_J, leading to a shift of the charge positions from the center of the plaquettes towards the weak bonds. Then, if $|\eta - 1|$ increases, the charges get closer together on either side of the weak bonds. This results in the formation of dipoles, as shown in Fig. 6.3 (c).

Modulated array in the critical region

In the previous section we have seen that the introduction of modulated bonds results in the formation of dipoles between neighboring half-integer charges. To describe this system of dipoles in the critical region, it's convenient to represent the charge distribution with variables located at the centers of the weak bonds. One thus associates with each weak bond a net charge m_{wb}, average of the two half-integer charges next to it, and a dipole moment $\vec{p}_{wb}$ formed by these two charges. With this definition, in the ground state, all $m_{wb} = 0$ and all dipoles along a column point in the same direction but alternate along each row.

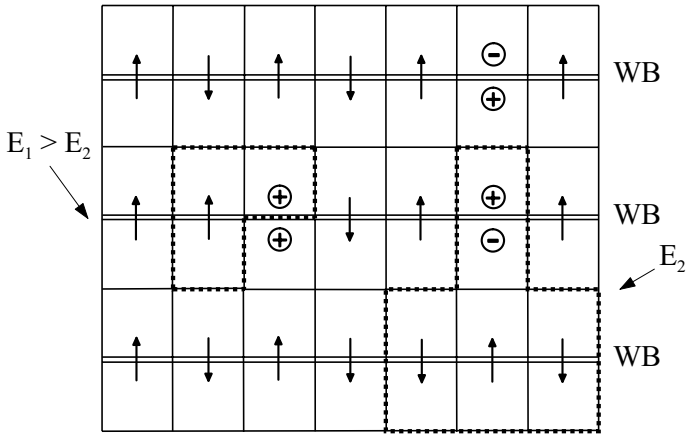

Figure 6.4: Domains of the opposite chirality in the ordered phase of a modulated array. The weak bonds are represented by double lines and domain walls by broken lines. The presence of dipoles increases the energy E_1 of a domain wall along weak bonds. Domain walls will therefore preferentially run along strong bonds.

In the picture of shifted charges, a domain wall separates adjacent plaquettes carrying charges of the same sign, as shown in Fig. 6.4. Because the distance between two charges of the same sign situated around a strong bond is larger, it's energetically more favorable for a wall to run along strong bonds than along weak bonds. When $|\eta - 1|$ is not too small, there is then a substantial energy difference between the two types of domain walls [83].

In the representation with the variables m_{wb} and $\vec{p}_{wb}$, the presence of a wall along a strong bond simply represents a change in the polarization, a flipped dipole. On the other hand, a wall running along a weak bond will alters the charges m_{wb}: every time a wall

starts or stops running along a weak bond, it produces half-integer fractional charges. In the critical region large domains will appear. However, since wall portions along weak bonds cost more energy per unit length, the domain walls will contain only short portions along weak bonds. The fractional charges will therefore be confined and combine to integer charges, contrary to the scenario presented for the unmodulated array. We now have the following picture in the critical region for the modulated array:

- the domain walls run mainly along strong bonds, and represent flipping dipoles formed of neighboring charges. The proliferation of these domain walls in the critical region will cause an Ising-like transition in this system of dipoles. We will see in section 6.1.4 that the flipping of these dipoles at the transition does not result in a susceptibility which diverges at the critical point. This explains why for $\eta \neq 1$ the BKT-transition can occur in the Ising-disordered phase;
- pairs of charges of the same sign, which are not bound in dipoles, combine to form a dilute gas of integer charges. The transition of this gas is a normal BKT-transition and is not triggered by the Ising transition.

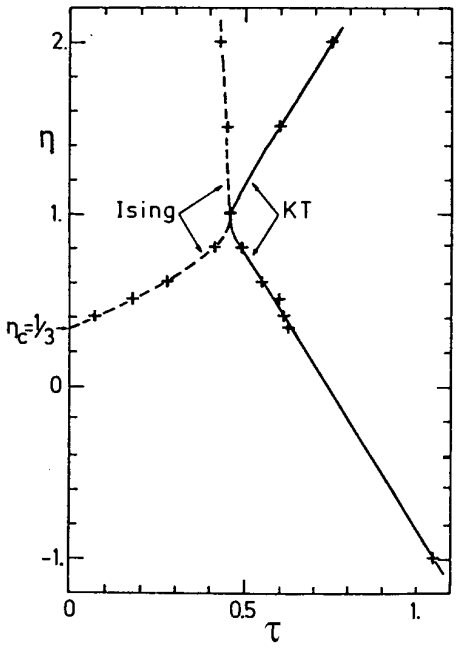

Figure 6.5: Phase diagram τ, η determined with Monte Carlo simulations [82] on a lattice with bond strength η as a function of the reduced temperature τ. The low-temperature transition is of Ising-type and the high-temperature one corresponds to a BKT-type transition. In the vicinity of $\eta = 1$ the phase diagram has only qualitative validity.

This scenario was checked by performing analytical calculations [84] and with Monte Carlo simulations [82, 83, 86, 85]. All these theoretical studies confirm the previous

predictions, and show two transition temperatures for a given value of η. They show a sudden proliferation of domain-walls at the low temperature transition, and a complete disappearance of the phase order at a higher temperature. This supports the conjecture that for $\eta \neq 1$ the low temperature transition is an Ising-like transition, while the high-temperature one is of BKT-type. The (τ, η) phase diagram [82] is shown in Fig. 6.5. The low temperature dashed branch represents the Ising-type transition line, while the high temperature line represents the BKT-type transition. In the vicinity of $\eta = 1$ the precision of Monte Carlo simulations does not allow to resolve the two transitions, and the phase diagram should be read qualitatively in this region. The extrapolation of the phase diagram seems nevertheless to indicate that for $\eta = 1$ the critical behavior results of a merging of the two transitions.

Monte Carlo simulations [85, 83] and analytical calculations [84] also allow to extract the static helicity modulus, which can be directly related to the superfluid density measured in our experiment. The static helicity modulus computed in reference [83] will be compared to our measurements in section 6.2.3.

6.1.4 Phase dynamics in a modulated array

The aim of this section is to find how the quantitative description presented in section 6.1.3 can be compared with our experimental data. We will first describe the low temperature behavior of the modulated array in a region where fluctuations are negligible. Then we introduce the dielectric function of the system of dipoles near the Ising transition, and relate it to measured quantities.

Description at low temperatures

In this section we briefly describe the influence of the modulation parameter η on the array of junctions at $f = 0$ and $f = 1/2$ in a temperature region where thermal fluctuations may be neglected. This will allow to find the expressions for the parameters describing a single junction as a function of temperature.

Let us first consider a unit cell of the modulated array shown in Fig. 6.3 (a). Each junction is described in the framework of the RSJ model [14] with L_J and R_J representing the inductance and the resistance of the unmodulated junctions at $f = 0$ respectively. In the RSJ model the junction resistance R_{ij} and the junction inductance L_{ij} between sites i and j are connected in parallel. The critical supercurrent is $I_C^{ij} = \eta I_C$ for the modulated junctions, where I_C is the critical current of the unmodulated junctions. This determines L_{ij} through $L_{ij} = \hbar/(2eI_C^{ij} \cos \vartheta_{ij})$. This relation allows to find the inductances of the junctions provided we know the gauge invariant phase differences ϑ_{ij} at the different frustrations. For $f = 0$ we have $\cos \vartheta_{ij} = 1$, leading to $L_{ij} = L_J$ and $\widetilde{L_{ij}} = L_J/\eta$ for the unmodulated and modulated junctions respectively, as expected. In a similar way, for $f = 1/2$, the junction inductances are obtained with Eq. (6.3), leading for the

unmodulated and modulated junctions to:

$$L_{ij}^{-1} = L_J^{-1}\frac{1}{2}\left(\frac{\eta+1}{\eta}\right)^{1/2} \quad \text{and} \quad \widetilde{L}_{ij}^{-1} = L_J^{-1}\frac{1}{2}\left(\frac{\eta+1}{\eta}\right)^{1/2}(2\eta-1)\,. \tag{6.4}$$

The temperature dependence of the junction inductance is taken into account by using the de Gennes equation [17]. Because the length l of the junctions is modulated by Δl, this causes indirectly a temperature dependence of the modulation parameter, given by:

$$\eta(T) = \exp\left[\frac{\Delta l}{\xi_N(T_{cs})}\left(\frac{T}{T_{cs}}\right)^{1/2}\right], \tag{6.5}$$

where $\xi_N(T_{cs})$ is the coherence length of the Cooper pairs in the normal metal at the transition temperature T_{cs} of the superconducting islands. With this relationship, we have taken into account the temperature dependence of η in determining the reduced temperature parameter τ (section 4.4.2), because the variation of η in the relevant temperature range is not negligible. On the other hand, η can be considered approximately constant for phenomena appearing within small temperature intervals. We will therefore take η constant for the discussion of the phenomena appearing in small intervals around the Ising or the BKT transition.

The influence of the modulation parameter η on the junction resistance R_{ij} is simply taken into account through the length of the normal metal bridge constituting the junction. By describing this length by l and $l-\Delta l$ for the unmodulated and modulated junctions, we obtain that their resistances are given by $R_{ij} = R_J$ and $R_{ij} = R_J(1-\Delta l/l)$ respectively.

At temperatures well below the critical region, the normal channel of the junctions becomes negligible compared to the superfluid channel. Moreover, at low temperatures the thermal fluctuations of the phases can be neglected, allowing to model the array with the inductances L_{ij} only. It is then possible to find a relationship between the sheet conductance G extracted from the measurements at low temperature and the single junction inductance. To establish this link, notice first that in our two-coil mutual inductance measurements we do not select the response of the array in any particular direction, but we measure, rather, the average of the conductance over all possible angles in the plane of the lattice. Let us call z_1 and z_2 the impedances of the array in the modulated and unmodulated directions. From an experimental point of view, we can reasonably assume that the measured sheet impedance Z is associated with an average of z_1 and z_2, which can be estimated by using Eq. (3.3):

$$\frac{M(Z)}{M_{ss}} \approx \left[1+\frac{Z}{i\omega M_c}\right]^{-1} = \left[\left(1+\frac{z_1}{i\omega M_c}\right)\left(1+\frac{z_2}{i\omega M_c}\right)\right]^{-1/2}, \tag{6.6}$$

with $M_c \simeq 1.12\cdot 10^{-9}$ H. In the relevant temperature domain, the response is mainly inductive, and leads to ratios: $z_1/(i\omega M_c) \ll 1$ and $z_2/(i\omega M_c) \ll 1$. By developing the square roots in the right-hand side of Eq. (6.6), one finds $Z \simeq (z_1+z_2)/2$. This

indicates that, to take into account the anisotropic character of our modulated array, we have to associate the array impedance with the arithmetic mean of the modulated and unmodulated impedance. Because the unit cell has three unmodulated junctions of inductances L_J and one modulated junction of inductance L_J/η, the arithmetic mean leads to the conductance at $f = 0$:

$$G(f=0) = \frac{1}{4}\left[3+\eta\right]\frac{1}{i\omega L_J} \quad \text{, while} \quad G(f=1/2) = \frac{1}{4}\left[\frac{\eta+1}{\eta}\right]^{1/2}\frac{\eta+1}{i\omega L_J} \tag{6.7}$$

is obtained for $f = 1/2$ in a similar way, with Eq. (6.4). The measured sheet inductance $L_\square$ is related at low temperature to the sheet conductance by $G = 1/(i\omega L_\square(\tau))$, allowing to write for $f = 0$, with the use of the first part of Eq. (6.7) and the de Gennes equation:

$$L_\square^{-1}(\tau) = \frac{2e}{\hbar}\,\frac{3+\eta}{4}\,I_C(0)\left(1-\frac{T}{T_{cs}}\right)^2 e^{-|c|\sqrt{T}}. \tag{6.8}$$

This equation was used in section 4.4.2 to determine the critical current of the junctions, and to deduce the relationship between the real and the reduced temperature.

Description near the Ising transition

In this section we determine the part of the response due to the domain walls in a temperature region close to the reduced temperature τ_I of the Ising transition. We describe their influence through a dielectric function ϵ_I, related to the measured sheet inductance.

Let us consider the two-fluid model to describe the response of the array, where the medium is modeled by a dissipative channel in parallel with an inductive one. Because the normal currents flowing in the junctions are small compared to the superfluid current near τ_I, the contribution of the normal channel is almost completely suppressed. We will thus neglect the normal channel in the following. Quite generally, the presence of thermal fluctuations is taken into account by adding an impedance Z_{dw} in series with the superfluid channel. Near the Ising-like transition temperature, this impedance represents the contribution of domain walls. Equivalently, it is possible to describe their influence with a dielectric function ϵ_I, which renormalizes the superfluid background L_0 resulting from the second part of Eq. (6.7). The dielectric function ϵ_I takes globally into account the contribution of domain walls appearing in the modulated and unmodulated directions, and the response of the array is then described by the equivalent circuit shown schematically in Fig. 6.6.

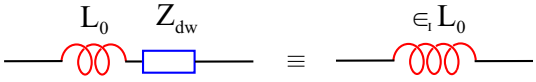

Figure 6.6: Equivalent circuit to describe the response of the array in the presence of domain walls. The renormalization of the superfluid channel L_0 due to these thermal excitations is taken into account by adding series impedance Z_{dw} or, equivalently, by the introduction of a dielectric function ϵ_I.

The measured quantity corresponding to the diagram of Fig. 6.6 is the sheet impedance $Z = R + i\omega L$ or, equivalently, the sheet conductance $G \equiv 1/Z \equiv (R_\Box)^{-1} + (i\omega L_\Box)^{-1}$. By introducing the dielectric function of the domain wall medium $\epsilon_I \equiv \epsilon_I' - i\epsilon_I''$ one obtains:

$$L = L_0 \epsilon_I' \quad \text{and} \quad R = \omega L_0 \epsilon_I'' \,, \tag{6.9}$$

where ϵ_I has different values for different orientations. We now establish an estimate of $\epsilon_I(\omega, \tau)$ by taking exclusively into account the response induced by the proliferation of the domain walls in the critical region. As far as the temperature is concerned, our analysis will only be valid in a region close to τ_I, and only as long as τ_I is small enough to be able to neglect the presence of bound pairs and free vortices. As noticed in the previous sections, in the Coulomb gas picture, the appearance of domain walls near τ_I will mainly lead to the flipping of dipoles. It is the flipping of these dipoles which induces a change in the dielectric function. It is possible to find a reasonable estimate of ϵ_I by considering the following remarks:

- the domain wall melting at τ_I only softens ϵ_I^{-1}, because the length of the dipoles is fixed by the modulation parameter η, which may be considered constant close to τ_I;

- as a result of the strong anisotropy of the modulated array, the dielectric function has two different values ϵ_{xx} and ϵ_{yy} in the x and y directions (see Fig. 6.3), related to ϵ_I by $\epsilon_I = \sqrt{\epsilon_{xx}\epsilon_{yy}}$. However, in first approximation, the presence of the dipoles will not affect the dielectric function in the x direction, we can therefore set $\epsilon_{xx} = 1$;

- in the quasistatic limit, ϵ_{yy} contains the susceptibility of a system with an Ising symmetry and is given by [83]:

$$\epsilon_{yy} = 1 + \pi^2 \frac{\eta^2}{|\eta + 1|} \chi_{I0}, \tag{6.10}$$

  where χ_{I0} is the " antiferromagnetic " susceptibility [87] of the Ising lattice. This quantity has no divergence at the Ising critical point, but shows a logarithmic anomaly of the type $t \ln|t|$ with $t \equiv 1 - \tau/\tau_I$ [83]. It has a vertical tangent at the critical temperature and rises to a maximum at a slightly higher temperature;

- a simple and intuitive approach to introduce the dynamical phenomena in the dipole system is to apply a Debye-like model, described by the following susceptibility:

$$\chi_{de}(\omega) = \frac{1}{i\omega t_{de} + \chi_{I0}^{-1}} \tag{6.11}$$

  where t_{de} is a short microscopic time associated with the dipole relaxation, and χ_{I0} the susceptibility in the static limit. At the frequencies of interest, $\omega t_{de} \ll \chi_{I0}^{-1}$, leading with Eq. (6.11) in first order to:

$$R \sim a_R (\omega t_{de})^2 \chi_{I0}^2 \quad \text{and} \quad L \sim L_0 (1 + a_L \chi_{I0}) \,, \tag{6.12}$$

where $a_R(\tau)$ and $a_L(\tau)$ are temperature dependent functions. The second part of Eq. (6.12) shows that, in the approximation $\omega t_{de} \ll \chi_{I0}^{-1}$, the inductive part of the response is not influenced by the dynamical approach to the system. For our relatively low measurement frequencies, it will therefore be reasonable to consider the inductance L in the quasistatic limit.

According to Eqs. (6.9) and (6.10) , the inverse of the dielectric function corresponds to the inverse sheet inductance L^{-1} as a function of temperature in the Ising-like critical region. For our measurements at the lowest frequency, we then expect, with increasing temperature, a softening of the inductive part of the response at $\tau = \tau_I$ due to the proliferation of domain walls. Because ϵ_I^{-1} remains non zero at temperatures slightly above τ_I, we also expect that L^{-1} does not vanish, but shows a plateau in a small temperature interval above τ_I.

The two components of ϵ_I can be related to the components of the static helicity modulus $\gamma = \sqrt{\gamma_x \gamma_y}$ in good approximation by $\gamma_x \sim \epsilon_{yy}^{-1}$ and $\gamma_y \sim \epsilon_{xx}^{-1}$ [83]. Even if the correspondence between ϵ_I and γ is not exact [83], they should exhibit the same kind of behavior, and γ should be characterized near τ_I by a $t \ln|t|$ anomaly (see Eq. (6.10)). Therefore, its temperature derivative at τ_I should show a $\ln|t|$ divergence.

So far we don't have a complete theoretical description of the dynamical phenomena appearing in the region of the Ising-like transition. We can nevertheless try to explain the behavior of the helicity modulus measured at non-zero frequencies by using a purely static approach and with the help of finite size scaling. Notice first that, in the Ising model, the logarithmic anomaly of the static helicity modulus γ is related to the size $\tilde{L}$ of the lattice by the differential relationship $(d/d\beta)[\beta\gamma]|_{max} \sim \ln|1 - \tau/\tau_c| \sim \ln \tilde{L}$, where $\beta \sim 1/\tau$, as confirmed by numerical simulations [83, 86]. Moreover, let us assume that measurements at frequency ω allow to detect phenomena occurring at length scale $\tilde{L}(\omega)$ obeying a power-law relation between $\tilde{L}$ and ω. One thus obtains a linear relationship between the maximum of the derivative of the helicity modulus and the logarithm of the frequency: $(d/d\tau)\gamma|_{max} \sim -\ln \omega$.

6.2 Results and discussion

6.2.1 Introduction

In this section we present the data collected with the use of the two-coil mutual inductance technique on a modulated array. We deduced from our measurements performed at frustrations $f = 0$ and $f = 1/2$ the sheet conductance of the sample $G = 1/R_\square + 1/(i\omega L_\square)$ or, equivalently, the impedance $Z = R + i\omega L$ in a frequency range between 0.23 Hz and 20 kHz for temperatures between 2 K and 8 K.

Section 6.2.2 is devoted to the discussion of the curves measured at $f = 0$. They allow to compare the transition of an unfrustrated modulated array with the transition of a regular array at $f = 0$ and to deduce the value of the modulation parameter.

We next discuss the data collected at full frustration in two steps. First we focus on the measurements performed at the lowest frequency, 0.23 Hz, which can be associated in good approximation to the static response of the sample. Because the resistive component of the response is still not well understood, we mainly comment the inductive part of the response at the beginning. We discuss the dissipative phenomena and the frequency related effects in a second step.

6.2.2 Measurements at $f = 0$

The normalized inductive part of the curves measured at $f = 0$ as a function of the reduced temperature τ is shown in Fig. 6.7 for different frequencies. More precisely, the dynamical helicity modulus $\Gamma(\omega, \tau)$, defined as $\Gamma = L^{-1}/L_J^{-1}$ where $L^{-1}(\omega, \tau)$ is the inverse inductance of the array and $L_J^{-1}(\tau)$ the inverse inductance of a single junction, is plotted as a function of τ. The helicity modulus takes into account the collective stiffness of the array without considerations for the individual properties of the junctions (division by L_J^{-1}). These curves were measured at three different frequencies ranging from 0.23 Hz to 2 kHz. The dashed line represents the universal prediction [27] for the jump of the static helicity modulus at the BKT transition.

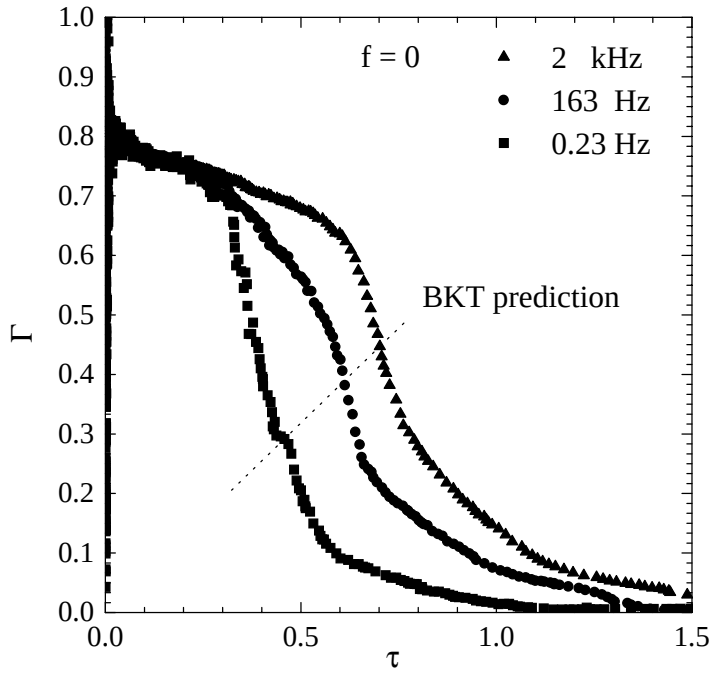

Figure 6.7: Dynamical helicity modulus Γ at $f = 0$ for three different frequencies as a function of the reduced temperature τ. The dashed line predicts the locus of the jump describing the BKT transition. Notice that at the lowest frequency the jump is steep and appears in the vicinity of $\tau = 0.4$.

The three curves show qualitatively the same behavior with increasing temperature. They start out together at low τ with an only slightly temperature dependent strait line. Then, with temperature increasing above $\tau = 0.3$, they separate and fall independently to zero. The drop is steeper and appears at lower reduced temperatures at lower frequency.

Let us now focus on the measurement performed at 0.23 Hz. As a consequence of the very low frequency used to acquire this curve, we expect that it is well described by the static helicity modulus. The measurement gives a straight line roughly temperature independent for $\tau \leq 0.3$, thereby indicating that the thermal excitations (vortex-antivortex) are negligible for reduced temperatures $\tau \leq 0.3$. In this region, the value of Γ is therefore mainly fixed by the ground state of the array, which dependents on the modulation parameter η, as explained in section 6.1.4. Following the first part of Eq. (6.7), the value of the helicity modulus of our modulated array for $\tau \leq 0.3$ is given by that of a regular array, reduced by a factor $(3 + \eta)/4$. By introducing a modulation parameter $\eta = 0.4$ in this expression, one obtains a value of Γ equal to 0.85 for our modulated array at low temperature, smaller than the value 1 relevant for an unmodulated square array.

Increasing the temperature above $\tau = 0.3$, the helicity modulus measured at 0.23 Hz exhibits a rapid decrease to zero. In the BKT scenario of the transition, this disappearance of the collective stiffness constant of the array is due to the dissociation of vortex-antivortex pairs. For an ideal (i.e. infinite and with all coupling constants exactly equal), unmodulated square array at $f = 0$, the BKT prediction for the transition temperature is given by $\tau_{BKT}(\eta = -1) \simeq 0.92$. This prediction is also valid for our modulated array if we take into account the lowering of the " bare " sheet inductance caused by the modulation. This can be achieved by remembering Eq. (6.7), which leads to the BKT temperature prediction $\tau_{BKT}(\eta = 0.4) \simeq 0.78$ for our modulated array. As shown in Fig. 6.7 this prediction is a factor of two larger than the measured value at 0.23 Hz which is approximately 0.4. We can evoke two reasons for this discrepancy: first, as observed in Ref. [61], it is difficult to obtain a frustration exactly equal to zero due to experimental limitations, and a few field induced vortices remain in the lattice. As shown in Ref. [61], the presence of these vortices leads to a premature jump of the helicity modulus, and therefore to a bad estimate of the temperature transition. The other reason is a possible disorder in the coupling constant of the junctions which could also reduce the measured transition temperature.

6.2.3 Measurements at $f = 1/2$

Quasistatic response as a function of temperature

Let us first examine the data collected at the lowest measurement frequency, which we associate in first approximation with the static response of the sample. The inverse of the sheet impedance $L^{-1}(T)$ and the resistance $R(T)$ are shown in logarithmic scales as a function of the real temperature T in Fig. 6.8. These measurements were taken at full frustration ($f = 1/2$) with a frequency of 0.23 Hz.

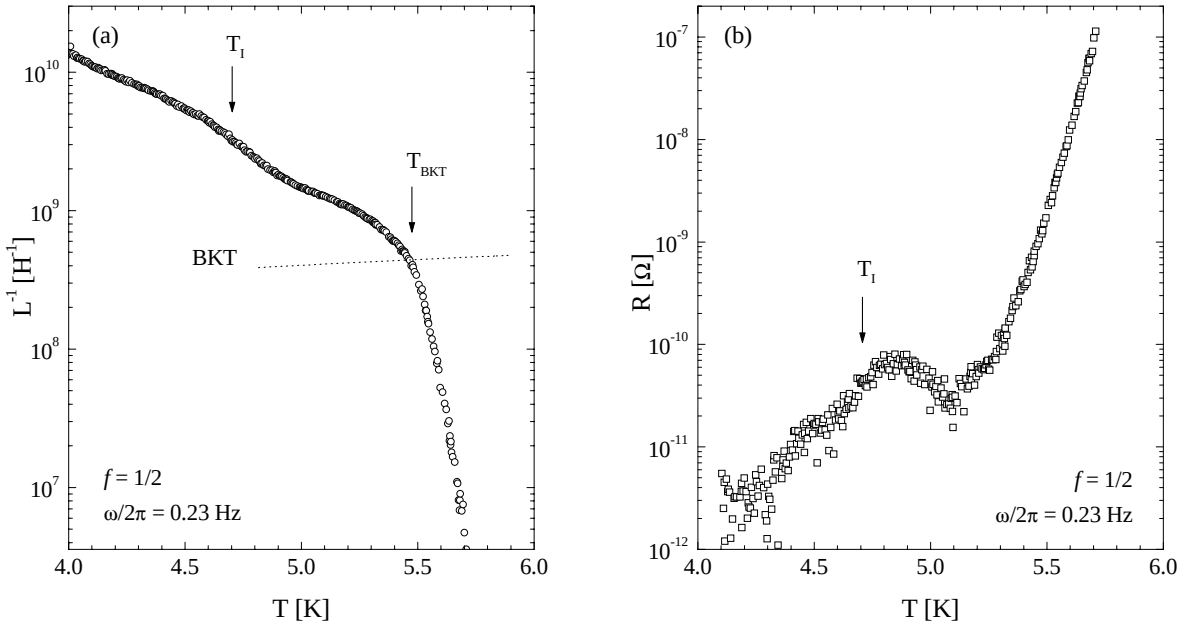

Figure 6.8: (a) Inverse kinetic inductance of the array at full frustration measured at 0.23 Hz as a function of the real temperature T. The dashed line predicts the locus of the jump describing the BKT transition. The low temperature transition at $T_I \approx 4.7$ K is associated with the Ising transition, whereas the jump at $T_{BKT} \approx 5.5$ K is the signature of the BKT transition. (b) Resistance of the array at $f = 1/2$ measured at a drive frequency $\omega/(2\pi) = 0.23$ Hz. Notice the appearance of a dissipative peak at a temperature close to T_I, followed by a rapid increase of dissipation at higher temperatures.

The quantity $L^{-1}(T)$ provides a direct probe of the superfluid density and, therefore, of the degree of phase coherence in the system. It exhibits two distinct features in the critical region:

- with increasing temperature, the curve presents first a softening at a temperature $T_I \approx 4.7$ K, revealing an anomaly in the superfluid density. This depression indicates a lowering of the phase coherence in the system, which keeps nevertheless a non-zero value at higher temperatures (4.9 K $\leq T \leq$ 5.3 K). This first transition at T_I leads therefore to a system which is only partially disordered. As discussed in section 6.1.3, it is then very probable that this is the result of the proliferation of Ising-type critical fluctuations, which consist of domains of opposite chirality within the ordered phase. This temperature is therefore associated with the Ising transition;

- at a higher temperature $T_{BKT} \approx 5.5$ K, the inverse of the sheet inductance falls abruptly to zero, indicating a complete disappearance of the superfluid density. This phenomenon occurs at a temperature which corresponds to the intersection between

the measured curve and the universal BKT prediction represented by a dashed line in Fig. 6.8 (a). It is therefore reasonable to link this loss of phase coherence with the BKT transition, and to associate T_{BKT} with the unbinding of the vortex pairs.

The resistive part of the response measured at full frustration with a drive frequency of 0.23 Hz is shown in Fig. 6.8 (b). For this frequency, the sensitivity of our measurement setup allows to probe the array resistance only for temperatures higher than 4.2 K. Increasing the temperature above 4.2 K, the resistance grows first by about a decade. This initial rise ends in a rounded peak, with a maximum at about 4.85 K. At higher temperatures the resistance decreases first slowly (4.9 K $\leq T \leq$ 5.2 K), before it shows again a rapid raise. One can explain qualitatively the shape of the resistive curve by considering the phenomena which described the behavior of the superfluid density. The dissipative peak appears indeed at a temperature very close to T_I, and it is therefore likely that the presence of this peak is the result of an Ising-like transition, although the increase of dissipation observed at temperatures higher than 5.3 K is associated with the BKT transition.

The " antiferromagnetic " susceptibility of the plane square Ising lattice was investigated on the basis of the exact series expansions [87], where it was found that the susceptibility of such a system has a vertical tangent at the critical temperature, and rises to a maximum at a somewhat higher temperature T_{max}. For the resistive curve shown in Fig. 6.8 (b), such a difference between T_{max} and T_I would result in locating the critical temperature of the Ising-like transition below the maximum of the dissipative curve. According to reference [87] this feature could be directly associated with the two-dimensional nature of the lattice.

To my knowledge, the data shown in Fig. 6.8 supply for the first time an experimental confirmation of the presence of two distinct transitions for modulated arrays at full frustration. These curves were acquired at a very low measurement frequency, and can therefore be compared in good approximation with the static approach developed in section 6.1.3. As predicted by this theory, we notice experimentally that the modulation of the coupling energy of the junctions in one direction leads, by increasing the temperature, first to the appearance of an Ising-type transition which is followed by a BKT-type transition. Although these two transitions are separated enough to be distinctly observed, we notice that the depression in the superfluid density induced by the Ising transition is very weak. It remains therefore difficult to be experimentally observed, and the use of low frequencies proved to be very useful because it allowed to achieve a high experimental resolution.

The different character of the two transitions is strikingly revealed by the shape of the curves shown in Fig. 6.8. One notices indeed that the Ising transition produces a structure in the superfluid density, or in the resistive part, of amplitude much smaller than the BKT transition. This can be qualitatively explained with the help of the scenario presented in section 6.1.3. We have seen in this approach that the Ising transition can be described with the help of a system of flipping dipoles, leading to a susceptibility which does not diverge at the critical point T_I, contrary to the behavior of the BKT transition. It is thus understandable that the signature of the Ising transition around T_I is more smooth than

the signature of BKT transition, which is accompanied by a complete disappearance of phase order.

Inductive part of the response as a function of τ

The inverse of the inductive part of the response, L^{-1}, normalized by the inverse inductance of a single junction L_J^{-1} is shown in Fig. 6.9 (a) as a function of the reduced temperature τ for several frequencies. These curves provide the dynamical helicity modulus $\Gamma(f = 1/2) = L^{-1}(f = 1/2)/L_J^{-1}$ at full frustration for three different frequencies. The dashed line represents the universal prediction for the jump of the static helicity modulus at the BKT transition. In Fig. 6.9 (b) we plotted the helicity modulus in the modulated and unmodulated directions, as computed with Monte Carlo simulations [83].

With decreasing temperature, for τ smaller than 0.02, the three curves shown in Fig. 6.9 (a) increase to the value of Γ measured in zero magnetic field. This behavior is probably due to the screening of the external magnetic field by a local field, produced by screening currents flowing in each plaquette of the array [47]. At temperatures τ smaller than 0.02, the frustration is therefore no more proportional to the applied field and the frustration of the curves shown in Fig. 6.9 (a) is different from 1/2.

For reduced temperatures higher than $\tau = 0.02$, the three curves present a similar general trend with increasing temperature:

- first, for $0.02 \lesssim \tau \lesssim 0.06$, one observes the presence of a plateau common to the three curves at $\Gamma \simeq 0.45$. The inductive response of the array is therefore independent of the measurement frequency for reduced temperatures smaller than $\tau \simeq 0.06$. Moreover, the temperature independence of Γ indicates that thermal excitations are negligible in this temperature range. For $\tau \leq 0.06$, the value of Γ is therefore mainly fixed by the ground state of the array, which depends on the modulation parameter η, as explained in section 6.1.4. Following the second part of Eq. (6.7), the value of Γ of our modulated array for $\tau \leq 0.06$ is depressed where compared to Γ of a regular array. By introducing a modulation parameter $\eta = 0.4$ in the second part of Eq. (6.7), one obtains a theoretical value $\Gamma = 0.65$ at full frustration at low temperature, smaller than $1/\sqrt{2}$, the value relevant for an unmodulated square array. Our experimental value $\Gamma \simeq 0.45$ at low temperature is thus a little bit a too small compared with $\Gamma = 0.65$ predicted by theory;

- for $\tau > 0.06$ the curves separate, and the response becomes frequency dependent. For temperatures $0.06 \lesssim \tau \lesssim 0.13$, the curves exhibit a decrease, which is steeper and leads to lower values at the lower frequencies. If this first reduction of the collective stiffness of the array is associated with an Ising-type transition, its behavior appears to be strongly frequency dependent;

- next, the curves stabilize at plateaus of non-zero amplitudes. In the scenario of the Ising-type transition discussed in section 6.1.3, we have seen that the dissipation is produced by flipping dipoles, and that it saturates at a non-zero value. Following this theoretical interpretation, one thus expects the levels of the plateaus to be the

same for all frequencies. By observing the data of Fig. 6.9 (a), one see that this prediction is in disagreement with the experimental curves, which show a frequency dependence of the plateaus levels. We have found no explanations to this fact until now;

- by increasing the temperature beyond the plateaus, the helicity modulus drops to zero; this corresponds to a complete disappearance of the phase order. In the scenario discussed in section 6.1.4, this feature is associated with the BKT transition.

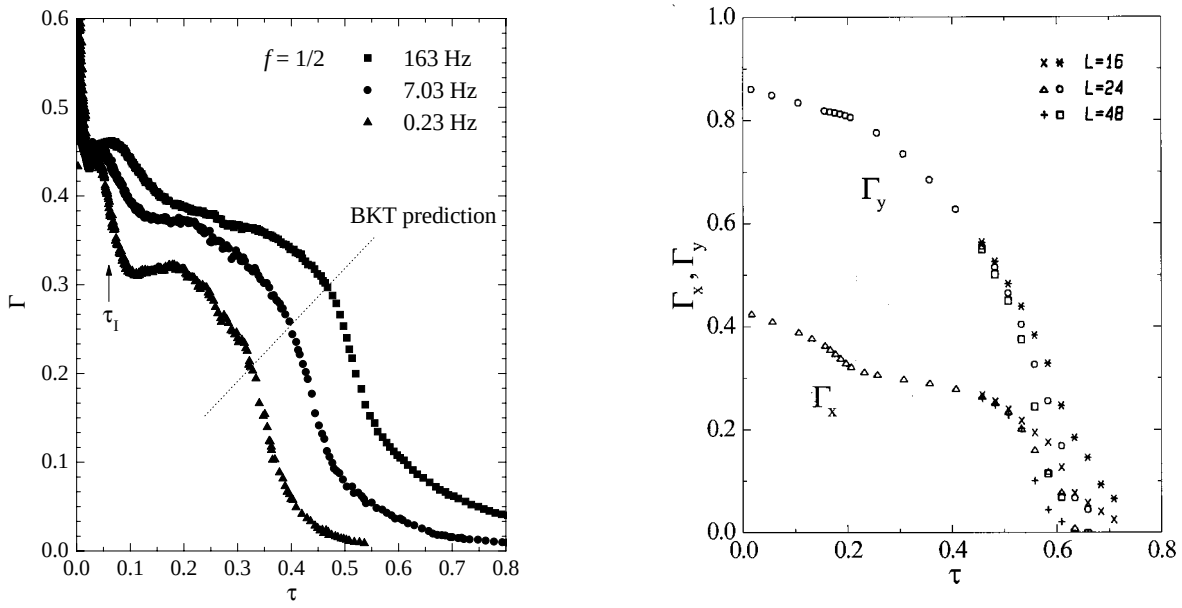

Figure 6.9: Dynamical helicity modulus Γ measured at $f = 1/2$ for three different frequencies as a function of the reduced temperature τ. The dashed line predicts the locus of the jump describing the BKT transition. For each curve and with increasing temperature, one notices first a decrease of the collective stiffness of the array around a temperature τ_I, which is followed at higher temperatures by a complete disappearance of the phase order. (b) Helicity modulus in x and y directions for $\eta = 0.5$ and for different lattices, computed with Monte Carlo simulations [83].

As mentioned above, we do not have at the moment an explanation describing the evolution of the measurements in the region of the Ising transition as a function of driving frequency. Moreover, a comparison, even qualitative, with the theoretical simulations is not easy; our measurements give indeed a mixing of the components of the helicity modulus in the modulated and unmodulated directions, while the theoretical simulations take generally into account the two components separately. As discussed in section 6.1.4, the helicity modulus measured at low frequency (0.23 Hz) approaches a static quantity, and can be compared with the results of Monte-Carlo simulations shown in Fig. 6.9 (b) in

good approximation. These simulations show the static helicity modulus in the modulated (x) and unmodulated (y) directions for arrays of several sizes with a modulation parameter $\eta = 0.5$ slightly larger than the η of our lattice. One notices first that in Monte-Carlo simulations only Γ_x is depressed by the Ising transition, which appears as a small kink around $\tau \simeq 0.15$. Although this curve can not be directly compared to our measurements, one notices that it shows a similar general trend as a function of temperature.

By plotting the helicity modulus at full frustration as a function of the reduced temperature τ, it is possible to check the locus of the transitions with the theoretical prediction shown in Fig. 6.5. For a modulation $\eta = 0.4$, this diagram indicates that the Ising transition appears at $\tau_I^{MC} \simeq 0.07$, while the BKT transition is expected at $\tau_{BKT}^{MC} \simeq 0.61$. These predictions can be compared with our experimental values which are for the Ising and BKT transitions, at $\tau_I^{exp} \simeq 0.06$ and $\tau_{BKT}^{exp} \simeq 0.33$ respectively. Thus, one notices that the experimentally observed transitions appear at lower values than the theoretical predictions, and that the loci of τ_I^{MC} and τ_I^{exp} are close. One can imagine two possible explanations for these deviations: first, one can think of a bad estimate of the reduced temperature τ; a second possible explanation is a small detuning of the external magnetic field.

Derivative of the helicity modulus

To visualize the evolution of $\Gamma(f = 1/2)$ for different ω, we calculated numerically, at each measurement frequency, the first derivative of the dynamical helicity modulus with respect to reduced temperature in the region of the Ising-like transition. By plotting these curves as a function of τ, one obtains the data shown in Fig. 6.10 (a). Each of the four curves shown possesses a maximum, which can be associated with an effective transition temperature τ_ω, different for each measurement frequency.

Let us first notice that the curves shown in Fig. 6.10 (a) possess peaks well marked and better defined at the low frequencies, while they subside and become wider with increasing frequency. It thus seems that the temperature range in which the fluctuations associated with the Ising transition are apparent becomes wider with increasing frequency. The same observation can also be made in Fig. 6.9 (a).

The curves shown in Fig. 6.10 (a) show that the effective transition temperature τ_ω associated with each frequency shifts to higher temperatures with increasing frequency. One indeed notices that τ_w is about 0.06 for 0.23 Hz, and increases to 0.11 for 163 Hz. We tried to describe this behavior with a Debye-like model (see section 6.1.4), which takes into account the dissipation induced by the dipoles, but it appears that it is not possible to explain the pronounced shift of τ_ω in this way. The observed frequency dependence remains thus unexplained.

The curves of Fig. 6.10 (a) were obtained with the normalized inductance of the array, plotted as a function of τ. Because τ is itself a function of temperature T, one could think that the shift of τ_ω as a function of ω is simply due to a bad numerical data analysis. To check the curves shown in Fig. 6.10 (a), we therefore examined directly the behavior of the unrenormalized inductance of the array measured at several frequencies. There too

we noticed a strong displacement as a function of frequency. It seems therefore that the curves shown Fig. 6.10 (a) retain their full validity.

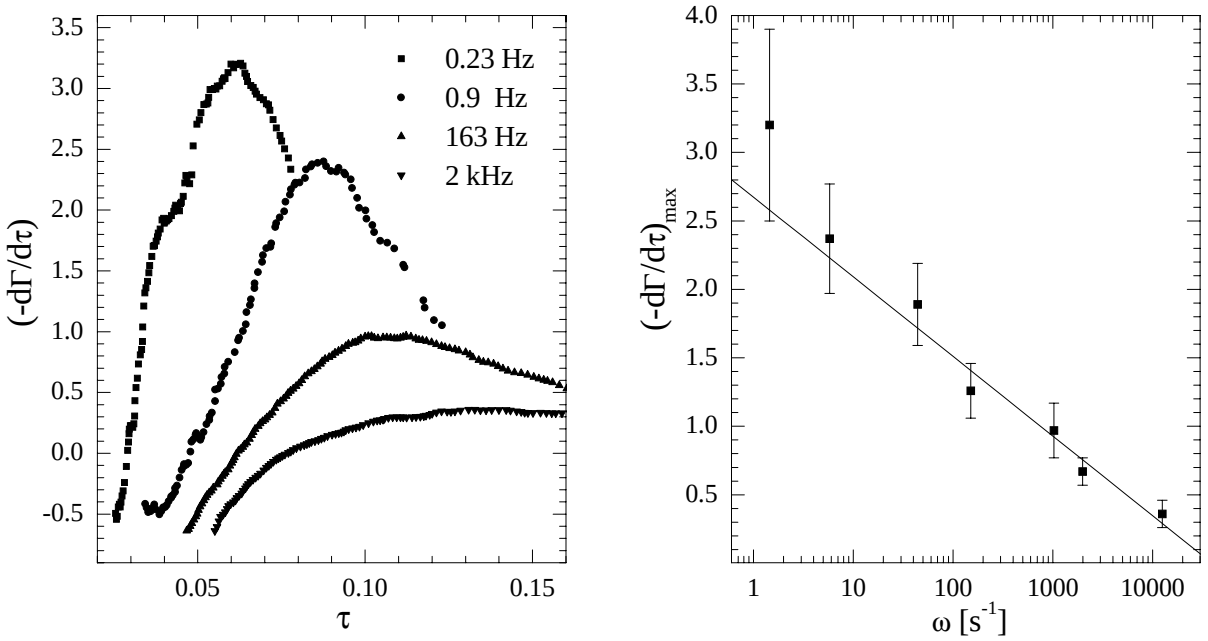

Figure 6.10: (a) Derivatives of the dynamical helicity modulus plotted as a function of τ, for several measurement frequencies. Notice the shift of the maxima as a function of τ. (b) Maxima of the curves shown in the previous figure plotted as a function of the measurement frequency in lin-log scales.

We can try to compare the data of Fig. 6.10 (a) with Monte Carlo simulations by adopting the purely static approach presented in the last paragraph of section 6.1.4. Assuming that each frequency ω allows to detect phenomena occurring in area $L^2(\omega)$, and that there is a power-law relationship between L and ω, we obtain a linear relationship between the maximum of $d\Gamma/d\tau$ and the logarithm of the frequency. This relationship follows directly from the logarithmic anomaly in the helicity modulus, it is thus a signature of the presence of an Ising-like transition. We plotted in Fig. 6.10 (b) the values of the maximum of the $d\Gamma/d\tau$ curves, deduced from our measurements, as a function of frequency in a lin-log representation. The error bars are an estimate of the uncertainty caused by the numerical procedure used to find the curves of Fig. 6.10 (a). The result obtained in this way fall on a straight line, as one notices in Fig. 6.10 (b). Nevertheless, we should be cautious about the conclusions which can be drawn from this figure. The anisotropic character of the array leads to helicity moduli which are different in the modulated and unmodulated directions, as shown in Fig. 6.9 (b). Monte-Carlo simulations provide these two components separately. Discussions about the Ising transition based on Monte-Carlo calculations relate therefore to only one Γ component. On the other hand, it is not possible to separate the Γ components with our measurement technique, and we have to consider

the measured signal as resulting from components in the modulated and unmodulated directions. Strictly speaking, the linear behavior of the data observed in Fig. 6.10 (b) does therefore not constitute a final proof of the Ising-like character of the transition.

To conclude this discussion, let us notice that it is reasonable to postulate that only one component of the measured signal is affected by the flipping of the dipoles related with the Ising transition. By considering the other component an effective constant background, figure 6.10 (b) regains its complete validity.

Resistive part of the response

The resistive part of the impedance of the array measured at full frustration as a function of the real temperature and for several driving frequencies is shown in Fig. 6.11. As mentioned above, the sensitivity of our measurement system does not allow to measure the resistance of the array at temperatures smaller than about $4.2K$.

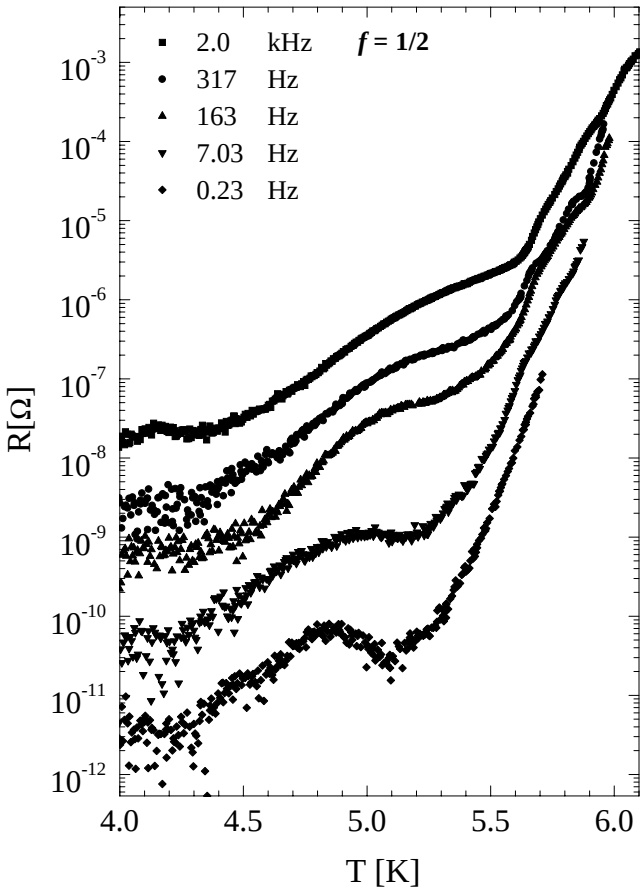

Figure 6.11: Resistance of the array measured at several frequencies at full frustration, as a function of the real temperature. Notice the appearance of a peak for the lowest frequencies, which is related to the Ising-like transition.

The resistive curves show qualitatively the same shape at all the measurement frequencies. With increasing temperature one first notices an increase of the resistance, leading to the appearance of a structure in the shape of a rounded peak. This structure seems to be less marked and wider at the high frequencies, and shifts to higher temperatures with increasing ω. At higher temperatures, each curve exhibits a rapid rise of the resistance, which finally approaches the normal state sample resistance.

A more detailed discussion of the data shown in Fig. 6.11 would be based on a theory including the evolution of the resistance as a function of frequency. As mentioned in section 6.1.4, we included the dynamical aspects with a Debye-like model, leading to the resistance predicted by Eq. (6.12). Unfortunately, even if the peak associated with the Ising transition at the lowest frequency could be described by this model, we notice that important features of the curves shown in Fig. 6.11 do not correspond to the prediction. In particular, the frequency dependence of the curves is in disagreement with the ω^2 dependence predicted by the first part of Eq. (6.12). To gain more insight in the dynamics of this system of dipoles, it would thus be interesting to probe the response directly as a function of the measurement frequency, in a way similar to what we did for the percolative array. In this manner it would be possible to achieve a more complete understanding of the phenomena occurring in the critical region of the Ising transition.

Chapter 7

Conclusions

In the present work we studied JJAs patterned into non-conventional geometries. The first stage was devoted to the fabrication process and the characterization of the geometrical parameters defining the arrays. We have then probed their response to a small ac electromagnetic field with the help of a two coil mutual inductance technique. This measurement method, combined with the use of a SQUID, allowed to achieve a high experimental resolution. Moreover, because the feedback response provided by the SQUID is approximately independent of the measurement frequency, it was possible to sweep the drive frequency over a wide range during the data acquisition, and so to take fully advantage of the intrinsically dynamic character of the inductive measurement method.

Percolative array

The dynamical response of the disordered array was measured as a function of temperature and excitation frequency for several values of frustration. The interpretation of these experimental results makes the following points stand out:

- the asymptotic corrections to the array inductance measured in the limit of small frustrations show a behavior peculiar to the disordered geometry of the lattice, in a temperature region below the critical temperature. The comparison with the theoretical approach, based on the hierarchical blob and bond model, confirms experimentally the scale invariance characteristic to the fractal structures. The small discrepancy between the predicted and the measured curves is probably due to thermal fluctuations, whose presence was neglected in the theory.

- at temperatures close to the critical region, the measurements of the sheet conductance are interpreted through an impedance Z_v of the vortex medium. The curves acquired as a function of frequency and at zero frustration reveal that the real and imaginary components of Z_v behave as power-laws, with temperature dependent exponents $u(\tau)$. This property was interpreted in the framework of a dynamical theory involving vortex bound pairs of sizes larger or equal to the correlation length ξ_p. The two-dimensional character of this approach is associated with a regular array of lattice constant ξ_p.

The exponent $u(\tau)$ shows experimentally a temperature dependence which is weaker than predicted by theory. Because the dynamics of the system is a complicated phenomenon to describe, it is difficult to reach definite conclusions about the reason for this disagreement.

- in a temperature region well above the critical temperature, the relevant excitations are single vortices moving in the pinning potential due to the array of junctions. The thermally activated behavior of these excitations is described by taking into account a regular 2D array of lattice constant ξ_p, which provides a barrier energy equal to twice the Josephson coupling energy.

Modulated array

We measured the response of modulated arrays at fixed frequencies at temperatures close to the critical region, at zero and full frustrations. With increasing temperature, the measurements at full frustration show first a weak depression in the superfluid density, accompanied by a dissipative peak in the resistive part of the response. One next notices, at a higher temperature, a rapid rise of the resistance and a complete disappearance of the superfluid density. A qualitative comparison of these experimental data with the theoretical predictions shows that it is possible to associate these features with two distinct transitions: one appearing at a lower temperature with an Ising character, followed by a BKT-type transition. The measurements have in this way indirectly revealed the presence of two kinds of excitations in the critical region for fully frustrated square arrays: on the one hand vortex excitations, related to the BKT transition, and on the other hand linear defects due to the appearance of domains of opposite chirality in the ordered phase which lead to the Ising-like transition.

A detailed comparison of our data with theory appeared to be difficult for several reasons. First, notice that our measurement technique probes the mean response of the lattice along the modulated and unmodulated directions, contrary to the theory which takes separately into account these two components. Moreover, the modulation parameter $\eta(T)$ is difficult to estimate accurately and depends on temperature, contrary to the studies performed theoretically. Finally, the evolution of the measured curves as a function of frequency in the regime of the Ising-like transition has not been explained until now. An additional study allowing to probe the response of the sample directly as a function of frequency, while frustration and temperature are kept constant, should establish more precisely the link with theory.

Finally, let us emphasize that the study of square modulated arrays required a particular effort for the fabrication of the samples, to obtain the same modulation of the coupling constants on the whole area of the lattice. Moreover, we noticed that the response of the array is very sensitive to the frustration. To obtain reproducible measurements at full frustration, we had therefore to adjust carefully the external magnetic field before each acquisition.

Acknowledgments

First I would like to thank my thesis advisor Prof. P. Martinoli who gave me the opportunity and the necessary means to carry out this work in his research group. I deeply appreciated his invaluable support to work out the theoretical approaches applied in this document, and the freedom he let me to choose the orientation of my research activities.

Experimentally speaking, this work would not have been possible without the experience of Dr. Ch. Leemann, who I am greatly indebted to both for his valuable suggestions and for his friendship throughout these four years. I wish also to express my deep gratitude to Dr. S. Korshunov, who made several trips from the Landau Institute of Moscow to establish the theoretical concepts used to explain our measurements. His frequent stays in Neuchâtel allow fruitful discussions to interpret the experimental results, and to spend some nice moments.

I wish also to warmly thank Dr. A.-L. Eichenberger, who guided with humor and good mood my first steps in the domains of the fabrication techniques and of the characterization of the arrays. A part of the experimental work was performed in collaboration with C. Jornod and S. Rossé during their diploma stage. The work in our team was efficient and enriching, and I would like to thank them especially.

I am thankful to Prof. H. Beck, B. Pannetier and C. Schönenberger for having accepted to be examiners for this Ph.D. thesis.

The establishing of the experimental setup would not have been possible without the help and the know-how of the technical staff of the electronics and mechanics workshops. I will keep good memories of their collaboration, which has been essential all along this work.

Finally, I wish to express my gratitude to my friends and coworkers for the nice moments spent together; they all contributed, to some extent, to this work: Michel, Jöel, Peter, Loïc, Alain, Mauro, Riccardo, Silvia, Bertrand, Stéphane, Gombo, ...

Appendix I: schema of the cryostat

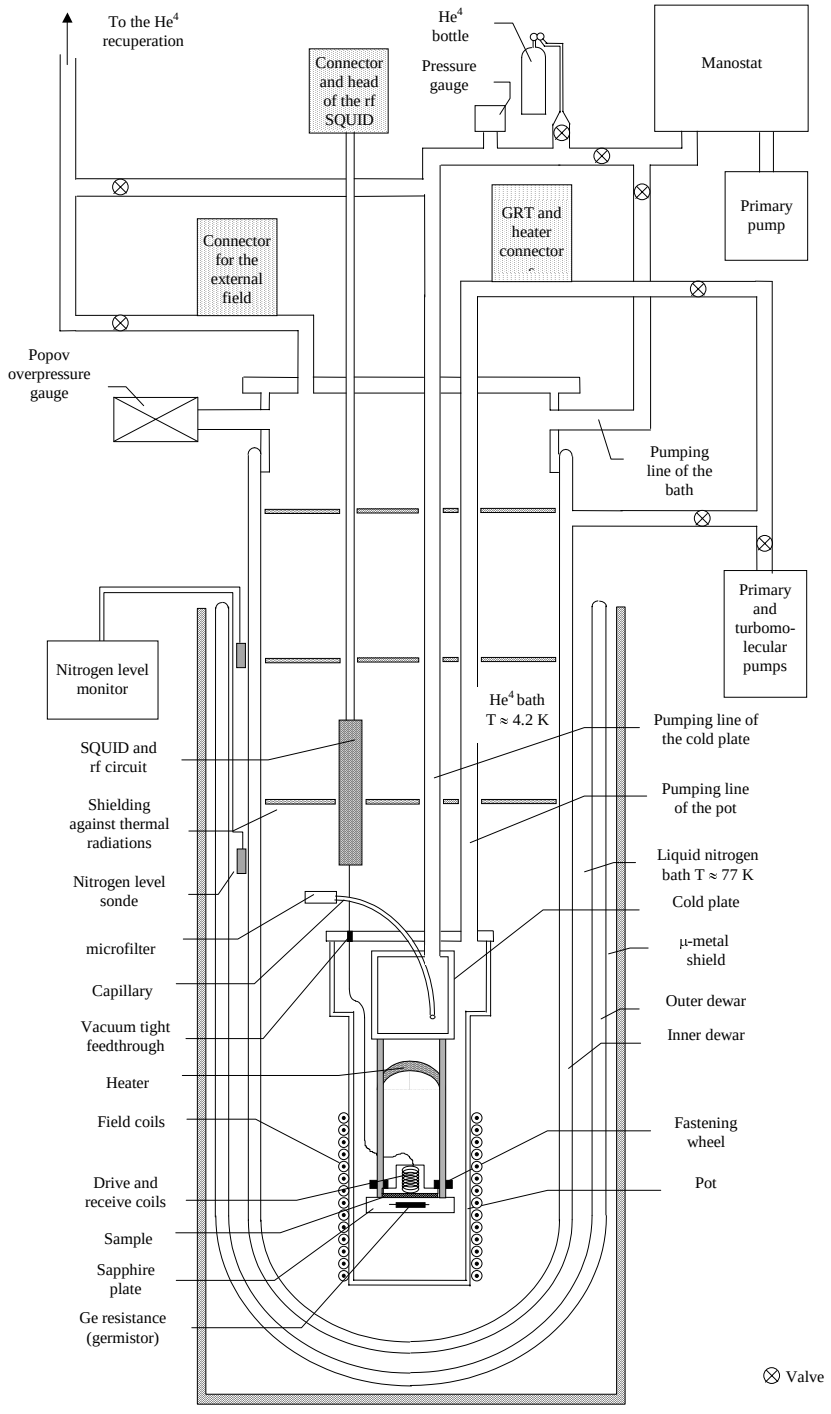

Figure 7.1: Schematic view of the insert and of the dewar.

Bibliography

[1] For a general review, see for example: R. S. Newrock, C. J. Lobb, U. Geigenmüller and M. Octavio, *preprint*.

[2] For a general review, see for example: P. Martinoli and C. Leemann, *J. Low Temp. Phys. 118*, 699 (2000).

[3] A. Bunde and S. Havlin, *Fractal and Disordered Systems*, Springer-Verlag, Berlin (1991).

[4] D. Stauffer and A. Aharony, *Introduction to percolation theory*, Second edition, Taylor & Francis, London, Washinghton DC (1992).

[5] J. Feder, *Fractals*, Plenum press (1998).

[6] See for example: D. Abraham *et al.*, *Phys. Rev. B* 26, 5268 (1982); Ch. Leemann *et al.*, *Phys. Rev. Lett.* 56, 1291 (1986); R. Théron *et al.*, *Phys. Rev. Lett.* 71, 1246 (1993).

[7] J. M. Kosterlitz and D. J. Thouless, *J. Phys. C* 6, 1181 (1973).

[8] J. M. Kosterlitz, *J. Phys. C* 7, 1046 (1974).

[9] K. K. Mon and S. Teitel, *Phys. Rev. Lett.* 89, 673 (1989).

[10] S. Teitel and C. Jayaprakash, *Phys. Rev. Lett.* 51, 1999 (1983).

[11] S. Teitel and C. Jayaprakash, *Phys. Rev. B* 27, 598 (1983).

[12] T. Halsey, *J. Phys. C* 18, 2437 (1985).

[13] A. Barone and G. Paterno, *Physics and Applications of the Josephson Effect*, J. Wiley (1982).

[14] M. Tinkham, *Introduction to Superconductivity*, Mc-Graw-Hill, New York (1996).

[15] B. D. Josephson, *Phys. Lett. 1*, 251 (1962).

[16] B. D. Josephson, *Adv. Phys. 14*, 419 (1965).

[17] P. G. De Gennes, *Rev. Mod. Phys.* 36, 225 (1964).

[18] A.-L. Eichenberger, *PhD thesis*, University of Neuchâtel 1997, unpublished.

[19] C. Jornod, *Diploma work*, University of Neuchâtel 1997, unpublished.

[20] S. Rossé, *Diploma work*, University of Neuchâtel 1999, unpublished.

[21] A. Hebard and A. Fiory, *Phys. Rev. Lett.* 44, 291 (1980).

[22] R. Meyer, *PhD thesis*, University of Neuchâtel 1995, unpublished.

[23] J. Perret, *PhD thesis*, University of Neuchâtel 1999, unpublished.

[24] B. Jeanneret *et al.*, *Appl. Phys. Lett. 55*(22), 2336 (1989).

[25] J. D. Jackson, *Classical Electrodynamics*, John Wiley & Sons, New York (1975).

[26] P. Dubos *et al.*, *Phys. Rev. B* 63, 064502-1 (2001).

[27] C. J. Lobb *et al.*, *Phys. Rev. B* 27, 150 (1983).

[28] C. Bailat, *Diploma work*, University of Neuchâtel 1994, unpublished.

[29] J. Hoshen and R. Kopelman, *Phys. Rev. B* 14, 3438 (1976).

[30] D. Abraham *et al.*, *Phys. Rev. B* 26, 5268 (1982);

[31] P. J. Flory, *J. Am. Chem. Soc.* 63, 3083 (1941).

[32] W. H. Stockmayer, *J. Chem. Phys.* 11, 45 (1943).

[33] S. R. Broadbend and J. M. Hammersley, *Proc. Camb. Phil. Soc.* 53, 629 (1957).

[34] B. B. Mandelbrot, *The fractal geometry of nature*, Freeman, San Francisco (1977).

[35] See for example: P. Davies, *The New Physics*, Cambridge University Press, Cambridge (1989).

[36] A. Kapitulnik *et al.*, *J. Phys. A* 16, L269 (1983).

[37] P. G. de Gennes, *La Recherche* 7, 919 (1976).

[38] B. J. Last and D. J. Thouless, *Phys. Rev. Lett.* 27, 1719 (1971).

[39] A. M. Dykhne, *Zh. Eksp. Teor. Fiz* 59, 110 (1970) [Sov. Phys. JETP 32, 63 (1971)].

[40] J. P. Straley *Phys. Rev. B* 15, 5733 (1977).

[41] L. de Arcangelis *et al.*, *Phys. Rev. B* 31, 4725 (1985).

[42] L. de Arcangelis *et al.*, *Phys. Rev. B* 34, 4656 (1986).

[43] A. Coniglio, *Phys. Rev. Lett.* 46, 250 (1981).

[44] Ch. Kittel, *Physique de l'état solide*, Dunod, Paris (1983).

[45] L. de Arcangelis *et al.*, *Phys. Rev. B* 31, 4725 (1985).

[46] L. de Arcangelis *et al.*, *Phys. Rev. B* 34, 4656 (1986).

[47] S. Korshunov, *private communication.*

[48] S. E. Korshunov *et al.*, *Phys. Rev. B* 51, 5914 (1995).

[49] R. Meyer *et al.*, *Phys. Rev. Lett.* 67, 3022 (1991).

[50] R. Meyer *et al.*, *Physica A 191*, 458 (1992).

[51] F. Wegner, *Z. Phys.* 206, 465 (1967).

[52] J.E. Mooij, in *Percolation, Localization and Superconductivity*, A.M. Goldman and S.A. Wolf eds., Plenum, New York (1984), p. 325.

[53] A.-L. Eichenberger *et al.*, *Phys. Rev. Lett.* 77, 3905 (1996).

[54] M. Willemin, *Diploma work*, University of Neuchâtel 1995, unpublished.

[55] J. Affolter, *Diploma work*, University of Neuchâtel 1996, unpublished.

[56] D.C. Harris *et al.*, *Phys. Rev. Lett.* 67, 3606 (1991).

[57] A.-L. Eichenberger *et al.*, *Czech. J. Phys.* 46, 697 (1996).

[58] R. G. Steinmann and B. Pannetier, *Europhys. Lett.* 5 (6), 559 (1988).

[59] J. Affolter *et al.*, *Physica B 280*, 241 (2000).

[60] P. Martinoli *et al.*, *Jpn. J. Appl. Phys.* 26, 1999 (1987).

[61] R. Théron, *PhD thesis*, University of Neuchâtel 1992, unpublished.

[62] A. F. Hebard and A. T. Fiory, *Physica B 109 & 110*, 1637 (1982).

[63] V. Ambegaokar *et al.*, *Phys. Rev. Lett.* 40, 783 (1978).

[64] A. M. Kadin *et al.*, *Phys. Rev. B* 27, 6691 (1983).

[65] V. Ambegaokar and S. Teitel, *Phys. Rev. B* 19, 1667 (1979).

[66] S. Wolf *et al.*, *Phys. Rev. Lett.* 42, 324 (1979).

[67] P. Martinoli, *private communication.*

[68] W.Y. Shih and D. Stroud, *Phys. Rev. B* 30, 6774 (1984).

[69] D. Bormann, *Phys. Rev. Lett.* 78, 4324 (1997).

[70] Ph. Flückiger *et al.*, *Physica B 165 & 166*, 1163 (1990).

[71] V. Ambegaokar and B. I. Halperin, *Phys. Rev. Lett.* 22, 1365 (1969).

[72] D. E. McCumber, *J. Appl. Phys. 39*, 3133 (1968).

[73] C. J. van der Beek *et al.*, *Phys. Rev. B* 48, 3393 (1993).

[74] Ph. Flückiger, *PhD thesis*, University of Neuchâtel 1994, unpublished.

[75] M. E. Fisher *et al.*, *Phys. Rev. A* 8, 1111 (1973).

[76] W. Y. Shih and D. Stroud, *Phys. Rev. B* 32, 158 (1985).

[77] S. E. Korshunov, *J. Stat. Phys.* 43, 17 (1986).

[78] B. J. van Wees *et al.*, *Phys. Rev. B* 35, 7291 (1987).

[79] Jorge V. José *et al.*, *Physica B 194-196*, 1671 (1994).

[80] P. Martinoli *et al.*, *Physica Scripta* T49, 176 (1993).

[81] Ph. Lerch *et al.*, *Phys. Rev. B* 41, 11579 (1990).

[82] B. Berge *et al.*, *Phys. Rev. B* 34, 3177 (1986).

[83] H. Eikmans *et al.*, *Phys. Rev. B* 39, 11759 (1989).

[84] D. Ariosa *et al.*, *J. Phys. France* 51, 1373 (1990).

[85] J. E. van Himbergen, *Physica B 152*, 46 (1988).

[86] E. Granato and J. M. Kosterlitz, *J. Appl. Phys.* 64, 5636 (1988).

[87] M. F. Sykes and M. E. Fisher, *Physica* 28, 919 (1962).